Høgskulen på Vestlandet

BACHELOR'S THESIS

An investigation of near-surface vapor pressure gradients in the snowpack

En undersøkelse av overflatenære damptrykksgradienter i snødekket

Emma Hauglin, Thor Parmentier, and Ola Thorstensen

Geology and geohazards

Department of environmental sciences

Supervisor: Simon De Villiers

03.06.22

We confirm that the work is self-prepared and that references/source references to all sources used in the work are provided, *jf. Forskrift om studium og eksamen ved Høgskulen på Vestlandet, § 12-1.*

Preface

This thesis marks the completion of a bachelor's degree in Geology and Geohazards at HVL.

We would like to thank Simon for providing good support and believing in the project. The ideas and feedback along the way really inspired and pushed the project forward. We would like to thank Statnett for letting us conduct the field work on their property at Slakkafjellet with access to electrical power. This was a key factor in order to gather weather data for a longer period of time, which was crucial for this project. Thanks to our teachers at HVL which have been good mentors during our time here. Lastly, thanks to our fellow geology students at HVL, which have contributed to a very pleasant and fun three years in Sogndal.

Abstract

The formation of near-surface faceted crystals caused by diurnal recrystallization has been observed by Birkeland et al. (1998). Lab experiment results by Pinzer and Schneebeli (2009) showed that oscillating temperature gradients did not lead to faceting. This thesis investigates if real-world asymmetry in the near-surface vapor pressure gradients is a prerequisite for the process of diurnal recrystallization. Two mechanisms for asymmetry are hypothesized, (1) the effect of warm snow having a higher equilibrium vapor pressure than cold snow, and (2) differences between heating and cooling of the snowpack.

To explore vapor pressure gradients, a numerical model was developed by solving the 1D heat equation in Excel using the finite difference method. The model predicts temperature evolution in a snowpack which allows for the calculation of vapor pressure gradients at high resolutions. Field work was conducted where metrological data and snow temperatures were collected to calibrate and evaluate model performance. Lastly, a function to quantify facet growth rate by vapor pressure gradient was developed to analyze the mechanisms of asymmetry. Sub-faceting gradients are not considered.

Though the model has weaknesses such as the use of sensible heat as a fitting parameter and the use of a constant solar radiation extinction coefficient, it produces plausible temperatures and vapor pressure gradients. The results indicate that asymmetry in the heating and cooling of the snowpack (hypothesis 2) is more important for diurnal recrystallization than the effect of temperature (hypothesis 1) alone. When working in tandem, the effect of temperature can amplify the asymmetry in heating and cooling. Mean negative temperature gradients in the snowpack lead to negative facet growth being the dominating process deeper than 2 cm. Negative vapor pressure gradients are maintained in the top 0 – 1 cm, in a combination of diurnal recrystallization and radiation recrystallization.

Contents

1. Introduction

The growing popularity of recreational activities in the mountains exposes more people to avalanche danger than before. Since 2008, 96 people have been killed by snow avalanches in Norway, where 67% of the fatal avalanches were caused by a persistent weak layer in the snowpack (Varsom, 2022). To produce accurate avalanche forecasts, research on this topic is important to understand the physical processes which alters the snowpack to form avalanches.

Slab avalanches can occur in stratified snowpacks, when a cohesive layer of snow is deposited on top of a thinner and weaker layer (McClung & Schaerer, 2006). Overburden stress can cause failure in the weak layer which initiates a slab avalanche. Faceted crystals are a type of snow that are weak in shear and have poor bonding properties, which can lead to persistent weak layers when buried (McClung & Schaerer, 2006). One of the proposed mechanisms for the formation of near-surface faceted crystals is called diurnal recrystallization. Birkeland et al. (1998) reports that during clear weather with warm sunny days and cold nights, big diurnal temperature fluctuations at the snow surface creates big temperature and vapor pressure gradients within the top five centimeter of the snowpack. These bi-directional near surface gradients are believed to facilitate facet growth. However, Pinzer and Schneebeli (2009) observed no facets during a lab experiment where they subjected snow samples to alternating, symmetrical temperature gradients for two weeks.

The aim of this thesis is to explore temperatures, temperature gradients and vapor pressure gradients in the snowpack, by developing a numerical model which can predict temperature evolution of the snow based on collected radiation and weather data from the field. In addition, a method to quantify facet growth based on the present vapor pressure gradient has been developed. By using these tools, this thesis will try to answer why Pinzer and Schneebeli (2009) did not observe facets during their lab experiment. The main hypothesis is that diurnal temperature fluctuation in nature leads to asymmetrical vapor pressure gradients. The asymmetry can be caused by two mechanisms: (1) Higher temperatures lead to higher vapor pressure gradients. (2) Heating and cooling of the snowpack does not happen symmetrically.

2. Theory/background

2.1. Properties of snow

2.1.1. Specific heat capacity

Specific heat is a property which quantifies the amount of energy that must be put into a unit amount of snow to change its temperature. For dry snow, the contributions from air and water are typically disregarded. This results in the product of snow density and the specific heat capacity for ice at -5°C (2090 J/kg °K) (Langham, 1982).

2.1.2. Density

Snow density is given by the ratio of mass to volume expressed as kg/m^3 and has a broad range from 30-500 kg/m^3. Typical values for fresh dry snow are 30-150 kg/m^3 that increases to the highest densities in seasonal snow of 400-500 kg/m^3. Snow deposited by wind can attain densities up to 300-400 kg/m^3, while typical values for ice crusts are 700-800 kg/m^3. The bulk amount of seasonal snow consist of 50 % air, or more by volume compared to the density for pure ice at 917 kg/m^3. This is an important property with respect to the metamorphism processes that depend on water vapor content in the pore space, which is further discussed in section 2.1.3 and 2.3 (Armstrong & Brun, 2008).

2.1.3. Thermal conductivity

The speed of heat transferred trough a material is controlled by the property thermal conductivity. This can be expressed by the Fourier equation as (Armstrong & Brun, 2008):

$$q = k_{eff} \frac{\partial T}{\partial x} \qquad (1)$$

Where q is the heat flux, k_{eff} is the effective thermal conductivity and $\partial T / \partial x$ is the temperature gradient in the direction of heat flow. Since snow is not limited to a solid phase, but also water and gas, Sturm et al. (1997) identifies three mechanisms contributing to heat transfer with the snowpack: Conduction through the crystal lattice, conduction through the air in the pore space and latent heat transfer by vapor diffusion. When measuring the conductivity of snow, these mechanisms all contribute to the heat flux resulting in an "effective" thermal conductivity. For ice, the thermal conductivity increases with decreasing temperature (Langham, 1982; Pinzer et al., 2012). In contrast, the thermal conductivity of snow have an inverse

dependence on temperature because of vapor transport in the pore space (Sturm et al., 1997). Several studies have shown that the thermal conductivity of snow has a correlation with snow density, as presented in Figure 1. They explain the scatter in values through difference in temperature and microstructure of the snow samples. Sturm et al.(1997) remarks that for depth hoar and faceted crystals there is no clear relationship between density and thermal conductivity. While rounded grains and windblown fragments show a clear relationship of increasing thermal conductivity with increasing density.

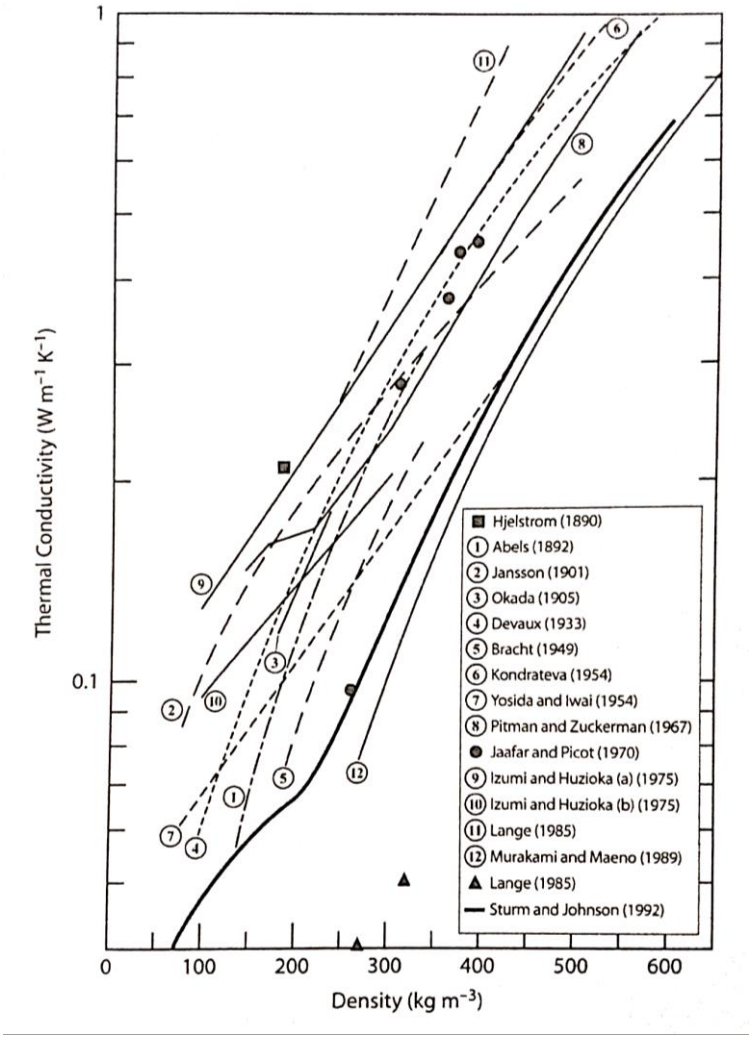

Figure 1 Effective thermal conductivity with increasing density from Sturm & Johnson (1992).

2.2. Energy balance

To create a mathematical model that accurately predicts the temperature evolution of a snowpack, it is important to understand the processes that influence the energy flux into and out of the snowpack. In glacier studies, near surface temperature and ablation rates are calculated by measuring the energy exchange in Watts across a given surface area (Benn & Evans, 2010). The energy fluxes are divided into components and expressed as terms in an energy balance equation. When neglecting horizontal energy transfers and assuming an open and flat surface, the following equation for energy balance in a snow cover is expressed by Armstrong & Brun (2008):

$$\frac{\partial Q}{\partial t} = SW_{net} + LW_{net} + H_s + H_L + H_P + G \quad (2)$$

Where: $\frac{\partial Q}{\partial t}$ = net change of the snowpack's internal energy per unit area

SW_{net}= net shortwave radiation

LW_{net} = net longwave radiation

H_S = sensible heat flux

H_L = latent heat flux

H_P = energy flux carried as latent or sensible heat by precipitation and blowing snow

G = ground heat flux

2.2.1. Shortwave radiation

Solar insolation is electromagnetic radiation in the spectrum 0,2 to 4 μm which respectively spans from ultraviolet to near-infrared It is usually referred to as shortwave radiation and accounts for 99,2% of the total incoming insolation (Armstrong & Brun, 2008). Most of the incoming shortwave radiation is reflected into the atmosphere due to the high albedo of snow. The albedo (α) can be calculated as the ratio of outgoing and incoming shortwave radiation (Benn & Evans, 2010):

$$\frac{SW_{out}}{SW_{in}} = \alpha$$

(3)

Calculating the net shortwave term of the energy balance equation can be done accordingly (Benn & Evans, 2010):

$$SW_{net} = SW_{in}(1 - \alpha)$$

(4)

Snow albedo can vary between 0.8 and 0.95 for a dry snow surface, while the albedo of a wet snow surface is significantly lower, at 0.5-0.7 (Armstrong & Brun, 2008). The albedo of a homogenous snow cover is dependent on grain size and the contents of impurities. Since these values usually increase with an aging snowpack, albedo often decreases with time. The formation of faceted crystals or surface hoar can have an opposite effect (Armstrong & Brun, 2008). The albedo of snow changes diurnally because of its dependency on solar zenith angle. Warren & Wiscombe (1980) found albedo to increase with decreasing solar zenith at all wavelength, they also remark that ice absorbs little visible light, but it has strong absorption in the near-infrared spectrum, leading to a spectral difference in albedo independent of zenith angle.

The remaining solar radiation penetrates the snow surface and heats the upper snowpack. According to Armstrong & Brun (2008) the extinction rate depends on grain size and crystal morphology. For the near-infrared spectrum penetration decreases with increasing grain size of granular shape, but not for increasing grain size of faceted crystals. McClung & Schaerer (2006) estimate that for alpine snow with a density of 100kg/m^3, less than 10% of the penetrating radiation remains after 10 cm. Measurements of peak temperatures at 10 cm depth in the Antarctic snowpack have led to the "solid state greenhouse" idea, which is explained by the effect of solar heat distributed at depth and radiative surface cooling (Brandt & Warren, 1993). However, Brandt and Warren (1993) show that the penetrating solar radiation which contributes to heating is mostly near-infrared radiation, which is absorbed in the top few millimeters. In their article, they show that for snow with a grain radius of 0,1mm, 44% of the total energy is absorbed in the top millimeter. They remark that blue light penetrates deep into the snowpack and almost all of it is scattered back and re-emerges at the surface, adding no heat to the snowpack.

Modeling the depletion of solar radiation with depth in a snowpack can be done by using Beer-Lambert-Bouger's law of extinction (Fierz et al., 2008):

$$I(x) = SW_{net} e^{-Kx}$$

(5)

Where: SW_{net} = net shortwave flux [W/m^2]

x = depth (positive downwards) [m]

K = the extinction coefficient for snow [m^{-1}]

By treating the incoming net shortwave radiation energy as a volume source, it can be distributed with depth in accordance with the obtained curve. Finding a fitting value for the extinction coefficient could be done by using a function based on snow density, grain diameter and wavelength or simply by using a fixed value. In the paper by Fierz et al. (2008), they compared real snowpack temperatures with modeled temperatures where different extinction models where used. In all models 90% of the SW energy was absorbed in the first centimeter of the snowpack. They concluded that the model with a fixed extinction coefficient of -230 m^{-1}, produced temperatures at depth (15-30 cm) which were one degree colder than the physical measurements. Fierz et al. (2008) concluded that a multiband extinction model which considers shortwave absorption over a larger range of depth provided the most promising result.

2.2.2. Longwave radiation

Longwave radiation is electromagnetic radiation in the infrared spectrum with wavelengths from 4 to 100 μm (Armstrong & Brun, 2008). All objects with a temperature above absolute zero emit thermal energy as radiation. The emitted longwave energy flux from a snowpack can be calculated from the snow surface temperature using the Stefan-Boltzmann law:

$$LW_{out} = \varepsilon \sigma T^4$$

(6)

Where LW_{out} is the emitted radiation flux [W/m^2], ε is the emissivity, σ is the Stefan-Boltzmann constant [W/m^2K^4] and T is the absolute temperature of the surface in Kelvin. Snow is often assumed to behave as a black body, a perfect absorber with respect to longwave radiation with emissivity that ranges between 0.995 to 0.98 (Benn & Evans, 2010). The high emissivity of snow causes the thermal radiation from one crystal to be absorbed by the neighboring ones, therefore thermal radiation loss to space is limited to the snow surface (Brandt & Warren, 1993). The main source of incoming longwave radiation is from clouds, atmospheric gases and terrestrial objects surrounding the snow. According to Armstrong and

Brun (2008), most of the incoming longwave radiation is absorbed in the first few millimeters of the snow surface. The outgoing radiation is normally bigger than the incoming, providing a net energy loss from the snowpack. The net longwave radiation heat flux from the snow surface is expressed by Benn & Evans (2010) with the incoming and outgoing longwave radiation:

$$LW_{net} = LW_{in} - LW_{out} \quad (7)$$

2.2.3. Sensible heat

Sensible heat flux is the turbulent heat exchange at the snow-air surface boundary (Armstrong & Brun, 2008). The phrase sensible heat originates from the idea that the changes in temperature can be sensed. Heat is either added or lost from the snowpack to the air by conduction of thermal energy between the materials. Since air is a good insulator, efficient heat exchange is dependent on the bulk movement of air near the surface. This occurs either by convection or turbulence created by wind eddies which replace the near-surface air with new air, maintaining the sensible heat flux. (Benn & Evans, 2010). One way to calculate the exchange of sensible heat is by using the bulk transfer method used by Hachikubo (2001):

$$Q_h = C_h c_p \rho_a w_z (T_z - T_s) \quad (8)$$

Where: Q_h = Sensible heat flux

C_h = Bulk transfer coefficient of heat

c_p = The specific heat of air

ρ_a = The air density

w_z = Wind speed

T_z = The air temperature

T_s = The surface temperature

The subscript z means height above the snow surface. The coefficient C_h is calculated by:

$$C_h = C_N(1 - 5R_B)^2 \quad \text{when} \quad 0 \leq R_B \leq 0{,}2$$

(9)

$$R_B = \frac{g(T_z - T_s)z}{T_m {w_z}^2}$$

(10)

C_N is the bulk transfer coefficient in a neutral atmosphere. Hachikubo (2001) used a value of $3{,}3 \times 10^{-3}$. R_B is the bulk Richards number and T_m is the mean air temperature, which is the same value as T_z (K).

2.2.4. Latent heat

Latent heat is the energy absorbed or released during a phase change. Since warm air can contain more moisture than cold air, a diffusion of water vapor molecules takes place from warm areas to cold areas. When water vapor diffuses from the air and deposits on to the snow surface, the amount of heat added to the snowpack, the latent heat of sublimation, is 2.838 x 10^6 J/kg for ice at 0° (Armstrong & Brun, 2008). Wind and air temperature are the main controls of latent heat flux. As with sensible heat, turbulence in the air replaces the near-surface air, maintaining the vapor diffusion and latent heat flux. The heat flux from phase changes is small, but relevant for surface hoar formation (McClung & Schaerer, 2006). Hachikubo (2001) presents a simple model for latent heat calculation:

$$sH_L = C_e \rho w_z (q_z - q_s)$$

(11)

Where sH_L is the latent heat flux for sublimation, C_e is the bulk transfer coefficient for water vapor, w_z is windspeed measured z meters above the snow surface, and q is the specific humidity. To measure accurate micrometeorological data of high frequency, Stössel et al. (2010) suggest the use of paired anemometers and CO_2/H_2O analyzers mounted at three and five meters above the snow surface.

2.2.5. Heat from precipitation

Energy is added or removed from the snowpack with mass changes. This happens when wind-transported snow or precipitation transports energy in the form of latent or sensible heat (Armstrong & Brun, 2008, p. 72). Heat is added when warm rain penetrates the snowpack and is removed when cold wind-drifted snow deposits on a warmer snowpack. The effect of this heat flux is small compared to the other heat fluxes,

but can be significant when the water from a rainfall freezes and releases latent heat of fusion (Gray & Male, 1982).

2.2.6. Ground heat

Ground heat flux is the energy transfer between the snow-soil interface. Because of snow's insulating properties, at depths below 0.3 m the snowpack temperatures are minimally influenced by diurnal temperature fluctuations, creating a gradual increase in the snow temperature towards the bottom (Birkeland, 1998) (Figure 2). Throughout the winter, the ground temperature is 0°C, providing an upwards heat flux into the snowpack. Heating of the ground is mainly due to summer warming but geothermal heating also keeps the ground from freezing (McClung & Schaerer, 2006). The small energy flux at the snow-soil interface does not contribute to the diurnal temperature fluctuations near the surface.

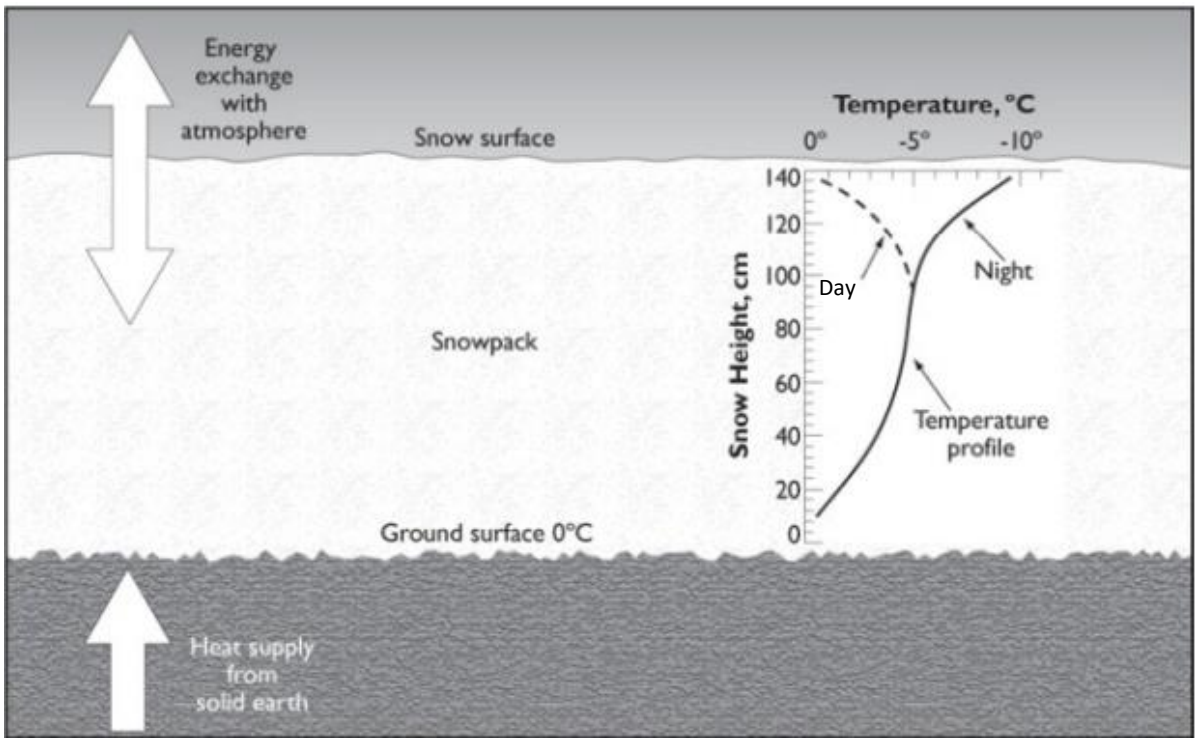

Figure 2 Temperature profiles for day and night in a snowpack. The temperature profiles presented in this thesis are mirrored, with negative temperatures to the left of the y-axis. From McClung and Schaerer (2006, p. 53).

2.3. Snow metamorphism

Snow is a complex medium which exists in an equilibrium state of solid, liquid and gas, all at the same time. Snow crystals are formed in a supersaturated environment in the atmosphere where the values of supersaturation can be more than 50% (McClung & Schaerer, 2006). The level of supersaturation in a snowpack are typically less than 1%, meaning that the newly deposited snow crystals are exposed to a different environment than where it was created, initiating metamorphism. Heat flow and pressure within the snowpack are the two mechanisms driving metamorphism, where heat flow is the predominant in a seasonal snow cover (McClung & Schaerer, 2006, p. 55). Snow metamorphism can be separated into what in older literature is termed "destructive" or "constructive" metamorphism, or as LaChapelle & Armstrong (1977) term it, "equi-temperature" and "temperature gradient" metamorphism. McClung & Shaerer (2006) argue that temperature gradients are present during both types of metamorphism and "equi-temperature" conditions only occur when the entire snowpack is 0°C. In this thesis, the terms "rounding" and "faceting" are used for these processes, producing respectively rounded or faceted crystals. Rounding is when snow crystals sinter, increase bond strength and equilibrate toward a shape with low surface energy. The process of rounding usually takes significantly longer time than faceting (McClung & Schaerer, 2006). Faceted crystals or their ultimate form, depth hoar, are angular crystals that form weak layers in the snowpack. They bond poorly because of fewer contact points between grains and are anisotropic, being strong in compression and weak in shear. This makes these weak layers dangerous because they can support an overlying slab but fail catastrophically with the right trigger (Fredston & Fesler, 2011; McClung & Schaerer, 2006; Nes, 2018).

2.3.1. Diffusion in snow

During metamorphism, snow crystals redistribute, lose, or gain mass mainly due to vapor diffusion in the pore space of the snowpack. Whether vapor sublimates or deposits off or on to a crystal is controlled by the level of supersaturation of the air around the given crystal. One of the diffusion processes is the effect of curvature, known as the Kelvin effect (Dunlop, 2008). If a surface is curved in a convex manner, such as the surface of a water droplet, the saturation levels will be stronger around the given droplet than above a flat plane of water with the same temperature (McClung & Schaerer, 2006). The effect is opposite around a concave surface. Since saturation levels are dependent on geometry, a dendritic snow crystal in a non-supersaturated environment will begin to decompose and become rounded, as mass diffuses from the sharply convex arms of the crystal to the concave base where saturation levels are lower. The Kelvin effect is small, however, compared to the effect of vapor pressure gradients in the intercrystalline spaces (McClung & Schaerer, 2006; Pinzer et al., 2012).

Metamorphism through hand-to-hand transfer of vapor by diffusion is the dominating mechanism in a seasonal snowpack (McClung & Schaerer, 2006). Equilibrium vapor pressure of water over ice is dependent on temperature, which means a temperature gradient in the snowpack induces a vapor pressure gradient. Since this relationship increases nonlinearly, a temperature gradient near 0°C means a higher vapor pressure gradient than the same temperature gradient at a lower mean temperature (LaChapelle & Armstrong, 1977). Vapor diffuses through the pore space from warm areas in the snowpack towards colder areas where the vapor pressure is lower (Langham, 1982). Temperature and vapor pressure gradients in a snowpack are primarily vertical (and negative), with heat and vapor flowing upward from the relatively warm ground-snow interface toward the cooler snow surface. When there is a high vapor pressure gradient in the pore space between two crystals, water vapor will diffuse (typically upward) from one crystal to the next. The individual snow crystals maintain a locally constant temperature, due to their relatively high conductivity compared to the air between them. Sublimation will occur on the undersaturated top side of the lower crystal, while deposition will occur on the bottom side of the locally supersaturated upper crystal (McClung & Schaerer, 2006). If the vapor pressure gradient is high enough, faceted crystals will start to form.

2.3.2. Rate of faceting

A critical threshold value for vapor pressure gradient must be exceeded for the process of faceting to dominate over rounding (LaChapelle & Armstrong, 1977). Since temperature is quite easy to measure and vapor pressure is distinctly not so, temperature gradient has often been used to determine the mode of metamorphism active in a snowpack. McClung & Schaerer (2006) suggest that the threshold temperature gradient for faceting is 10 K/m. Miller et al. (2003) present a range, 10-20 K/m for the threshold between rounding and faceting and 25 K/m for "highly efficient growth". Pinzer and Schneebeli (2009) used 20 K/m in their experiment. As explained in chap. 2.3.1., vapor pressure is a nonlinear function of temperature, so using a critical temperature gradient is useless without its accompanying mean temperature. LaChapelle and Armstrong (1977) found that a critical vapor pressure gradient of 5 mb/m with a corresponding temperature gradient that varies with temperature is required for faceting (Figure 3). A 10 K/m temperature gradient is equal to a 5 mb/m vapor pressure gradient at 0°C (based both on Figure 3 and calculations done in chap. 3.1.4.). In general, higher temperatures result in bigger growth rates, because a smaller temperature gradient is needed to produce the critical vapor pressure gradient. According to Miller et al. (2003), the threshold value for faceting is, in addition to temperature gradient and absolute temperature, dependent on snow density, pore-space size and grain size. Lower density snow transitions at a lower temperature gradient and larger grains transition at a lower temperature gradient

(Miller et al., 2003). Exploring all factors is outside the scope of this thesis, therefore the focus will be on the effect of vapor pressure gradients in the snowpack.

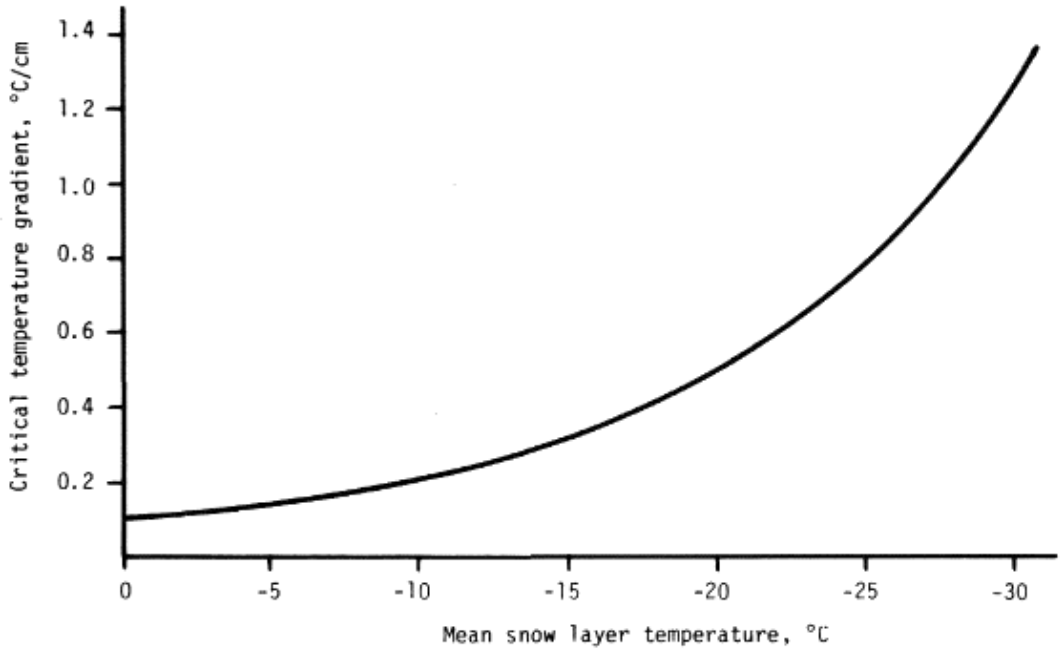

Figure 3 The critical temperature gradient needed to provide the critical vapor pressure gradient, 5 mb/m, with mean snow temperature (LaChapelle & Armstrong, 1977, p. 27).

Defining how quickly facets grow after surpassing the 5 mb/m threshold is a complex matter. Faceting happens faster in low density snow with large pores and temperatures close to 0°C (Jamieson, 2006; McClung & Schaerer, 2006, p. 56). Miller and Adams (2009) simulated the effect crystal orientation with respect to the direction of the temperature gradient had on growth rates. Marbouty (1980) found an upper limit of density, where snow denser than 350 kg/m^3 did not grow even under vapor pressure gradients well above the threshold. As with the threshold value required for faceting, the model is a simplification, and will be focusing on the effect of vapor pressure gradients, not crystal orientation or density. Miller and Adams (2009) say that there is no standardized method for describing the geometry of faceted crystals. Grain radius is often used for rounded grains, but facets can be irregular in shape and size and a radius can be difficult to define. This makes comparing facet size between studies a challenge. Two studies that use similar definitions of grain size are Marbouty (1980) and Fukuzawa and Akitaya (1993). Both studies exposed samples of snow to high vapor pressure gradients in one direction over time. Marbouty (1980) defined grain size by taking photos of a sample, then dividing the total area by the number of crystals. He explored the effects of temperature gradient, temperature, snow density and initial

snow type on the process of faceting. Fukuzawa and Akitaya (1993) defined snow crystal size as the diameter of a circle with the same area as the projected area of the snow crystal. They explored the effects of temperature gradients on growth rate in a lab compared to measured rates in the field.

2.4. Near-surface faceted crystals

Layers of faceted crystals near the surface of the snowpack are, according to McClung & Schaerer (2006), quite important when working with snow avalanches. They are more easily triggered by humans than weak layers deeper in the snowpack. Birkeland (1998) presents three processes that form near-surface faceted crystals, radiation recrystallization, melt-layer recrystallization and diurnal recrystallization. Radiation recrystallization is a process where solar radiation warms the subsurface snow, often to or near the melting point, while longwave radiative cooling keeps the surface dry and cold. This can give intense temperature and vapor pressure gradients in the top 1-2 cm of the snowpack (McCabe et al., 2008). Melt-layer recrystallization occurs when a wet layer of snowpack (melted by sun or rain) gets buried by cold, dry snow. The wet snow stays at 0°C until it has frozen, while the dry snow above can have much colder surface temperatures, giving strong temperature and vapor pressure gradients in the dry snow (Birkeland, 1998). Diurnal recrystallization is described in detail in the next section. All three of these processes can occur together and work in tandem, so it can be quite difficult to separate them (Birkeland, 1998; McCabe et al., 2008).

2.4.1. Diurnal recrystallization

Diurnal recrystallization is the mechanism behind the formation of faceted crystals near the surface that is the focus of this thesis. Since the density of snow is quite low and most of its volume is air, snow makes for a great insulator. The snow temperature below approximately 30 cm under the surface is therefore relatively stable and does not change quickly. Changes in temperature throughout the day and night, or diurnal temperature oscillations, cause the temperature of the snow surface to vary widely and cause large temperature gradients and vapor pressure gradients to form (Figure 2). The highest temperature gradients typically occur in high pressure, fine weather situations, where the nights are clear and cold, and the days are sunny and relatively warm. This can give temperature gradients of over 200K/m in areas of the upper 30 cm of the snowpack. (Birkeland, 1998; Birkeland et al., 1998). According to Birkeland (1998), the diurnally oscillating temperature gradients, negative during the night and positive during the day, can cause widespread faceting in all elevations and aspects. Cooperstein et al. (2004) found a few years later that near surface facets from diurnal recrystallization, tended to be more developed on south-facing aspects, but still present on north-facing aspects.

Diurnal recrystallization usually only happens in the top 15 cm, with the weakest crystals at or just below the surface (Birkeland, 1998). Faceting due to diurnal recrystallization can occur over the course of a single day, but several days of oscillating temperature gradients will lead to more highly developed facets. Stratton (1997, as cited in (Birkeland, 1998) claims that daytime snow surface temperatures just below melting, clear night skies, and low density snow support the growth of diurnally recrystallized facets. Observations of diurnally recrystallized facets and near-surface facets have been done by others as well. Hardy et al. (2001) studied large faceted crystals formed by bi-directional gradients of temperature and vapor pressure in the mountains of Bolivia. Hood et al. (2005) endeavored to document the conditions necessary to form near-surface faceted crystals in Alaska. McCabe et al. (2008) observed six separate radiation recrystallization events in Montana.

2.4.2. Birkeland et al. (1998)

In the 1995-96 winter in Montana, Birkeland et al. (1998) measured snowpack temperature gradients and calculated vapor pressure gradients during a clear sky period that formed diurnally recrystallized facets. The facets developed into 1 mm big crystals in a 5-10 cm thick layer of newly fallen snow within 36 hours. The observed negative temperature gradients exceeded 200 K/m in the night, more than twenty times the rule of thumb threshold value of 10 K/m required for faceting (Figure 4). The observed vapor pressure gradient exceeded 25 mb/m in both directions (Figure 5), five times greater than the 5 mb/m that is required for faceting. The largest temperature gradients and vapor pressure gradients were found in the top 5 cm of the snowpack, with decreasing values the deeper they measured.

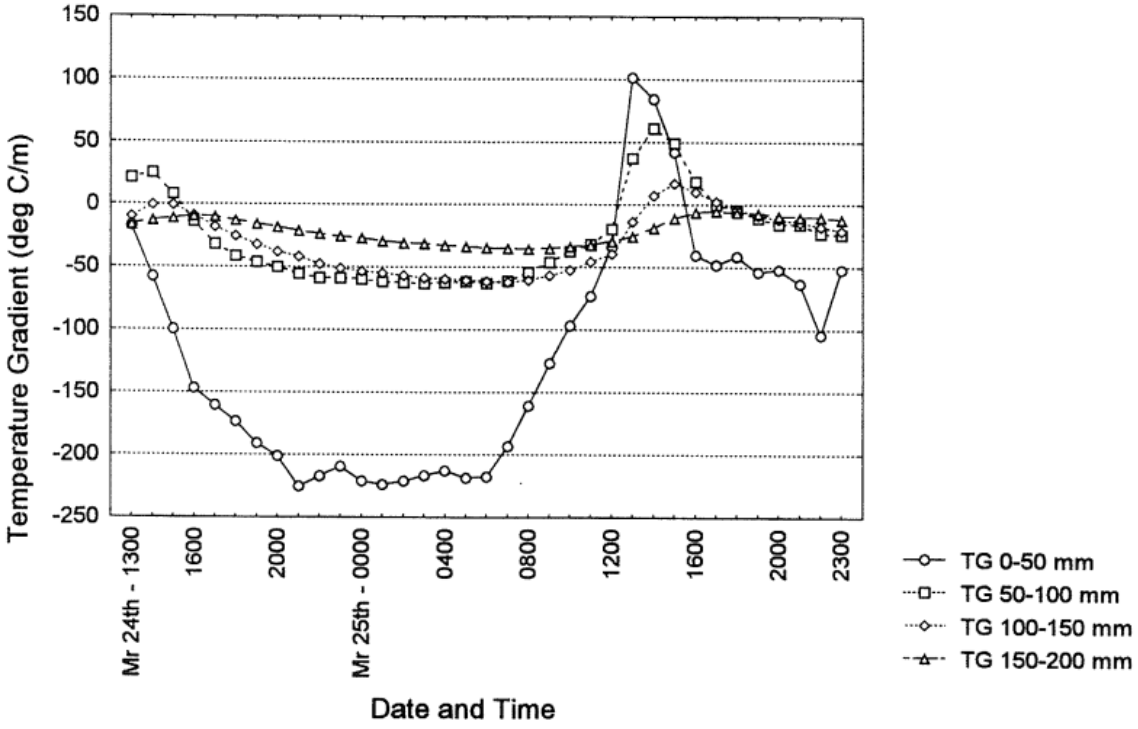

Figure 4 Temperature gradients from Birkeland et al. (1998) during a clear sky period in March 1996.

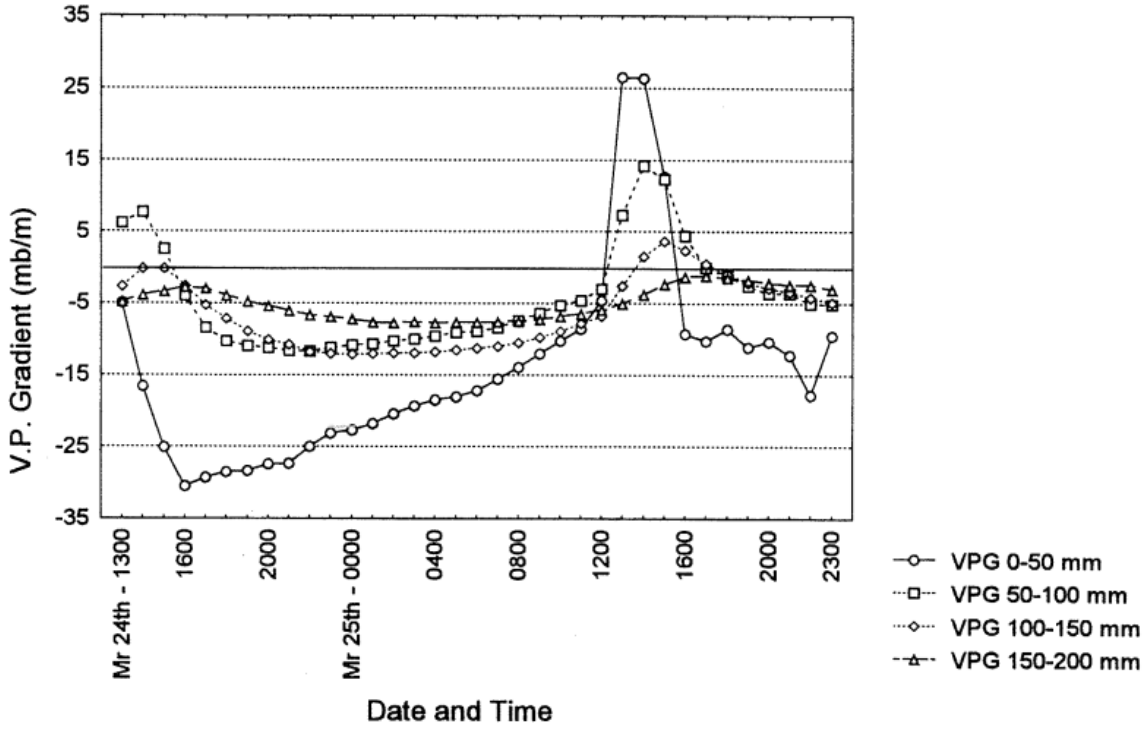

Figure 5 Vapor pressure gradients from Birkeland et al. (1998) during a clear sky period in March 1996.

2.4.3. Pinzer & Schneebeli (2009)

In controlled laboratory experiments Pinzer and Schneebeli (2009) changed the temperatures at the top and bottom of a 53 mm in diameter and 20 mm high cylinder of snow with symmetrical, but opposite, sinusoidal temperature gradients between 80 and 120 K/m for 14 days. The sample was exposed to temperature gradients above their nominal threshold of 20 K/m for 86% of the time. Despite having large, but realistic temperature and vapor pressure gradients, Pinzer and Schneebeli (2009) observed no faceting in their samples taken with a μCT scanner in the innermost 36.9 mm of the total diameter, a height of 7.488 mm in the center of the snow sylinder. They argue that this challenges the theory of a critical temperature gradient, and their results indicate that one cannot tell the history of a snow crystal only by its morphology. Rounded grains can be the result of high temperature and vapor pressure gradients. They also state that the fixed mean temperature and symmetrical nature of their experiments are too simple compared to what happens in nature.

2.4.4. Mechanisms for asymmetry

This raises the question as to why Pinzer and Schneebeli (2009) did not observe any faceting in their lab experiment even though the snow sample was exposed to high sinusoidal temperature gradients. This thesis investigates whether their experiment was so symmetrical that all facet growth in one direction might have been undone by the facet growth in the opposite direction. While in nature, facets grow because of asymmetry. Two hypothesized mechanisms explaining the real-world asymmetry are presented here.

The first hypothesis is that since there is a higher equilibrium vapor pressure in a warm snowpack than in a cold one, a fixed temperature gradient will lead to a higher vapor pressure gradient in the snowpack during daytime when the snow is warm, than at night.

The second hypothesis is that heating and cooling of the snowpack does not happen symmetrically. When the snowpack cools in the evening and through the night, outgoing longwave radiation from the surface dominates. Longwave radiation rapidly cools the surface of the snow, but since the effective conductivity of snow is low, the rest of the snowpack cools more slowly and lags behind the top few millimeters. When heating the snowpack, shortwave radiation from the sun penetrates the snow surface and heats the near surface snow (described in section 2.2.1). Energy is distributed in the top few centimeters of snow and creates smaller positive temperature gradients compared to the larger negative temperature gradients formed under cooling, when the change is initiated right at the surface.

A drift in the mean temperature of the snow and different durations heating and cooling could also cause asymmetry in the snowpack but it is not investigated in this thesis.

3. Methods

3.1. Numerical model

Using a numerical model to investigate snowpack temperatures and energy balance has been done by HVL bachelor group Lundberg et al. (2019). The model developed for this thesis was inspired by their work. During this project the model has increased in complexity, where the finished product is essentially two models, one with Dirichlet and the other with Neumann boundary conditions. For both models, energy flux where heat is flowing into the snowpack is defined as positive, inversely outgoing flux is defined as negative.

3.1.1. Solving the one-dimensional heat equation

Heat transfer within the snowpack is dominant in the vertical direction, between the ground and the snow surface. When neglecting horizontal heat transfer, Anderson (1976) argue for the use of the one-dimensional heat equation to calculate temperature evolution in a uniform snowpack:

$$\frac{\partial u}{\partial t} = \alpha \frac{\partial u^2}{\partial x^2}$$

(12)

Where: u = temperature [K]

t = time [s]

x = vertical distance [m]

α = the thermal diffusivity [m^2/s]

The thermal diffusivity is given by:

$$\alpha = \frac{k_e}{c_i \rho_s}$$

(13)

Where: c_i = the specific heat capacity of ice [J /kg K]

ρ_s = the snow density [kg/m^3]

k_e = the effective thermal conductivity of snow [W/m K]

The finite difference method is used to solve the heat equation numerically. This method works by splitting the derivative terms into a finite number of segments (x), then the temperature evolution for each segment is calculated for a set difference forward in time (Δt). The size of segments (Δx) and duration of time difference influences the margin of error of the calculation. For the left side of equation (12), the change in temperature at a given segment after a difference in time can be approximated by:

$$\frac{\partial u}{\partial t} \approx \frac{u(x, t + \Delta t) + u(x, t)}{\Delta t}$$

(14)

The second derive term of equation (12), a solution is found by using Taylor series expansion as an approximation:

$$f(x + \Delta x) = f(x) + \Delta x f'(x) + \Delta x^2 \frac{f''(x)}{2!} + \Delta x^3 \frac{f'''(x)}{3!} + \Delta x^4 \frac{f^{(4)}(\xi_1)}{4!} \ldots$$

(15)

$$f(x - \Delta x) = f(x) - \Delta x f'(x) + \Delta x^2 \frac{f''(x)}{2!} - \Delta x^3 \frac{f'''(x)}{3!} + \Delta x^4 \frac{f^{(4)}(\xi_2)}{4!} \ldots$$

(16)

Where f(x) = the given function

ξ = is a number between $x \; and \; (x + \Delta x) or \;\; x \; and \; (x - \Delta x)$

Adding the expansions shown in equation (15) and (16) gives:

$$f(x + \Delta x) + f(x - \Delta x) = 2f(x) + \Delta x^2 f''(x) + \Delta x^4 \frac{(f^{(4)}(\xi_1)) + (f^{(4)}(\xi_2))}{24}$$

(17)

Rearranging equation (17) gives:

$$\frac{f(x + \Delta x) - 2f(x) \; + f(x - \Delta x)}{\Delta x^2} - f''(x) = \Delta x^2 \frac{(f^{(4)}(\xi_1)) + (f^{(4)}(\xi_2))}{24}$$

(18)

The second derivative term is then given by:

$$\frac{\partial u^2}{\partial x^2} \approx \frac{u(x+\Delta x,t) - 2u(x,t) + u(x-\Delta x,t)}{\Delta x^2}$$

(19)

Substituting the terms obtained in equation (14) and (19) into equation (12) and rearrange the terms to obtain the solution for the temperature at segment x after a determined time step ($t + \Delta t$):

$$u(x,t+\Delta t) = u(x,t) + \alpha \frac{\Delta t}{\Delta x^2}\left(u(x+\Delta x,t) - 2u(x,t) + u(x-\Delta x,t)\right)$$

(20)

The heat equation was solved in Excel by constructing a matrix where equation (20) fills the domain. Cells $u(x_0,t)$ and $u(x_{max},t)$ respectively represents the top and bottom conditions at the domain boundary, where a solution is calculated based on the imposed values. Cells $u(x,t_0)$ represents the initial condition from which the temperature differences forward in time are calculated. Since the temperature at sufficient depth is close to constant, as discussed in chapter 2.2.6., the temperature evolution of the model is mainly driven by temperature fluctuations at the surface boundary.

When using the finite difference method to approximate a solution, round off errors with a sufficient magnitude will collapse the computation because of amplification of the solution values. This can be avoided using by using a small forward difference in time (Δt) for a given distance between points (Δx). Von Neumann stability analysis predicts that a stable model must satisfy the following equation:

$$\alpha \frac{\Delta t}{\Delta x^2} \leq \frac{1}{2}$$

(21)

3.1.2. Implementing Neumann boundary condition

To further improve the model's interaction between the snow and the atmosphere, the next step was controlling the surface temperature by using the heat flux at the surface boundary instead of fixed temperatures. To achieve this, a ghost cell was added outside the surface boundary $\left(u(x_{0-\Delta x},t)\right)$ to allow for a central difference approximation of the snow surface temperature value ($u(x_0,t)$). The temperature of the ghost cell can be manipulated such that the gradient through the surface allows for the correct heat flux being conducted through the boundary. The temperature gradient is based on the difference between cells $u(x_{0-\Delta x},t)$ and $u(x_{0+\Delta x},t)$. This method assumes that the heat flux at the surface is consistent a

small distance (Δx) from the surface into the snowpack. The accuracy of this assumption inversely dependent on the value of Δx because of snows insulating properties. The ghost cell formula is derived from the equation for thermal conduction (1):

$$q = \frac{k_e \Delta T}{L}$$

(22)

Where: q = heat flux [W/m^2

k_e = effective thermal conductivity [W/mK]

ΔT = temperature gradient [K/m]

L = length [m]

Substituting the terms in equation (22) the ghost cell formula is given by:

$$q = k_e \frac{u(x_{0-\Delta x}, t) - u(x_{0+\Delta x}, t)}{2\Delta x}$$

$$\frac{2\Delta x}{k_e} \times q = u(x_{0-\Delta x}, t) - u(x_{0+\Delta x}, t)$$

$$u(x_{0-\Delta x}, t) = q\frac{2\Delta x}{k_e} + u(x_{0+\Delta x}, t)$$

(23)

3.1.3. Implementing the terms of the energy balance equation

In theory chapter 2.2. the equation for energy balance in a snowpack is presented. To predict temperature evolutions in an accurate manner, each of the terms should be considered in the model. The energy exchange between the snowpack and the environment occurs mainly at the surface, as discussed in chapter 2.2.1 and 2.2.6 shortwave radiation and ground heat flux contributes to heating at depth. Because of low temperature gradients at the bottom of the snowpack, the ground heat flux is small compared to energy supplied by the sun. Estimates based on modeled snowpack temperatures during the 1st of April period suggest the ground supplied heat equals to 2% of the total absorbed solar radiation during a 24-hour.

Ground heat flux is implemented by a fixed static boundary condition at the bottom of the snowpack.

Shortwave radiation is implemented by equation (5), where the amount of penetrating shortwave radiation is distributed among the layers by the equation:

$$\Delta I_x = I(x) - I(x + \Delta x)$$

(24)

Where x is the depth of the given segment in meters. For the cells within the domain, the increase in temperature from shortwave radiation is calculated by considering how much the added shortwave radiation energy in isolation would heat the given layer. This was done by using the formula for specific heat capacity:

$$Q = mc\Delta T$$

(25)

Where: Q = heat [Joules]

c = specific heat capacity [J/m K]

ΔT = change in temperature [K]

The mass of the given layer is calculated based on the assumption that each of the model segment can be considered a three-dimensional layer with a unit base area. The added energy is calculated by multiplying the heat flux from ΔI with Δt. The equation for the increase in temperature by shortwave radiation is given by:

$$q\Delta t = mc\Delta T$$

$$\Delta T = \frac{q\Delta t}{mc}$$

$$\Delta T = \frac{\Delta I\ \Delta t}{\rho_s\ \Delta x\ c}$$

(26)

Where: q = heat flux [W/m^2]

m = mass [kg]

ρ = snow density [kg/m^3]

c = Specific heat capacity of ice [J /kg K]

For simplicity, the penetrating solar flux is assumed to be constant for each time step of the calculation. Consequently, the margin of error is dependent on the value of Δt. With a small enough value, the change in incoming shortwave radiation during each step forward in time becomes negligible. Combining equation (26) and (20) the final equation for cells within the model domain (except for cells representing the surface ($u(x_0, t)$)), temperature is given by:

$$u(x, t + \Delta t) = \left(u(x, t) + \alpha \frac{\Delta t}{\Delta x^2} \left(u(x + \Delta x, t) - 2u(x, t) + u(x - \Delta x, t)\right)\right) + \frac{\Delta I \, \Delta t}{\rho_s \, \Delta x \, c}$$

(27)

For the surface boundary condition, the energy terms considered for the surface heat flux is given by:

$$q = \Delta I_{x=0} + LW_{net} + Q_h$$

Where $I\Delta$ is the depth distributed shortwave radiation [W/m^2], LW_{net} is net longwave radiation [W/m^2] and Q_h is the sensible heat flux. For simplicity, the model assumes that latent heat is constant. In chapter 3.2. it is discussed how incoming and outgoing shortwave and longwave radiation from the snow surface at our field location was measured. Air temperature was also measured and used to calculate sensible heat flux as presented in chapter 2.2.3. Because high frequency wind data was not measured at the field location, windspeeds was computed as a fitting parameter for the sensible heat calculation, in order to create surface temperatures which was consistent with the measured outgoing longwave radiation. The simulated outgoing longwave values were calculated from the modeled surface temperatures by equation (6):

$$LW_{out\ cal.} = \varepsilon \sigma (u(x_0, t))^4$$

Where $u(x_0, t)$ is the surface temperature at a given time [^{o}K]. Assuming that the real snow surface temperature is dependent on the present heat flux, which is also true for the model, computed LW_{out} values can be used as an indicator of model performance. If the modeled surface runs to cold, more sensible heat is applied by increasing the wind speed, inversely windspeed is reduced if model runs to hot. The model performance using fixed sensible heat, fixed windspeed and variable windspeed is presented and discussed in chapter 4.3.2. Variable wind values for the sensible heat calculation (equation (8) and(10)) is computed by the following if-condition:

If:

$$LW_{out\ real} < LW_{out\ cal.}$$

Then:

$$w_t = w_{t-\Delta t} - a$$

Else:

$$w_t = w_{t-\Delta t} + a$$

Where: $LW_{out\ real}$ = the measured outgoing longwave [W/m^2]

$LW_{out\ cal.}$ = the computed outgoing longwave value [W/m^2]

w_t = the windspeed for the given time with the model [m/s]

$w_{t-\Delta t}$ = windspeed at previous time step [m/s]

a = constant for windspeed adjustment [m/s]

When all the calculated and measured energy terms are implemented into the ghost cell equation (23), it takes the form as:

$$u(x_{0-\Delta x}, t) = \left(\Delta I_{x=0} + \left(LW_{in} - (LW_{out\ cal.})\right) + Q_h\right) \frac{2\Delta x}{k_e} + u(x_{0+\Delta x}, t)$$

(28)

3.1.4. Calculating vapor pressure

Vapor pressure was calculated by using the same method as presented by Birkeland et al. (1998). By assuming that pore space in the snow is saturated with vapor, equilibrium vapor pressure with respect to a flat ice surface at given temperature can be calculated using the Goff-Gratch formulation. Pinzer et al. (2012) supports the assumption of a flat interface by stating Kelvin effects only play a role for grains with a radius of curvature less than 10^{-7} m. The formula for vapor pressure is:

$$\log_{10} e_i = -9{,}09718\left(\left(\frac{T_0}{T}\right) - 1\right) - 3{,}56654 \log_{10}\left(\frac{T_0}{T}\right) + 0{,}876793\left(1 - \left(\frac{T}{T_0}\right)\right) + \log_{10} e_{io}$$

(29)

Where: e_i = Equilibrium vapor pressure for a flat ice surface [mb]

T = Absolute temperature [°K]

T_0 = Ice-point temperature (273,16 °K)

e_{io} = Equilibrium vapor pressure at ice-point temperature (6,1071 mb)

3.1.5. Calculating growth rate of faceting

To define a function for the growth rate for faceting a minimum threshold value of 5 mb/m was used, according to the findings of LaChapelle and Armstrong (1977). Due to the difficulty of defining the size of faceted crystals, the findings of Fukuzawa and Akitaya (1993) and Marbouty (1980), who defined snow crystal size similarly, were used. Their results were recalculated to get values for growth rate in nm/s and vapor pressure gradient in mb/m. GeoGebra and R were used to plot facet growth rates against vapor pressure gradients and perform regression analyses. The equation for facet growth rate, f(v), takes the form:

$$f(v) = a\ln(v) + b \tag{30}$$

Where: v = vapor pressure gradient [mb/m] between $u(x,t)$ and $u(x+\Delta x,t)$

a = constant

b = constant

Vapor pressure gradient between $u(x,t)$ and $u(x+\Delta x,t)$ is calculated by:

$$v = \frac{e_{ix} - e_{ix+\Delta x}}{\Delta x} \tag{31}$$

Where $e_i$is calculated using equation (29).

To calculate the growth rate at $u(x,t)$, the following equations was used:

For v > 5 mb/m:

$$f(v) = a \ln(v) + b$$

(32)

For v < -5 mb/m:

$$f(v) = -1\,(a \ln(|v|) + b)$$

(33)

For -5 mb/m < v < 5mb/m:

$$f(v) = 0$$

(34)

Equation (32) calculates growth rates when the vapor pressure gradient is positive and above the threshold vapor pressure gradient required for faceting. Under the snow crystals there is sublimation, while over the crystals there is deposition, and faceting happens on the top side. Equation (33) represents the opposite. Vapor pressure gradient is above the threshold for faceting, but in the opposite direction. Individual snow crystals experience sublimation on the top and deposition on the bottom.

3.2. Field work

The purpose of the field work was to gather data from a snowpack to calibrate and tune the model. A CNR4 radiometer and five Tinytag temperature loggers were installed 9th of March and logged for nearly a month to 7th of April. The field period lasted from 00:00 the 11th to 14:00 the 12th of March. The data collected during the field period were manual temperature measurements of the snowpack taken every other hour, density measurements, and extinction measurements of shortwave radiation in the snow.

3.2.1. Locality

The field work was conducted by Slakkafjellet in Sogndal municipality, at the northwest corner of Statnett's electrical substation (Figure 6 and Figure 7). This locality was chosen due to the practicality of having road access and electricity, while still being at a relatively high altitude (720 m.a.s.l.). This made for easy access and a longer snow season. Statnett kindly lent us an outlet at their cabin, which powered the heater and ventilation unit of the radiometer.

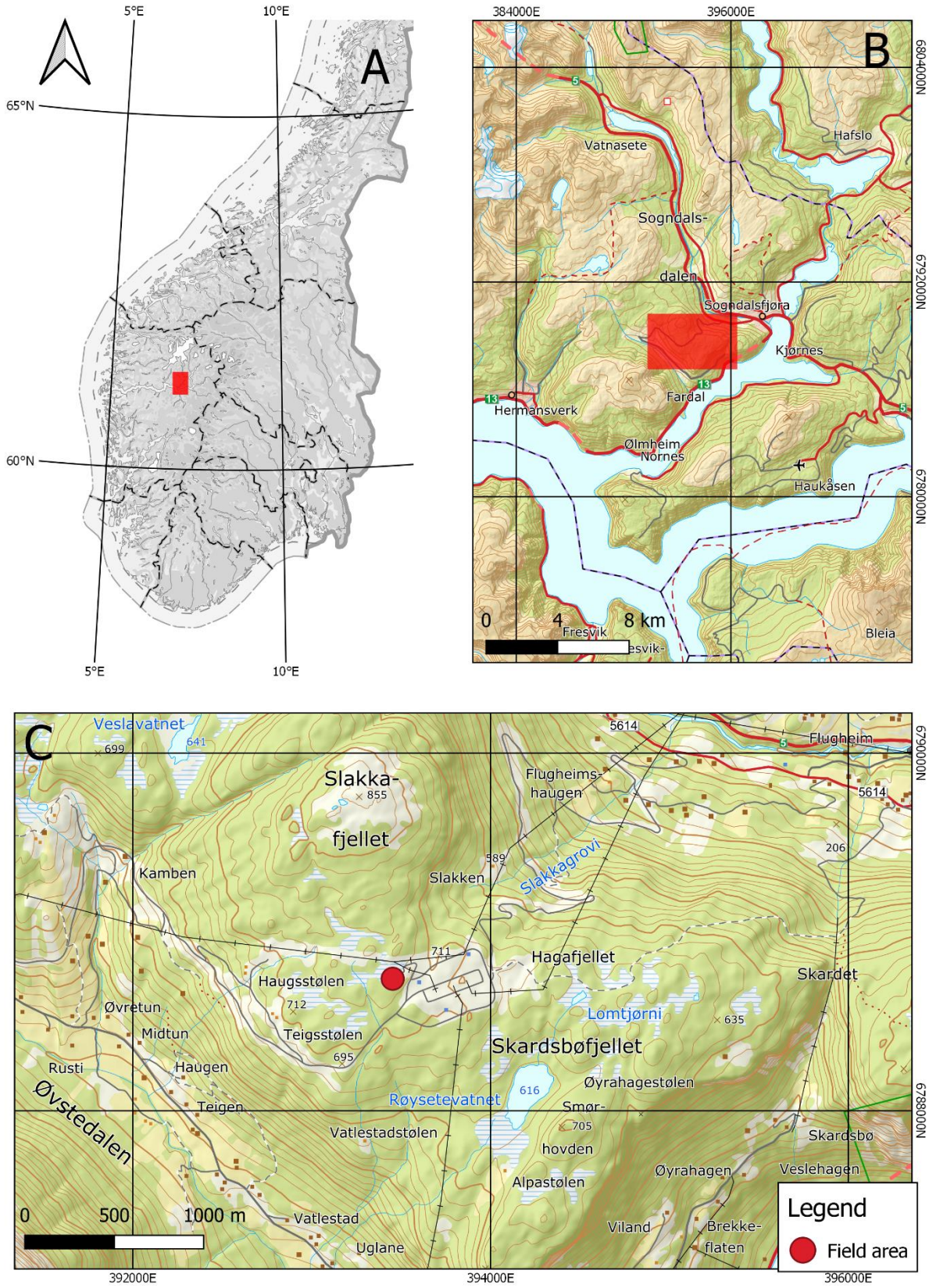

Figure 6: Overview map of the field area.

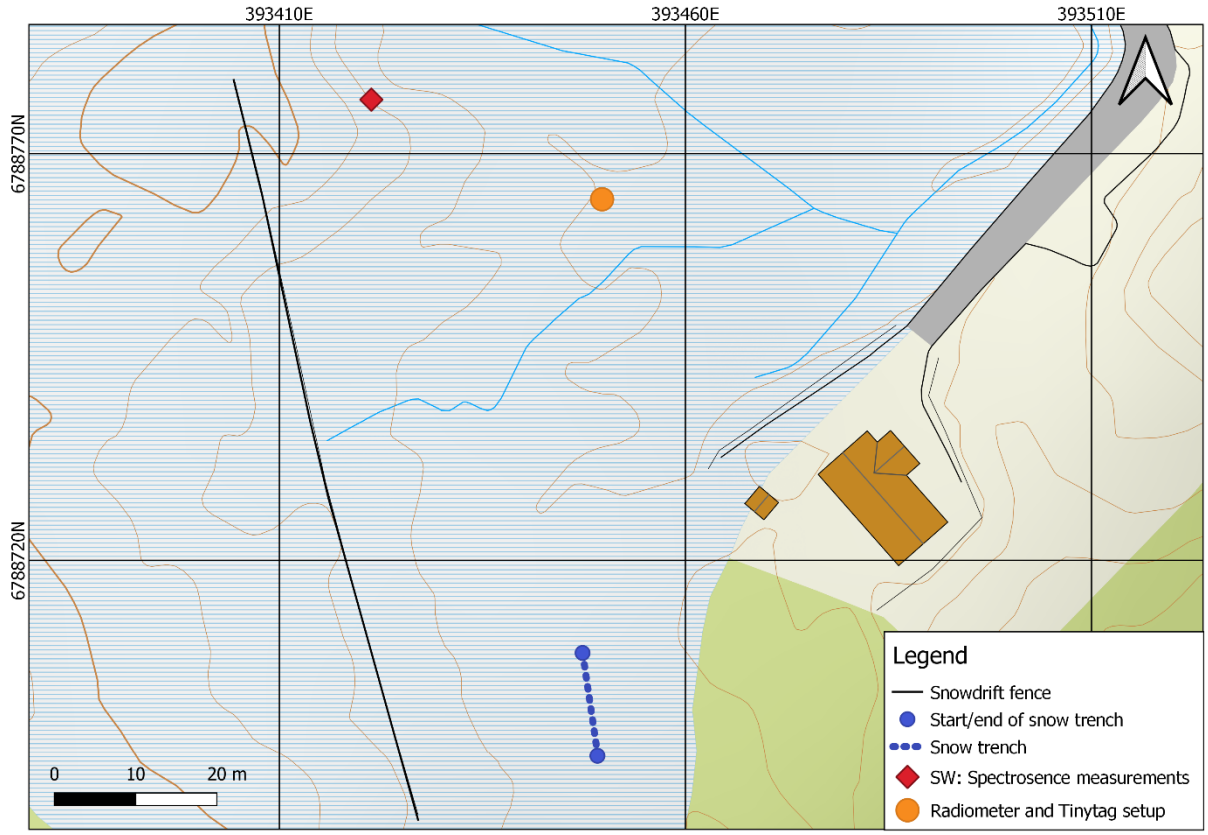

Figure 7 Experimental setup at the field site.

3.2.2. Experimental setup

For the logging section of our setup, a CNR 4 Net Radiometer connected to a Logbox SE was used to measure and log incoming and outgoing shortwave and longwave radiation (Figure 8). The wiring between the radiometer and the Logbox can be seen in Appendix 7.1. The radiometer consisted of two pyranometers, one facing up and one down, for shortwave radiation. Likewise, it had two pyrgeometers, one facing up and one down, to measure longwave radiation. The radiometer was mounted 150 cm above the snow surface on an aluminum pole stuck in the ground at the orange point in Figure 7. On the installation day, 7th of April, the snow was 150 cm deep at the field site. The radiometer was mounted on the south side of the pole to keep shading effects from the instrument and setup to a minimum. An area was cordoned off to keep the snow undisturbed (Figure 9). The radiometer was approached from the north during installation and checkups, to keep the snow surface under the instrument as smooth as possible.

There are two main sources of error for the pyrgeometer (Kipp & Zonen, n.d.-a). The thermopile in the

pyrgeometer measures the difference between its own temperature and what it “sees”. On sunny days the upper pyrgeometer window will absorb incoming solar radiation and may heat up. This will then radiate inwards and can cause and error of up to 6 W/m^2. The second, and major cause of error in the pyrgeometer is water deposition on the pyrgeometer window. This will set the signal to about zero and during clear, windless nights frost or dew formation on the window can give an error of more than 100 W/m^2. To prevent these errors, a CNF Ventilation Unit was installed, which heats and ventilates the instruments. Ventilation reduces the error due to heating the pyrgeometer window and keeps the windows clear from precipitation, while heating keeps the window above the dew point. Errors in the pyranometer readings due to use of the CNF 4 are negligible (Kipp & Zonen, n.d.-a). When carrying out the field work, photos were taken of the pyranometer and pyrgeometer domes and windows regularly to see if frost or dew had formed, in case the CNF 4 Ventilation Unit did not work as intended.

Figure 8 Setup of logging equipment looking west. CNR4 Net Radiometer on the left connected to a Logbox SE. Two Tinytag temperature loggers at about 10 cm (logger C) and 150 cm (logger B) from the snow surface, inside white sun shields. Wiring and Tinytags are tied to the north side of the pole to limit shading effects on the radiometer. This photo was taken the 7th of April, right before dismantling.

Figure 9 Cordoned off area.

In addition to the radiometer, five Tinytag temperature loggers were set up. Three were placed in the snowpack without sun shields. One at the bottom of the 150 cm deep snowpack (E), one 100 cm deep (D), and one 30 cm deep (A) connected to the aluminum pole with a rope to make retrieval easier (Figure 10). To prevent the aluminum pole to influence the temperature measurements, the Tinytags were placed 50 cm or more from the pole. Two Tinytags were placed 10 cm (C) and 150 cm (B) above the snow surface in sun shields to measure air temperature (Figure 8). The Tinytags and the wiring of the radiometer were tied to the north side of the pole to avoid shading the area underneath the radiometer.

Figure 10 Placement of Tinytags below the snow surface. Logger E was placed at the bottom of the 150 cm deep snowpack. Logger D was placed 50 cm higher, at 100 cm depth. Logger A was placed at 30 cm depth. All the Tinytag loggers were tied to the aluminum pole seen to the upper left.

3.2.3. Manual temperature measurements

The manual temperature measurements were taken with a "thermoplank" consisting of eight thermometers mounted to a plank (Figure 11). Table 1 shows how far apart the tips of the thermometers were when mounted to the plank. Thermometer H was accidentally mounted at a slight angle, so the end was 0,5 cm off the intended position. All other thermometers were within 1 mm of the intended position. The top three thermometers were spaced closer than the rest to attain a higher level of detail of the near-surface measurements. The thermometers were calibrated by putting them in a bowl with water mixed with snow, a temperature assumed to be close to 0,0°C. The errors were noted of each thermometer and the individual calibration constants were applied to the gathered data in the processing stage.

A handheld IR thermometer were used to measure snow surface temperatures (photo in Appendix 7.2.). The input needed for the IR thermometer was a value for emissivity. The product manual suggested a value of 0,83 for snow, which were used for all measurements. This contradicts the emissivity values mentioned in section 2.2.2.

Table 1 Thermometer distances

Thermometer	Distance from surface
A	1 cm
B	3 cm
C	5 cm
D	10 cm
E	15 cm
F	20 cm
H	24,5 cm
G	30 cm

Figure 11 The "Thermoplank". Eight thermometers mounted to a plank to make temperature measurements in a snow profile more efficient. Each thermometer is labelled with a letter to distinguish them in the data.

Snow temperatures were measured with the “thermoplank” and the IR thermometer every other hour from 00:00 the 11.03.22 to 14:00 the next day in the shaded, north facing wall of the trench shown on the map in Figure 7 and in Figure 12. Since the “thermoplank” was 29 cm long, measuring thrice gave a total measuring depth of 88 cm. The measurements overlapped, so thermometer A measured at the same depth as thermometer G’s last measurement, giving two measurements at 30 cm depth and 59 cm depth.

During the night, one 88 cm temperature measurement was taken. While the sun was up, the measurements were taken once with sun on the snow surface, once directly after shading the surface, and once 20-30 min after shading. During the measurements, the thermometers were let in the snow to equilibrate to their new temperature until they seemed stable. This process was filmed, and the data collected from the videos were all taken 60-90 seconds after the thermometers were placed in the trench wall. At least 60 cm of snow was removed before each measurement, to reach snow that had not yet been affected by the trench (Figure 12).

Potential errors for the manual temperature measurements include weaknesses in the construction of the "Thermoplank" as well as human measurement error. When sticking the thermometer in the snow, the thermometer tips may have been forced slightly out of line, perhaps up to 2 mm. Thermometer H likely experienced the largest error caused by this effect due to its slightly crooked mounting. A second error source for our manual measurements is the placement of the first thermometer compared to the snow surface. The intention was for thermometer A to measure at 1 cm depth, but an error of up to 5 mm may have occurred.

Figure 12 Snow trench for temperature measurements. Photo taken at 11:39. Fun fact: six tons of snow was moved at this location.

3.2.4. Measuring shortwave extinction

As discussed in section 2.2.1., short wave radiation decreases exponentially with depth in the upper 10 cm of the snowpack. To get a function for this decrease, penetrating shortwave radiation was measured with a

Skye Spectrosense 2+ pyranometer. The pyranometer measured incoming SW radiation through a nearly undisturbed snowpack from below in a snow cave by digging 1,2 m horizontally into the side of a hill and shaving off snow from the ceiling (Figure 13). When recording a value from the upper pyranometer, the instrument was held as level as possible. It was held flush with the ceiling of the snow cave to limit light coming in from the sides or reflecting from below.

The main weakness to this method was that the top 15 cm were the most important and also the most difficult to measure. The recorded depths may be off by up to 5 mm. An avalanche probe was used to measure the remaining distance to the surface. This may have affected the values for SW radiation. A hole from an earlier probing can be seen to the right in Figure 13. This might have let additional SW radiation penetrate deeper than in an undisturbed snowpack.

Figure 13 Measuring shortwave radiation penetration with the Skye Spectrosense 2+.

3.2.5. Snow density measurements

Snow density was measured by using a plastic box with a volume of 2,2 L and a weight of 49 grams. A digital scale was used to measure each sample. The samples were taken successively deeper, with the start and end depths for each sample recorded.

The main source of error for the density measurements is that the plastic box was not rigid. This means that the volume was not constant for each measurement. A second source of error is that the snow was slightly compacted when putting it in the box. Both errors are relatively small, but a reduction in error is expected with the use of a professional snow density measurement kit.

3.3. Processing radiometer data

3.3.1. Calculation of irradiance

The output from the pyranometers and pyrgeometers is mV. To convert this to the desired W/m^2 a series of calculations need to be made. Calculating the irradiance for the pyranometers is done by equation (35):

$$E_{SW} = \frac{\mathrm{U_{emf}} \times 1000}{\mathrm{S}} \quad (35)$$

Where E_{SW} is shortwave radiation in W/m^2, U_{emf} is output voltage in mV, and S is the sensitivity of the pyranometer in $\frac{\mu V}{W/m^2}$. The sensitivities of the pyranometers and pyrgeometers can be found in Appendix 7.3.

Calculating irradiance for the pyrgeometers is a more complex matter. The calculation is done with equation (36):

$$E_{LW} = \frac{\mathrm{U_{emf}} \times 1000}{\mathrm{S}} + \sigma \times T_b^4 \quad (36)$$

Where E_{LW} is longwave radiation in W/m^2, U_{emf} is output voltage in mV, and S is the sensitivity of the pyrgeometer in $\frac{\mu V}{W/m^2}$, σ is the Stefan-Boltzmann constant $\left(5{,}67 \times 10^{-8} \frac{W}{m^2 K^4}\right)$, and T_b is the body temperature of the instrument in K. Since we used the thermistor to measure the body temperature of the instrument, as explained in Appendix 7.1, T_b is given by equation (37) (Kipp & Zonen, n.d.-b).

$$T_b = (\alpha + [\beta \times (\ln(R)) + \gamma \times (\ln(R))^3])^{-1}$$

(37)

Where:

$\alpha = ,0295 \times 10^{-3}$

$\beta = 2{,}391 \times 10^{-4}$

$\gamma = 1{,}568 \times 10^{-7}$

R = Resistance

Resistance is calculated using the following equation:

$$R = \frac{VREF \times c}{U_{emf}} - c$$

(38)

Where VREF is the excitation voltage (in our case 2500 mV), U_{emf} is the output voltage from the thermistor in mV, and c is the 10k parallel with input impedance. As mentioned in Appendix 7.1., we wired the thermistor to AIN4 in the Logbox SE. AIN3 and AIN4 have and internal voltage divider and therefore 13,2 kΩ input impedance (Kipp & Zonen, 2020). c is given by the following equation:

$$c = \frac{10000 \times 13200}{10000 + 13200}$$

(39)

3.3.2. Calculating albedo, net radiation, and snow surface temperatures

Albedo is calculated by:

$$Albedo = \frac{E_{SWdown}}{E_{SWup}}$$

(40)

Where E_{SWdown} is the irradiance from the downwards facing pyranometer in W/m^2 and E_{SWup} is the irradiance from the upwards facing pyranometer.

Net SW radiation is calculated by:

$$E_{netSW} = E_{SWup} - E_{SWdown}$$

(41)

Net LW radiation is calculated by:

$$E_{netLW} = E_{LWup} - E_{LWdown}$$

(42)

Where E_{LWdown} is the irradiance from the downwards facing pyrgeometer in W/m^2 and E_{LWup} is the irradiance from the upwards facing pyrgeometer.

Net radiation is calculated by:

$$E_{net} = E_{SWup} - E_{SWdown} + E_{LWup} - E_{LWdown}$$

(43)

Snow surface temperatures, T_s, are calculated by solving for T in the Stefan-Boltzmann equation and converting from K to C:

$$T_s = \left(\frac{E_{LWdown}}{5{,}67 \times 10^{-8}}\right)^{\frac{1}{4}} - 273{,}15$$

(44)

3.4. Processing Skye Spectrosense 2+ data

GeoGebra was used to process the incoming shortwave radiation data from Skye Spectrosense 2+ pyranometer. Each measurement was manually plotted in a spreadsheet before using regression analysis to express solar extinction as a natural exponential function with depth in meters on the x-axis and radiation W/m^2 on the y-axis. The suggested function did not account for all the penetrating SW radiation, so the function was adjusted to intersect the y-axis at the total amount of penetrating solar radiation.

4. Results and discussion

In the period 9th of March to 7th of April 2022, automated temperature and radiation measurements were conducted at Slakkafjellet. The air temperature data from for the whole period is shown in Figure 14, gathered from Tinytag logger B, mounted 150 centimeters above the snow surface. The manual field work took place from 00:00 on the 11th of March to 14:00 12th of March. The second period of interest is named the "1st of April period" which spans from 00:00 30th of March to 23:59 the 1st of April. Simulation of the snowpack was performed based on radiometer and Tinytag data.

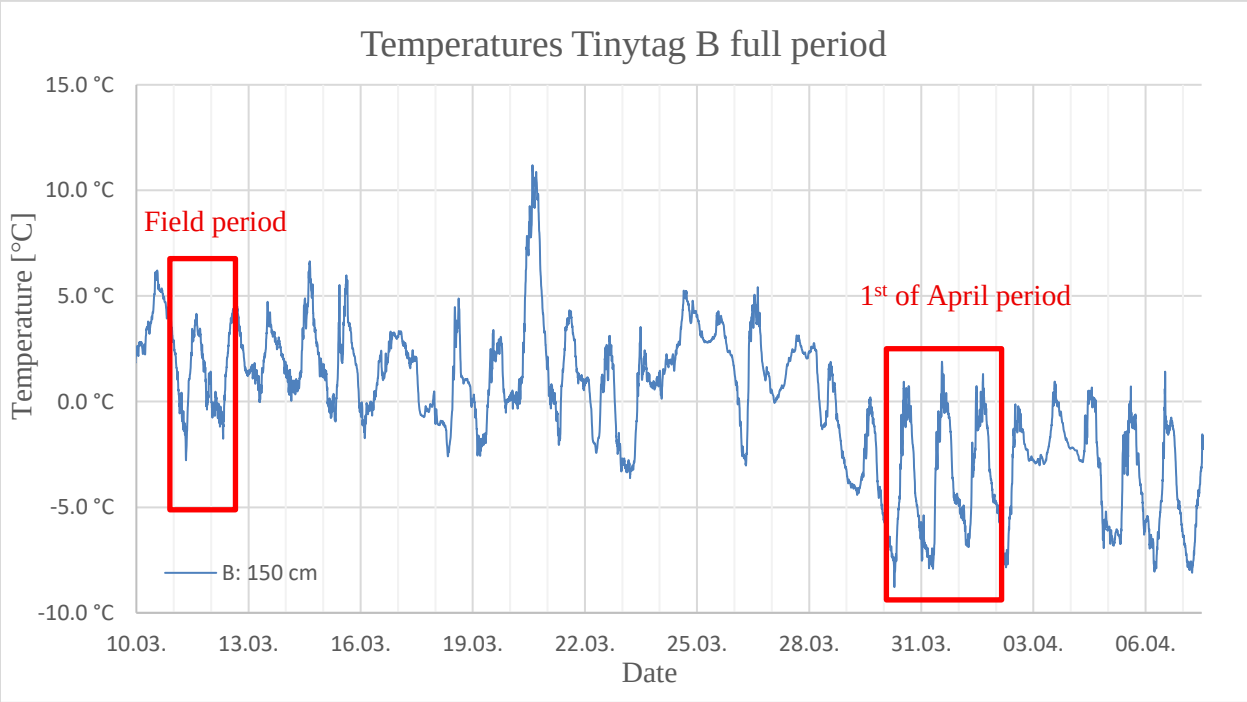

Figure 14 Temperatures from Tinytag B for the full measuring period. The field period and the 1st of April period are marked in red boxes respectively left and right.

4.1. Theoretical results

4.1.1. Function for facet growth rate

The function of growth rate is presents in Figure 15 and given by:

$$f(x) = 1{,}0987 \ln(x) - 1{,}7452$$

(45)

Using R, a logarithmic fit gives an R-value of 0,90 ($p < 0{,}001$), which means that 90% of the change in facet growth rate can be explained by the relationship with vapor pressure gradient. A linear fit is only slightly worse, with an R-value of 0,89 ($p < 0{,}001$).

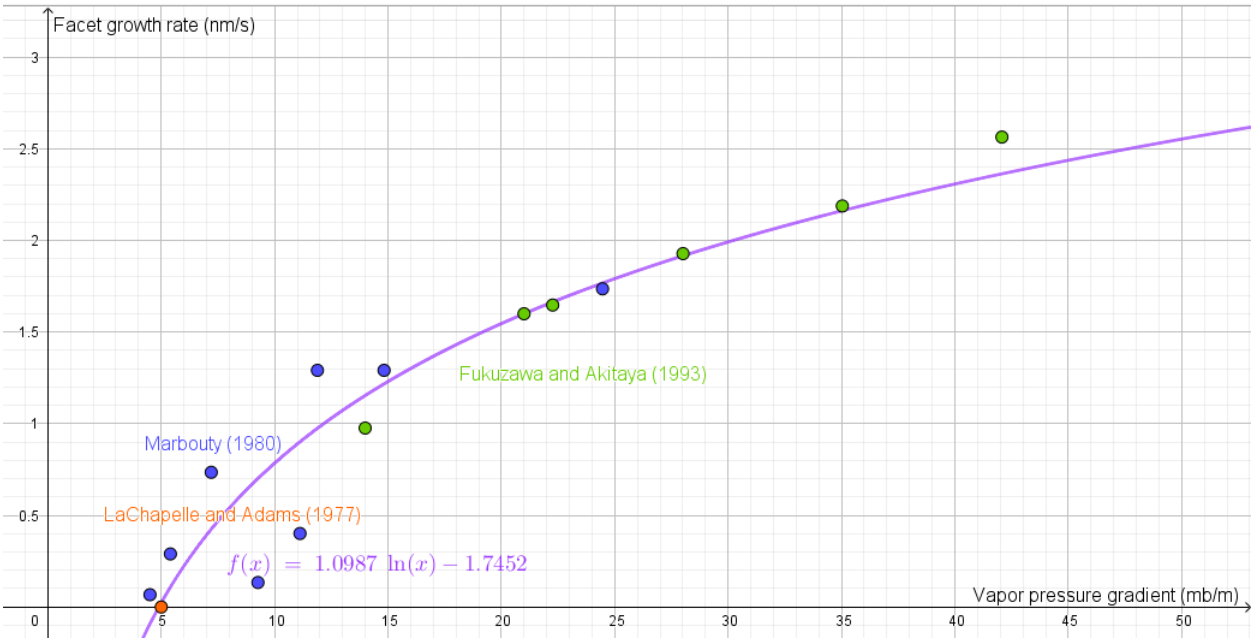

Figure 15 Function for facet growth rate.

The logarithmic function is used because has a higher R-value and intersects the x-axis nearly at 5 mb/m (4,89602 mb/m), the threshold vapor pressure gradient required for faceting. In this thesis, the effect of rounding is considered negligible, the growth is considered to be zero under the threshold vapor pressure gradient. As an extension of this study, it is recommended to look into what happens to the snow when the vapor pressure gradient is under threshold values.

4.1.2. Simulation of Pinzer and Schneebeli (2009) experiment

The simulation was based on Pinzer and Schneebeli's (2009) S2 experiment. The initial conditions were -2,3°C throughout the whole snow, the mean temperature of the snow. The peak temperature gradient is ±87°C/m and the calculated peak vapor pressure gradient is 39 mb/m for the top half of the snow, and -39 mb/m for the bottom half. The upper and lower boundary condition are two equal but opposite sinusoidal functions by the equation:

$$BC(x) = \pm 0{,}87 \sin\left(\frac{\pi}{12}\, x\right) - 2{,}3$$

(46)

Simulation parameters can be seen in Table 2. Resulting temperature profiles over time can be seen in Figure 16. The symmetrical nature of the temperature oscillations leads to temperature profiles that appear linear, though they are, in fact, slightly curved due to the propagation time needed for temperature changes far from the surfaces. The mean temperature is -2,3°C, and therefore the "root point" in the center stays at -2,3°C.

Table 2 Pinzer and Shcneebeli simulation parameters

Variables		**Units**	**Values**
Thermal diffusivity	α	$[m^2/s]$	$1{,}9529 \times 10^{-7}$
Heat capacity	c	[J/K]	2090
Density	ρ_s	$[kg/m^3]$	245
Effective thermal conductivity	k_{eff}	[W/m*K]	0,1
Delta x	Δx	[m]	0,002
Delta t	Δt	[s]	10
Total Depth	x_{max}	[m]	0,02
Duration	t_{max}	Hours	48

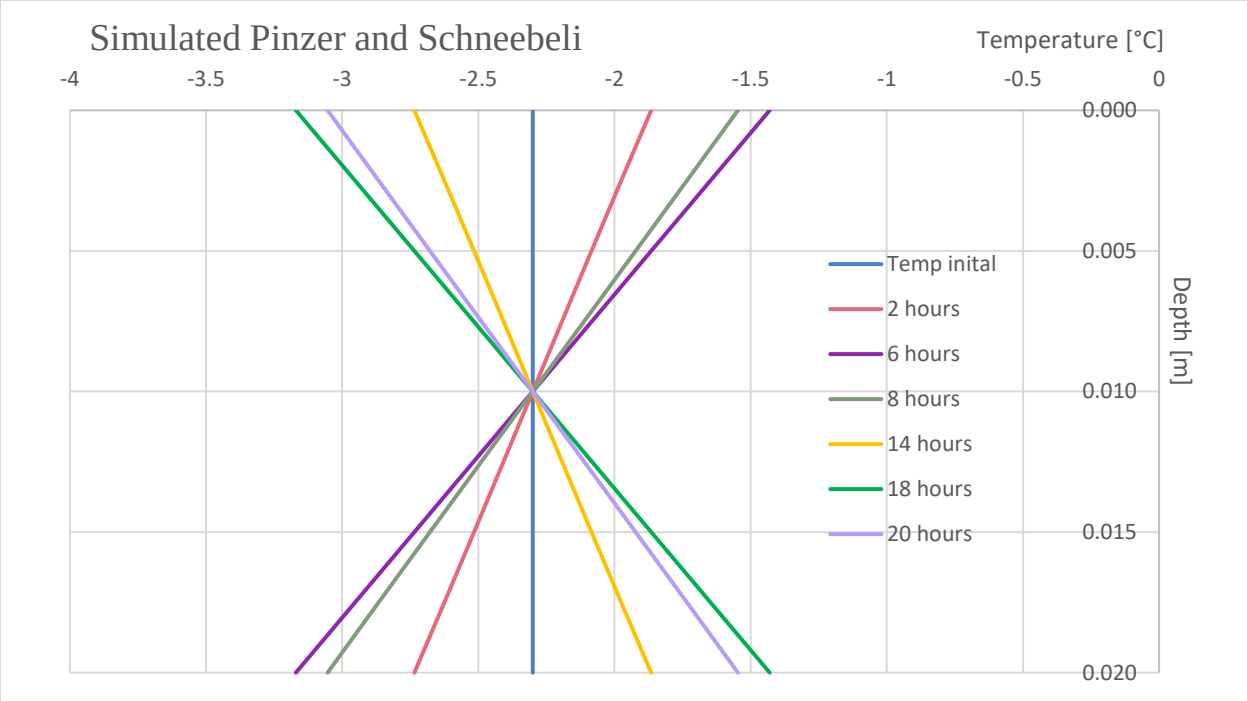

Figure 16 Simulated of Pinzer and Schneebeli (2009) S2 experiment.

The result of net faceting for 24 hours is shown in Figure 17. It shows a linear curve between 0,00358 mm of positive growth at the top of the simulated snow sample to 0,00358 mm of negative growth at the bottom of the sample. At the center of the sample, the net growth is 0 mm.

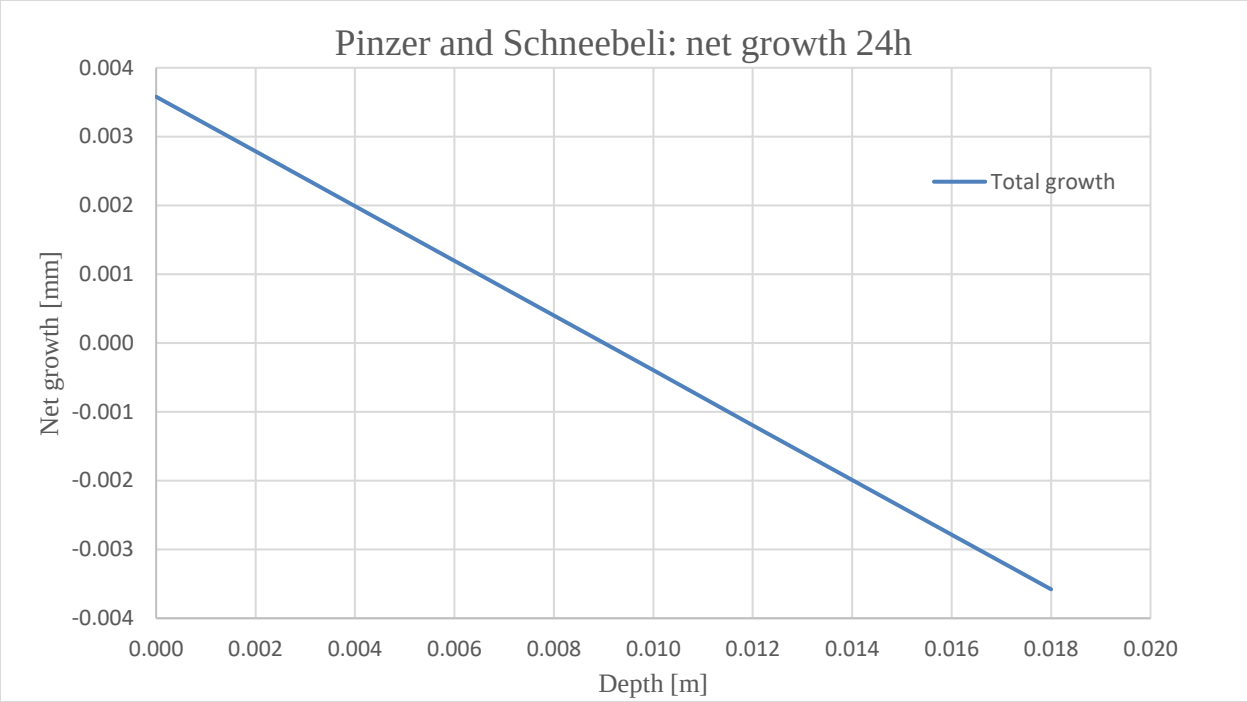

Figure 17 Pinzer and Schneebeli (2009) net facet growth of the S2 experiment.

The presence of net facet growth from simulating the Pinzer and Schneebeli (2009) experiment was initially a surprise, since it was assumed (incorrectly) that the symmetrical nature of their experiment would lead all facet growth to be reversed when the vapor pressure gradient switched sign. It can be explained, however, by considering the effect of temperature. In Figure 16, when the snow at the top of the sample is at its warmest, the temperature gradient is positive. This gives increased vapor pressure gradients in the positive direction and net positive faceting occurs. The effective conductivity of snow transfers heat through the sample so quickly that negative gradients of temperature and vapor pressure at the top of the sample remain miniscule until the surface has cooled to -2,3°C and the temperature gradient throughout the sample becomes negative. The same process, with opposite sign seems to be at work in the bottom half of the sample. When the bottom snow is at its warmest, the temperature gradient is negative, giving higher negative vapor pressure gradients, growth rates and a net negative growth. In a way, the Pinzer and Schneebeli (2009) simulation isolated the effect of temperature (hypothesis 1).

Figure 18 shows the growth rates over time of the top and bottom 2 mm of the snow sample from the simulation of Pinzer and Schneebeli's (2009) experiment. The growth rates for the middle of the sample are not shown in Figure 18 to not crowd the graph, but they lie between the growth rates for the top and bottom 2 mm. The curve for growth rate 0-2 mm peaks on the positive side at 2,28 nm/s. The peak negative growth for 0-2 mm is 2,15 nm/s. Between 18-20 mm the sample experiences the same, but with

opposite sign. The peak positive growth rate between 18-20 mm is 2,15 nm/s, while the peak negative growth is 2,28 nm/s. The flat sections at 0, 12, and 24 hours with growth rates equal to 0 nm/s are when the snow sample experienced vapor pressure gradients below 5 mb/m (4,89602 mb/m as presented in 4.1.1) and the function for facet growth rate (equation (45)) gives 0 nm/s

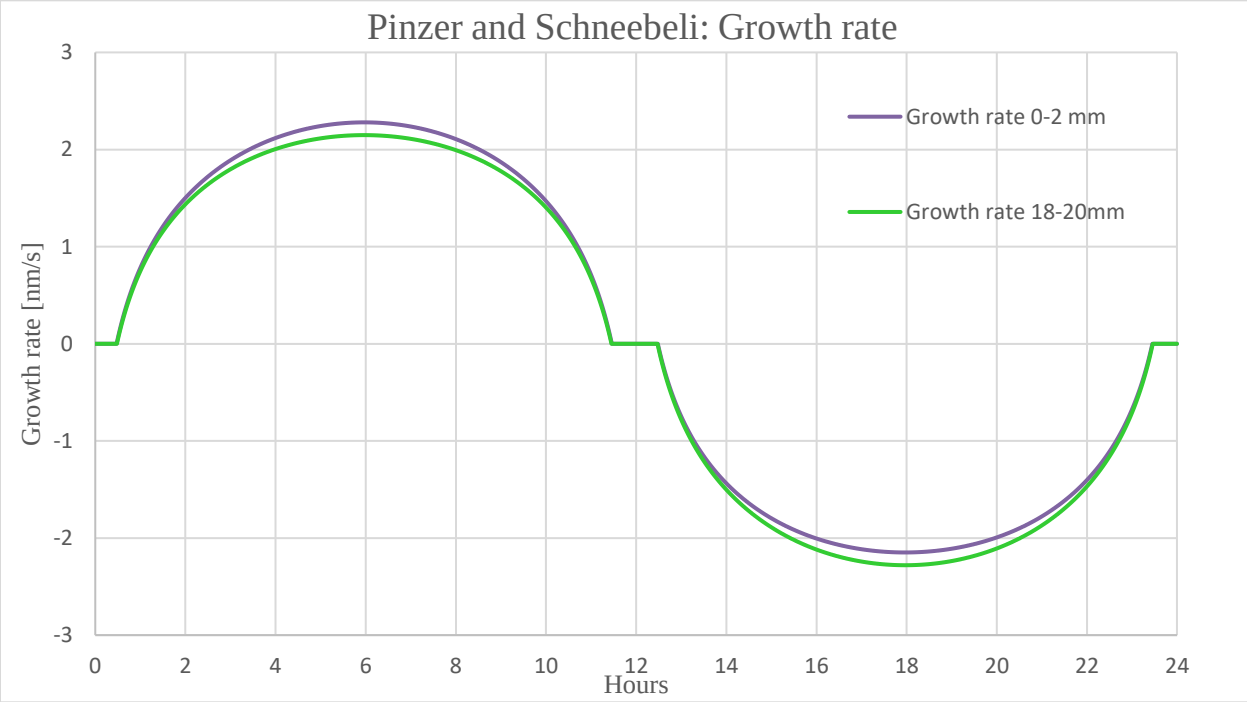

Figure 18 Pinzer and Schneebeli (2009) growth rates at top and bottom 2 mm of the snow cylinder.

Figure 18 indicates that the entire simulated snow sample experienced large and nearly equal positive and negative growth rates for most of the experiment. The area between the two curves shows the difference in growth between the top and bottom of the sample, with net positive growth on the top and net negative growth on the bottom. The (not shown) curve of growth rate at the center of the snow sample has equal areas under the positive and negative sides, meaning all positive growth gets reversed by the subsequent negative growth.

The model does not take rounding into account, which may play a part in lowering net facet growth. If at the 12-hour mark, the snow at the top of the sample, which has grown more, rounds more than the snow at the bottom, which has grown less, the difference in growth rate may be compensated for to some degree. It seems likely, however, that this effect is minimal, due to the short time spent in “rounding mode” compared to faceting.

A potentially significant reason that Pinzer and Schneebeli (2009) did not observe faceting during their experiment is that when taking µCT scans, they did this near the center of their snow sample, where according to the simulated results in this thesis, facet growth was nearly zero. Had the µCT scans been taken closer to the boundaries, they may have observed more faceting. On the other hand, only the results from 24 hours, one cycle of the sinusoidal temperature oscillations, are shown here. Pinzer and Schneebeli (2009) ran their experiment for approximately 14 days. The net growth after 14 days should be 14 times that for 24 hours. This would equal around 0,02 mm of facet growth in the section scanned, which may be enough to be noticeable in a µCT scan. For µCT scans taken after half a cycle, facet growth should perhaps be visible. Further investigation is needed.

4.1.3. Simulation: sinusoidal temperature oscillations / The effect of temperature

A simulation was run with fixed boundary conditions and the parameters found in Table 3. It was controlled by sinusoidally oscillating surface temperatures between -19°C and -1°C and fixing the bottom of the snowpack at 0°C. Initial conditions were chosen by using linearly interpolated temperatures between the surface at -19°C and the bottom at 0°C, then running the simulation until the temperature profile equilibrated (ca. 100 cycles). The profiles were defined to be equilibrated when the difference between IC temperatures and final temperatures were equal down to six decimal points. The simulated temperatures can be seen in Figure 19. The mean temperature at the snow surface is -10°C, and it increases with depth. This shows that the mean temperature gradient for the whole snowpack is negative. Since this is a purely theoretical approach, the temperatures and times do not match with any measured data. The coldest surface temperature was set to 02:00, with the simulation running until 01:58 the next day.

Table 3 Parameters for simulating sinusoidal temperatures.

Variables		**Units**	**Values**
Thermal diffusivity	α	$[m^2/s]$	$2{,}39*10^{-7}$
Heat capacity	c	[J/K]	2090
Density	ρ_s	$[kg/m^3]$	200
Effective thermal conductivity	k_{eff}	[W/m*K]	0,2
Delta x	Δx	[m]	0,01

Delta t	Δt	[s]	120
Total Depth	x_{max}	[m]	1
Duration	t_{max}	hours	24

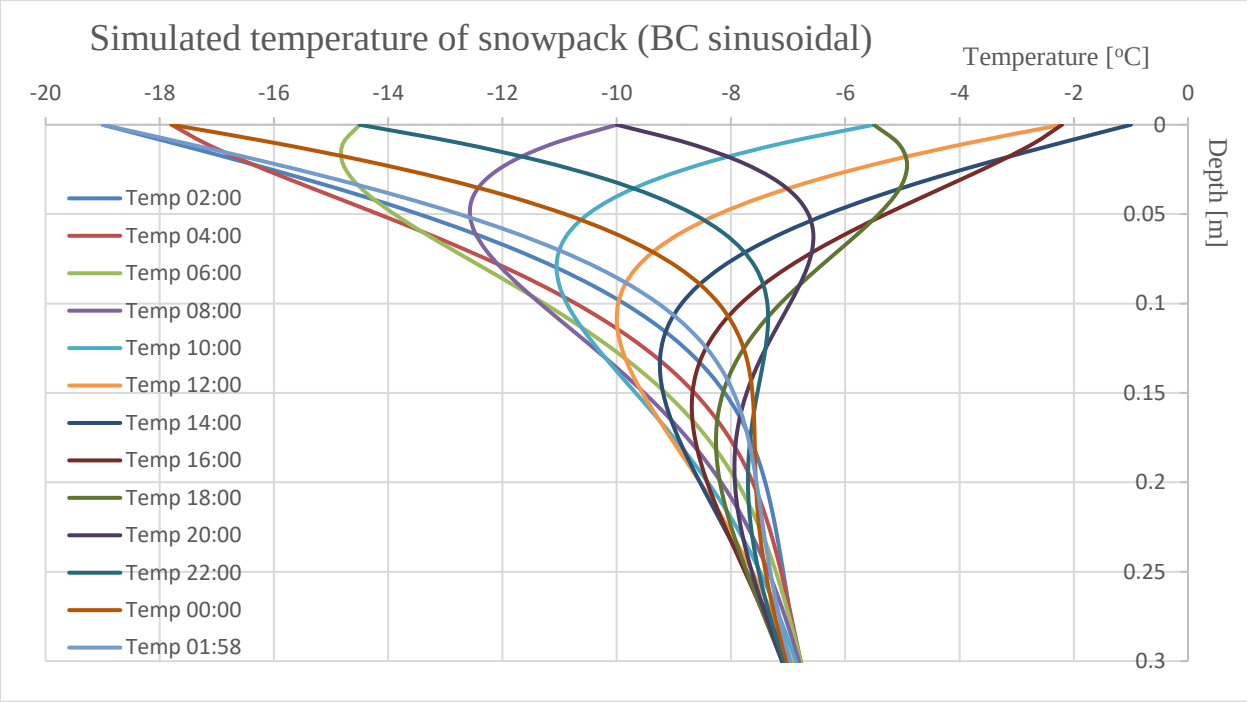

Figure 19 Temperature profiles at two-hour intervals throughout 24 hours in the snowpack simulated with sinusoidally oscillating surface temperatures. The near symmetry makes for an aesthetically pleasing spread of temperatures.

The simulation of the Pinzer and Schneebeli (2009) experiment and this simulation are quite similar in their sinusoidal nature. The top half of the Pinzer and Schneebeli (2009) experiment acts as a simulation with fixed, constant lower boundary condition and sinusoidal upper boundary condition. The mean temperature does not change with depth, while the simulation done here has a warmer mean temperature with depth.

The resulting sum of facet growth with depth after one day of sinusoidal temperature oscillations can be seen in Figure 20. Under 22 cm the sum of facet growth is zero. From 22 cm to 12 cm there is increasing negative facet growth with decreasing depth, until 12 cm with a peak value of -0,018 mm of growth. From 13 cm to about 5 cm negative facet growth decreases with decreasing depth. From about 5 cm to the simulated snow surface there is positive growth of facets, nearly linearly increasing with decreasing depth. The peak value on the positive side is 0,022 mm of growth at the surface.

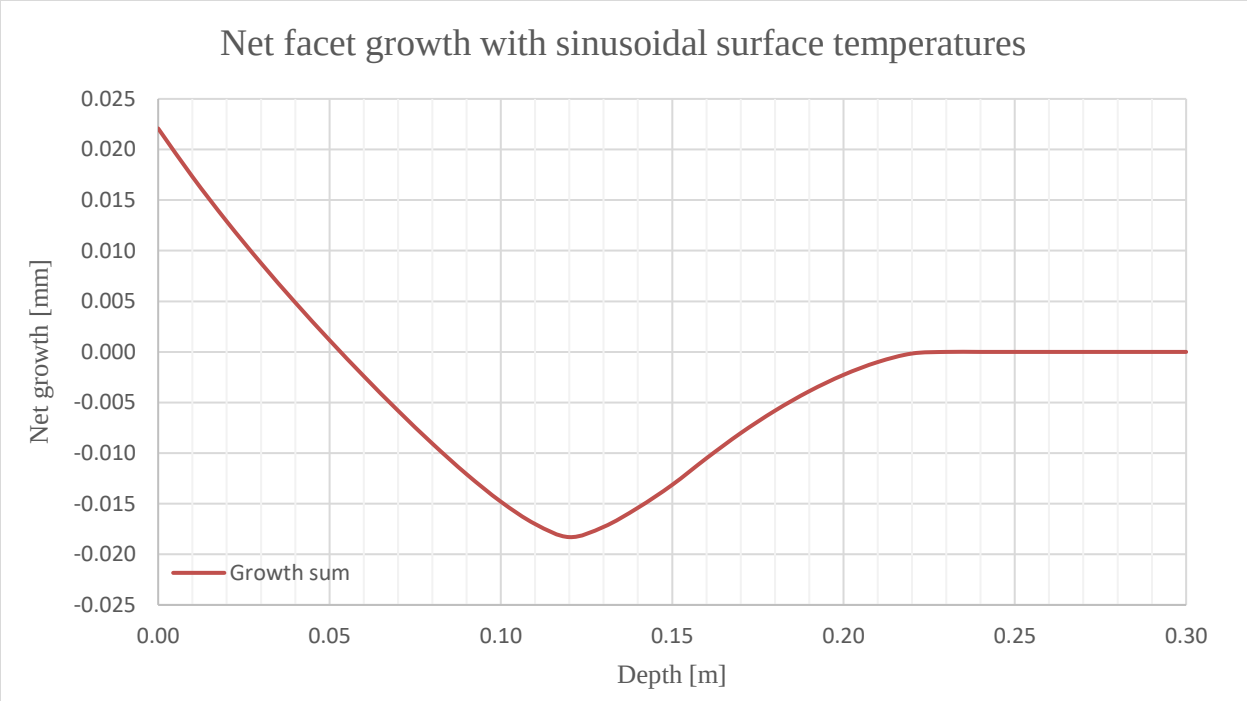

Figure 20 Net facet growth with depth after one day of sinusoidally oscillating surface temperatures. Positive growth means faceting on the top of grains, while negative means faceting on the underside of grains.

The lack of net growth under 22 cm in Figure 20 suggests that the temperature gradients under that depth at those temperatures are not large enough to produce a vapor pressure gradient above 5 mb/m and no facets grow as a result. In the section between 22 cm and 12 cm, negative faceting increases to a peak. This indicates that in this part of the snowpack, negative temperature gradients are large enough to produce negative vapor pressure gradients above 5 mb/m. From 12 cm and upward, the temperature gradients are still, on average, negative, as seen in Figure. The difference between maximum and minimum temperatures starts becoming pronounced at that depth. This implies that the effect of temperature becomes more important at that depth, giving the positive temperature gradients noticeably higher vapor pressure gradients than the negative temperature gradients. Above 5 cm depth is where the effect of temperature starts to dominate. A net growth of zero does not necessarily mean growth has not occurred, only that positive and negative growth are equal. Here, the differences between warmest and coldest temperatures are relatively large, and the effect of temperature becomes more important than the overall mean negative temperature gradient.

Facet growth rate for three depths over time is shown in Figure 21. The peak values for both positive and negative growth rates occur later with depth. The absolute values of positive and negative peaks for all depths decrease with depth. As seen in Figure 20, net growth rate at the surface is positive, at about 5 cm

depth 0 nm/s, and at 12 cm, negative. Though it is not shown in Figure 21 to avoid crowding the graph, growth rate at 23 cm is 0 nm/s. The flat parts where growth rate is zero is where the simulated snowpack has experienced vapor pressure gradients below 5 mb/m and no facet growth takes place. The length of sections with 0 nm/s growth rates increase with depth until 22 cm depth. Under this value growth rates are 0 nm/s through the whole simulation.

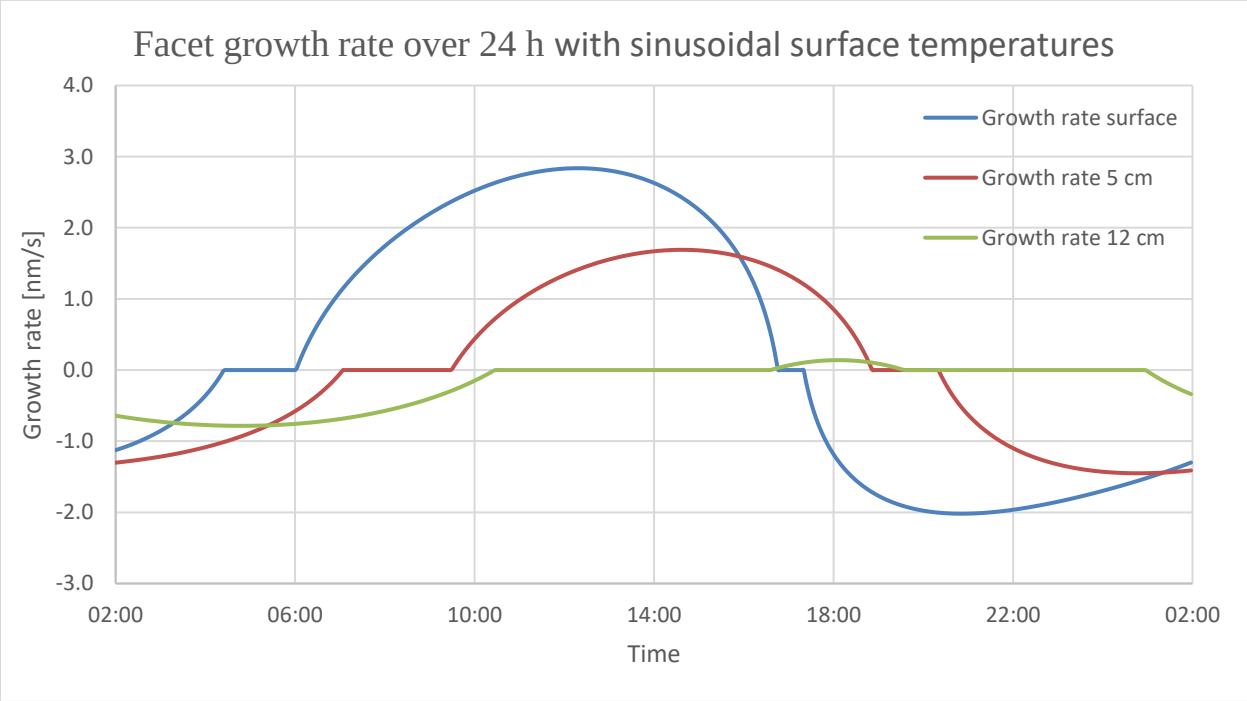

Figure 21 Facet growth rate over time at three depths for the snowpack with sinusoidal surface temperatures. The blue line shows growth rate at the surface, where the highest amount of positive net facet growth was found. The red line shows growth rate at 5 cm depth, where positive and negative growth cancelled each other to become zero net growth. The green line shows growth rate at 12 cm depth, where the highest amount of negative net facet growth was found.

The staggering of peak growth rates by depth is expected, as it takes time for changes in surface temperature to propagate downward. The lines for surface growth rate and growth rate at 5 cm show a gradual increase when going toward positive values, and a more rapid decrease when going toward negative values. This is likely due to the effect of temperature. When the snowpack is warmest, around 14:00 for the surface and 16:00 for cm depth (Figure 19), a change in temperature gradient leads to a larger change in vapor pressure gradient than when the snow is colder. Though it is difficult to see only by looking at the graphs, and no calculations have been made to specifically test it, it can be assumed that

the line for growth rate at 12 cm depth in

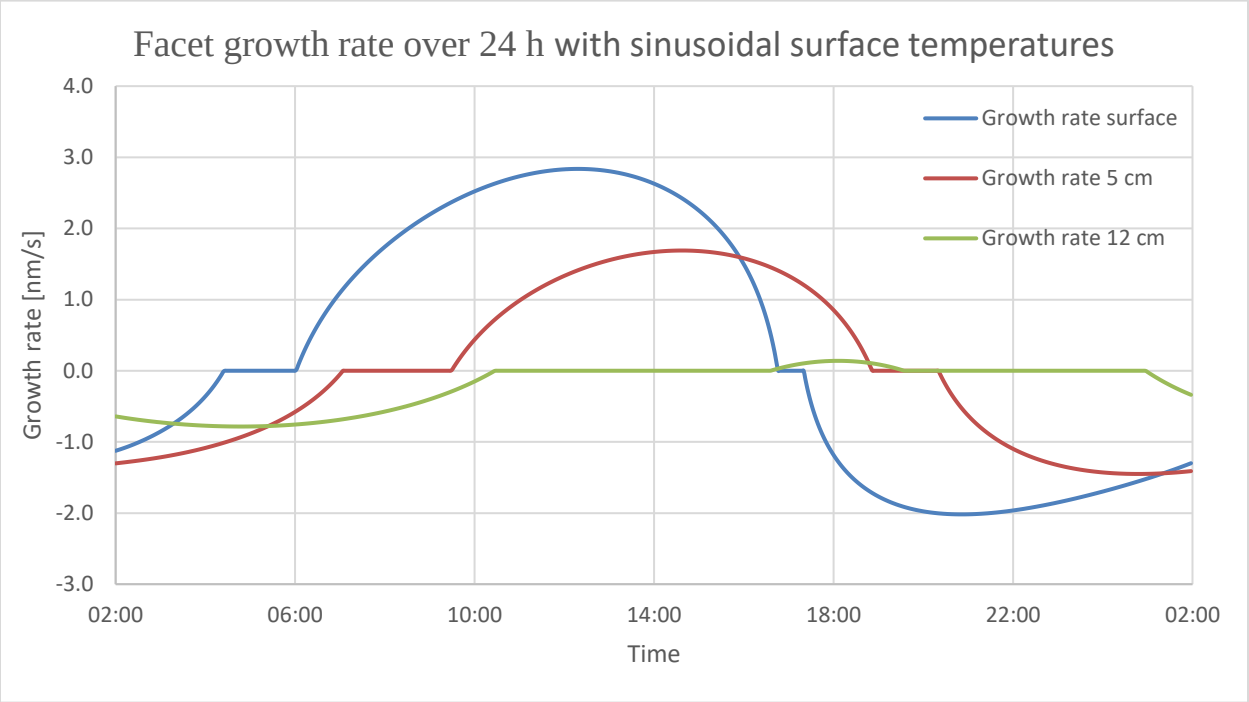

Figure 21 and the lines in Figure 18 for growth rate in the Pinzer and Schneebeli (2009) experiment are skewed in a similar fashion.

As seen in Figure 20, on either side of the 12 cm mark there are depths that have the same net growth after a day. This implies that the sum of areas between their respective growth rate graphs and 0 nm/s growth rate are the same, even though the shapes of those graphs are different. Between 12 cm and 23 cm, there is little to no positive growth, because the spread in maximum and minimum temperatures is not large enough to produce large positive temperature gradients, or to overcome the mean negative temperature gradient. There is only a little negative growth in the same depth interval, because although the mean temperature gradient is negative, it is not very large. Between 12 cm and 5 cm, there is substantially more positive and negative growth, but the net growth can still be the same as points below 12 cm since growth rates with opposing signs cancel each other. Rate of rounding may have an effect on these results, but is not investigated in this thesis.

4.2. Results field period

The weather during the field period from 00:00 on the 11th of March until 14:00 on the 12th of March consisted of consisted of two cold and clear nights with air temperatures down to -2.5°C followed by sunny and warm days with air temperature reaching 4°C, measured by Tinytag B placed 150 cm above

the snow surface (Figure 14). No faceted crystals were observed during the field period.

4.2.1. Radiometer data field days

Due to loss of battery power in the Logbox, all data before about 19:00 on the first field day was lost. In Figure 22, showing shortwave radiation measured by the pyranometers, the incoming SW radiation is zero during the night when the sun is under the horizon. At about 07:10 the sun rises and both incoming and outgoing SW radiation increase rapidly up to their peaks between 12:00 and 13:00. At their peaks SW_{in} nearly reached 500 W/m^2 and SW_{out} reached slightly more than 400 W/m^2. SW_{in} and SW_{out} decrease smoothly from their peaks until around 14:00, when the clear period was over and clouds arrived, affecting the measurements drastically. Interestingly, both incoming and outgoing SW radiation increase at approximately the same rate until 08:30. This gives an albedo of about 1 and net SW of about 0 W/m^2 until the lines for incoming and outgoing SW radiation diverge at 08:30. From there the albedo gradually decreases from 1 to 0,75 at 14:00. The effect of decreasing albedo can be seen in the line for net SW as well. Since a continuously larger portion of SW_{in} is not reflected, net SW rises nearly linearly and does not peak and decrease like SW_{in} and SW_{out} do separately.

The two spikes at 11:40 and 13:10 are due to human disturbance when checking whether the Logbox was still running. This can be seen in Figure 23 only on the lines for outgoing SW and outgoing LW radiation, meaning the disturbance was only between the radiometer and the ground. One explanation of the decrease in albedo may be that increased moisture on the snow surface lowers albedo. A second, and perhaps more important factor is that different wavelengths of SW radiation have different albedos at high solar zenith angles.

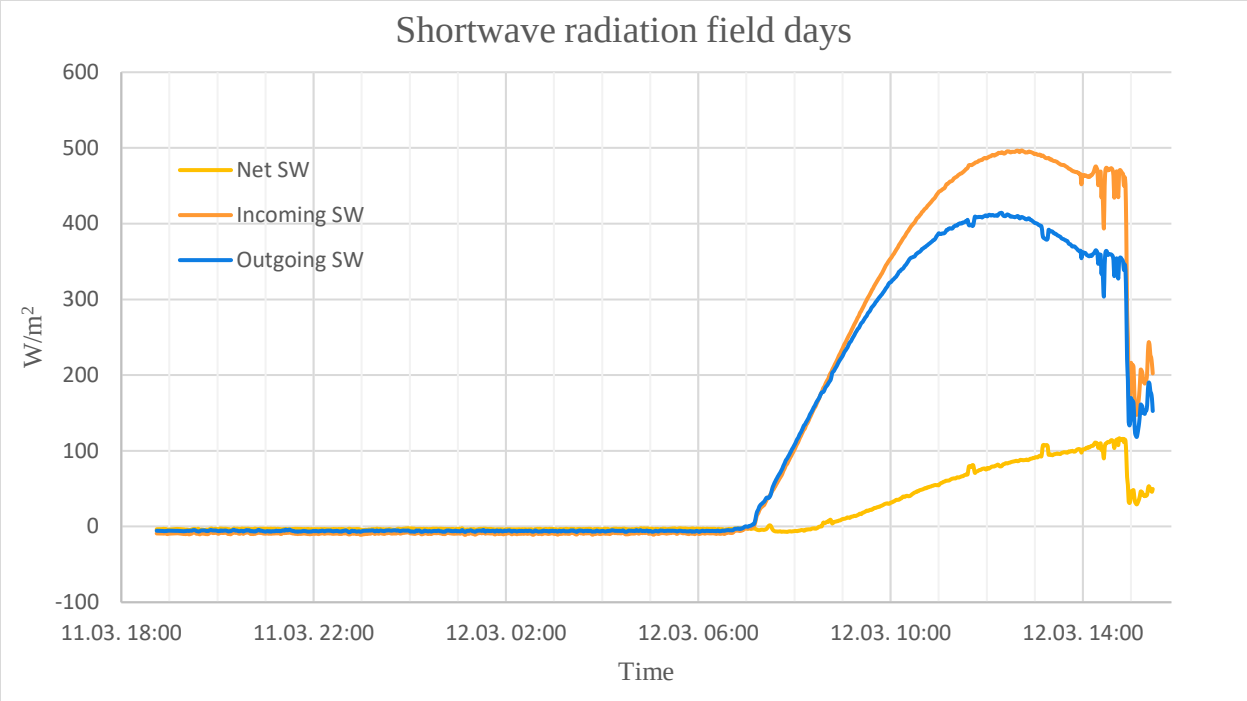

Figure 22 Shortwave radiation field days.

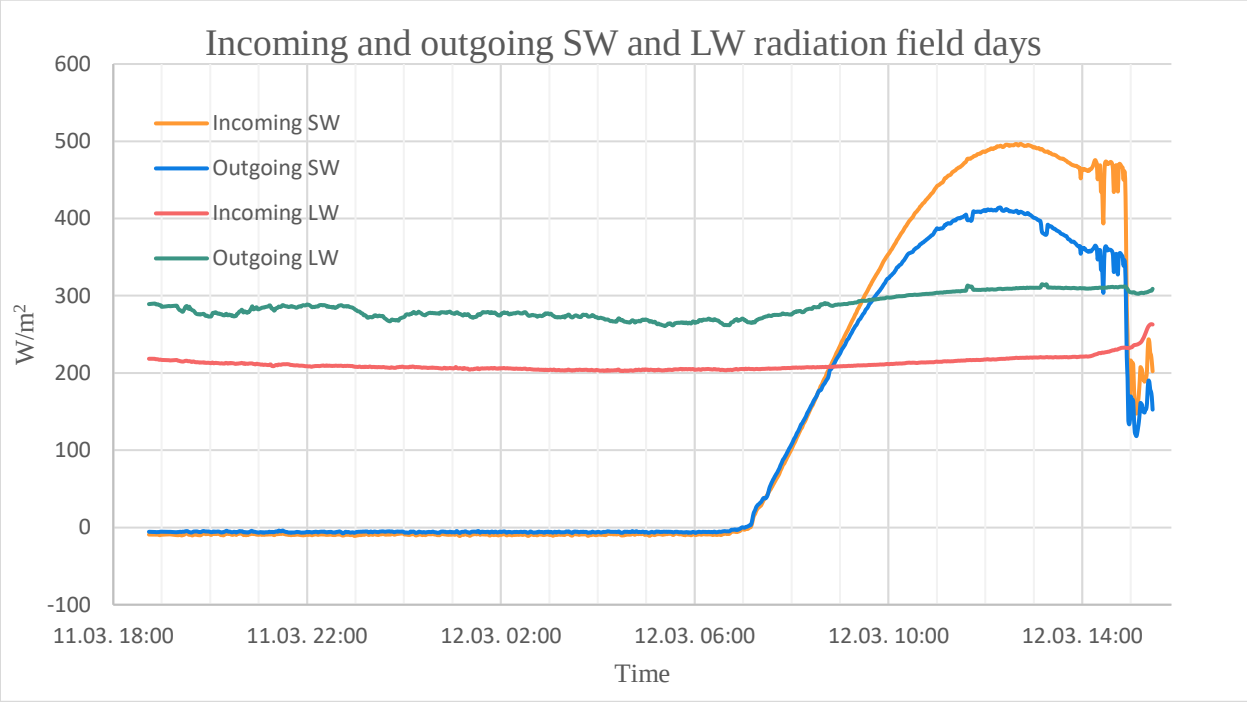

Figure 23 Incoming and outgoing SW and LW radiation field days.

4.2.2. Tinytag data field days

Figure 24 shows the snow and air temperatures measured by the Tinytag temperature loggers during the field period. The air temperature was measured 10 cm (logger C) and 150 cm (logger B) above the snow surface. Logger C shows bigger temperature fluctuations and varies from -6°C to +6°C (±12°C) on the 11th of March. Logger B follows the same oscillating pattern, but with less variation (±6°C). The biggest temperature difference in the air is on 11th of March at approximately 03:50 and 07:50 with nearly a 4°C temperature difference.

Snow temperature was measured at 30 cm (A), 100 cm (D) and 150 cm (E) from the snow surface. The temperature 30 cm down in the snowpack lies around -2°C from midnight the 11th of March until the following midnight before cooling down to -4°C 12:00 on the 12th of March. The snow temperature 100 cm below the snow surface is around -1.7°C in the beginning of the field period, before it gradually warms up to -1.4°C at the end of the field period. The measured temperatures at the base of the snowpack are steady -0.2°C throughout the whole field period.

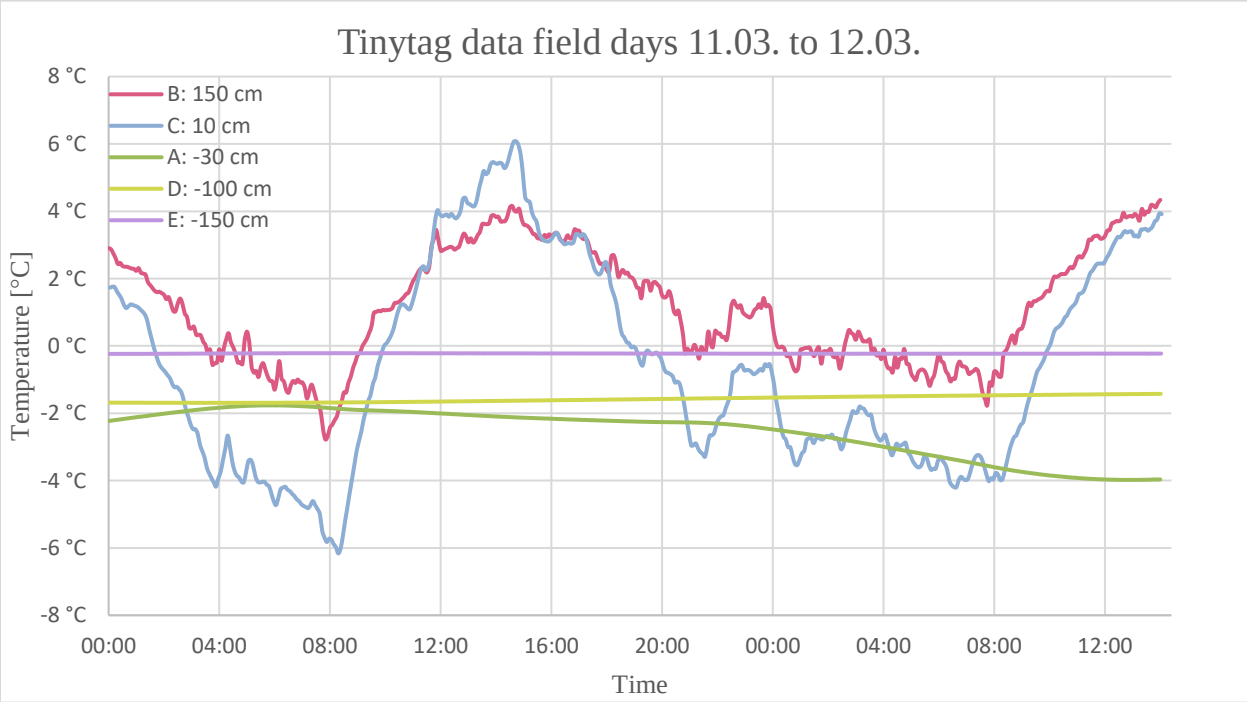

Figure 24 Tinytag data from field days 11th to the 12th of March. The measuring distance is relative to the snow surface.

The differences between air temperatures suggest that logger C is affected by the snow surface temperature more than logger B. During the night, Tinytag C shows colder temperatures than B, which is likely due to LW cooling of the snow surface. What looks like scatter in Tinytags B and C, may be the effect of wind, bringing changes in temperature due to sensible heat.

The snow temperature increases with depth, while the variation in the measurements decreases This implies that there are warmer and more stable temperatures towards the base of the snowpack providing an upwards heat flux, and that the diurnal temperature fluctuations do not significantly affect the snow below 30 cm depth. This confirms what McClung and Schaerer (2006), Birkeland (1998) and others say about diurnal temperatures in the snowpack.

4.2.3. Results of manual temperature measurements

When measuring snowpack temperatures, three measuring methods were employed in the daytime: measuring in the sun, measuring directly after shading the surface, and measuring 20-30 min after shading the surface. The main issue with using the temperature measurements from the sun is knowing what were truly measured. Since most SW radiation is not absorbed directly at the snow surface, but penetrates deeper, the near surface temperature measurements taken in the sun were erroneously high. Using the shaded measurements can prevent this effect. The measurements taken 20-30 min after shading are also not so representative, because the sun influences the temperature of the snowpack. The temperatures after 20-30 min of shading are missing SW radiation and are too cold. The measurements taken directly after shading, on the other hand, avoid SW radiation being absorbed by the metal in the thermometers, but are taken quickly enough that quite little heat is lost from the snowpack. These are the values chosen to be presented and used to compare with the model. The measurements taken with the handheld IR thermometer is discarded due to measurement error.

4.2.4. Shortwave extinction

Figure 25 shows the measured shortwave extinction expressed as a function I(x), introduced in section 2.2.1, as percentage of radiation remaining by depth. The function for the shortwave extinction during the field day is:

$$I(x) = 1e^{-16x} \tag{47}$$

With the measured extinction coefficient, K=16, 20% of the penetrating solar radiation remains after 10 cm. Using Fierz et al. (2008)'s value, where $K = 230$, 10% of the absorbed SW radiation remains after only 1 cm. Application of the extinction function in the model is quite important to the results and is discussed in section 4.3.2.

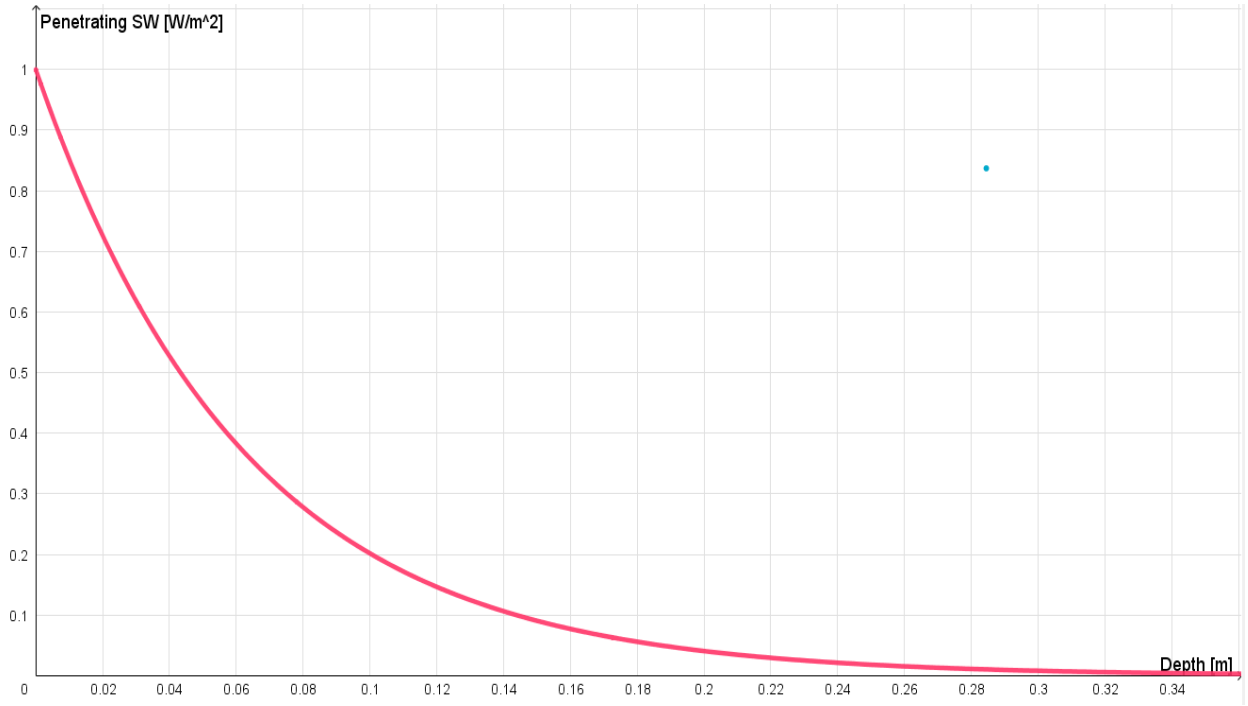

Figure 25 Measured shortwave extinction 12th of March. $I(x)=1e^{-16x}$

4.2.5. Density results

The density calculations from the 11th of March are presented in Table 4. The measurements show an increase in density with depth from 231 kg/m^3 to 330 kg/m^3 and an average density of 277 kg/m^3.

In the final versions of the simulations of the field period and the 1st of April period, the measured average density of 277 kg/m^3 was used for the whole snowpack even though the measured upper 39 cm were less dense. This value is below the upper limit of 350 kg/m^3 presented by Marbouty (1980), where depth hoar does not grow because of too little pore space. Changing the density and effective conductivity with depth is a simple step in further development of the model that is not done in this project.

Table 4 Density measurements from the field area taken 11th of March.

Depth interval [cm]		Measured mass [kg]	Snow mass [kg]	Density [kg/m^3]
4	15	0,558	0,509	231,36
16	27	0,57	0,521	236,82
28	39	0,608	0,559	254,09
42	53	0,684	0,635	288,64

55	66	0,721	0,672	305,45
69	80	0,696	0,647	294,09
82	93	0,774	0,725	329,55
Average density				277,14

4.3. Simulation of field days

Table 5 shows the variables used for simulation of the field day. Numbers in parentheses represent values used for the heat flux model which differed from the fixed boundary condition (BC) model.

Table 5 Variables used to for field days simulations. Numbers in parentheses show differing values used for the heat flux model.

Variables		**Units**	**Values**
Thermal diffusivity	α	[m^2/s]	3,45 *10^{-7}
Heat capacity	c	[J/K]	2090
Density	ρ_s	[kg/m^3]	277
Effective thermal conductivity	k_{eff}	[W/m*K]	0,2
Delta x	Δx	[m]	0,1 (0,05)
Delta t	Δt	[s]	60 (30)
Total Depth	x_{max}	[m]	0,9 (0,5)
Duration	t_{max}	hours	38 (18)

4.3.1. Modeling snow temperatures using fixed boundary conditions

Surface BC based on manual temperature measurements

The first simulation has a fixed BC controlled by the manual temperature measurement taken 1 cm from the snow surface. The initial conditions are the temperatures measured at 00:00 the 11th of March, with temperatures linearly interpolated between the thermometers. Figure 26 shows cooling of the snowpack at 22:00 and 06:00. The model follows the measured temperatures quite well when forced at the surface by 1 cm measurements. This indicates that the effective conductivity of 0.2 is representative of this snowpack

and that the modeled snowpack conducts heat out quite similarly to the actual snow during the fieldwork.

Figure 27 shows the heating of the snowpack. The simulated temperatures tend to lag the measured ones. This could be caused by the fixed boundary condition which does not consider the shortwave radiation distribution below the surface.

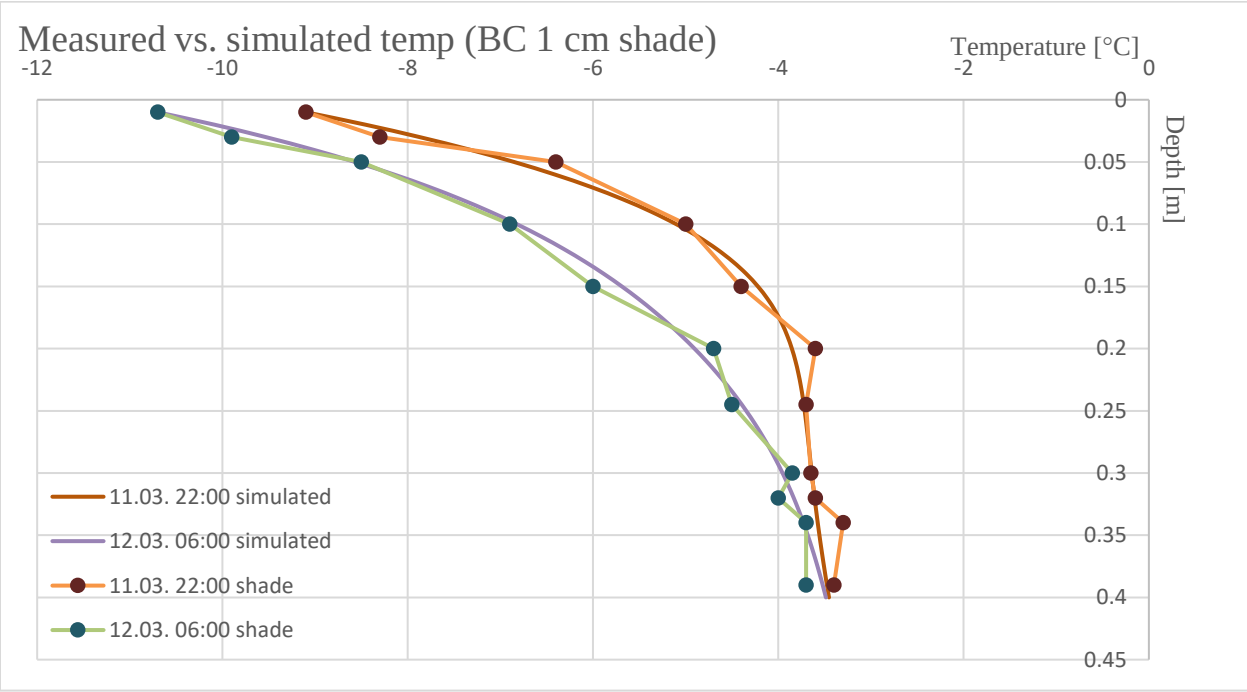

Figure 26 Measured vs simulated temperatures of the cooling snowpack. The surface BC of the simulation is the manual temperature measurements at 1 cm depth.

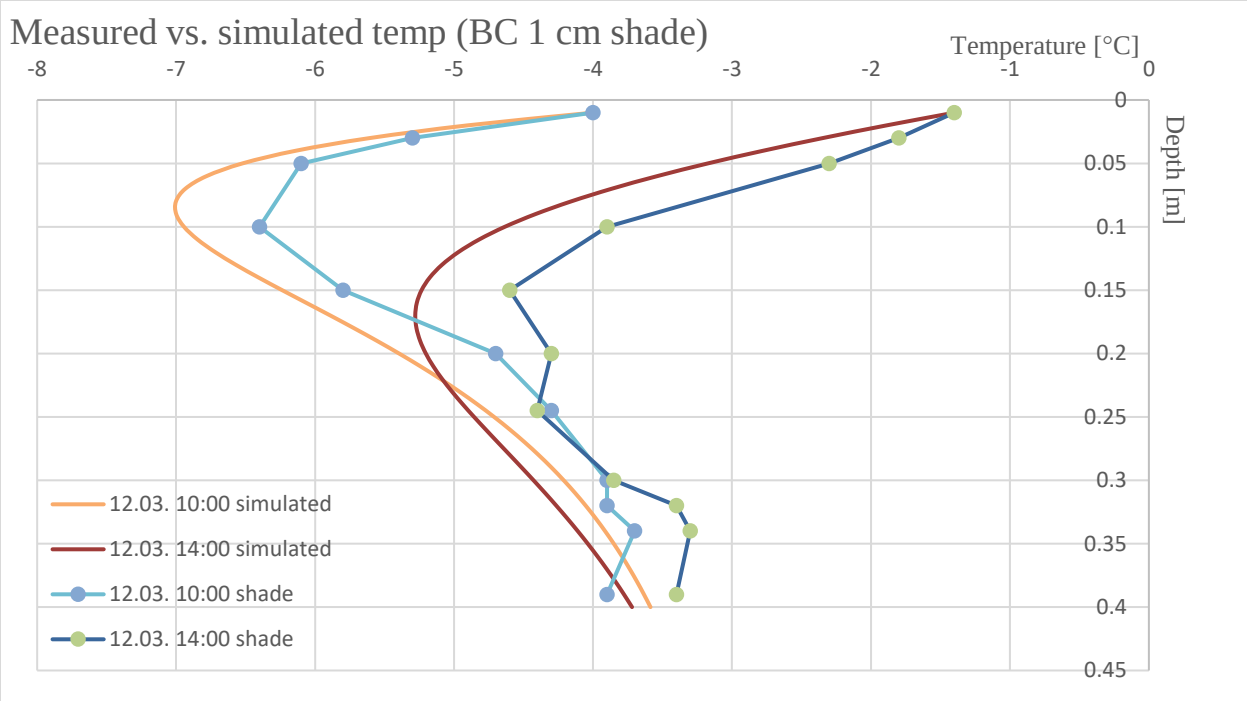

Figure 27 Measured vs. simulated temperatures of a heating snowpack. The surface BC of the simulation is the manual temperature measurements at 1 cm depth.

Surface BC based on surface temperatures calculated from radiometer

The second simulation of snowpack temperatures during the field days was performed using a fixed surface BC based on the snow surface temperatures calculated from the outgoing longwave radiation measured with the radiometer using equation (44). The surface temperatures measured from the radiometer tended to be a degree or two colder than the temperatures measured at 1 cm depth. Figure 28 shows simulated temperatures compared with the manual measurements at 06:00 and 12:00 the 12th of March. When the snow is cooling, the simulated temperatures replicate the measured temperatures quite well. The biggest deviation for the 06:00 profile is at 15 centimeters depth with a temperature difference of 0,5°C. During day warming the simulated temperatures do not keep up with the measured snow temperatures, showing approximately 1°C deviation at 14:00 through the profile from five centimeter to 35 cm.

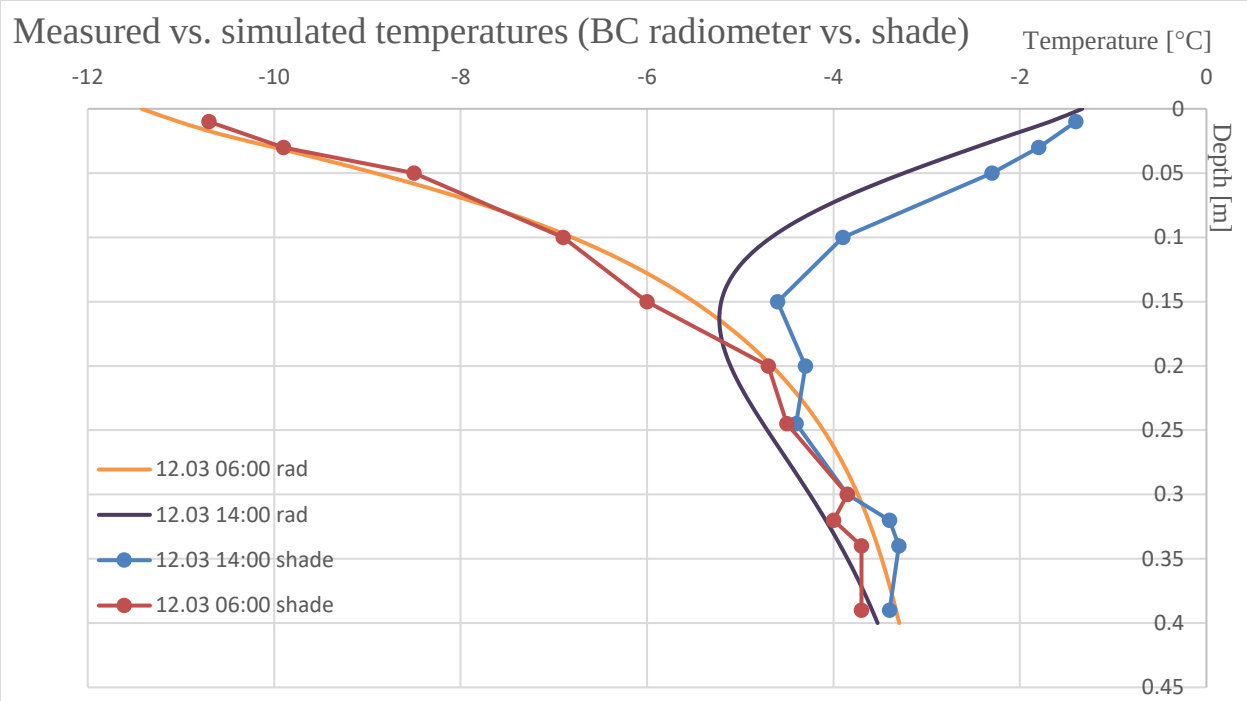

Figure 28 Measured vs. simulated temperatures during heating and cooling of the snowpack. BC is fixed by the snow surface tempratures calculated from outgoing longwave radiation.

4.3.2. Development of the heat flux model based on field day temperature measurements

The manual field day temperature measurements of the snowpack were important in order to tune the heat flux model. As presented in chapter 3.1.3., outgoing longwave radiation is used as a control variable to evaluate model performance, and is crucial for the three main decisions which were made about model input data: (1) Choosing a fixed albedo for net shortwave radiation, (2) Implementing a self-regulating sensible heat variable and (3) choosing a shortwave extinction coefficient.

Investigation of net shortwave radiation with fixed and varying albedo

The net shortwave measurement presented in 4.2.1 implies a changing albedo value during the day. When measured net shortwave was used as an input for the model, the simulated near-surface temperatures ran too cold during the morning period from sunrise at 07:00 to 09:00. The low temperatures suggested a lack of solar heat distributed at depth during this time. To mitigate this, an average albedo of 0,878 was calculated based on the integrated function of SW_{net} and SW_{in} by using equation (4), then applied the obtained albedo to the measured incoming shortwave radiation. The two solar inputs are shown in Figure 29.

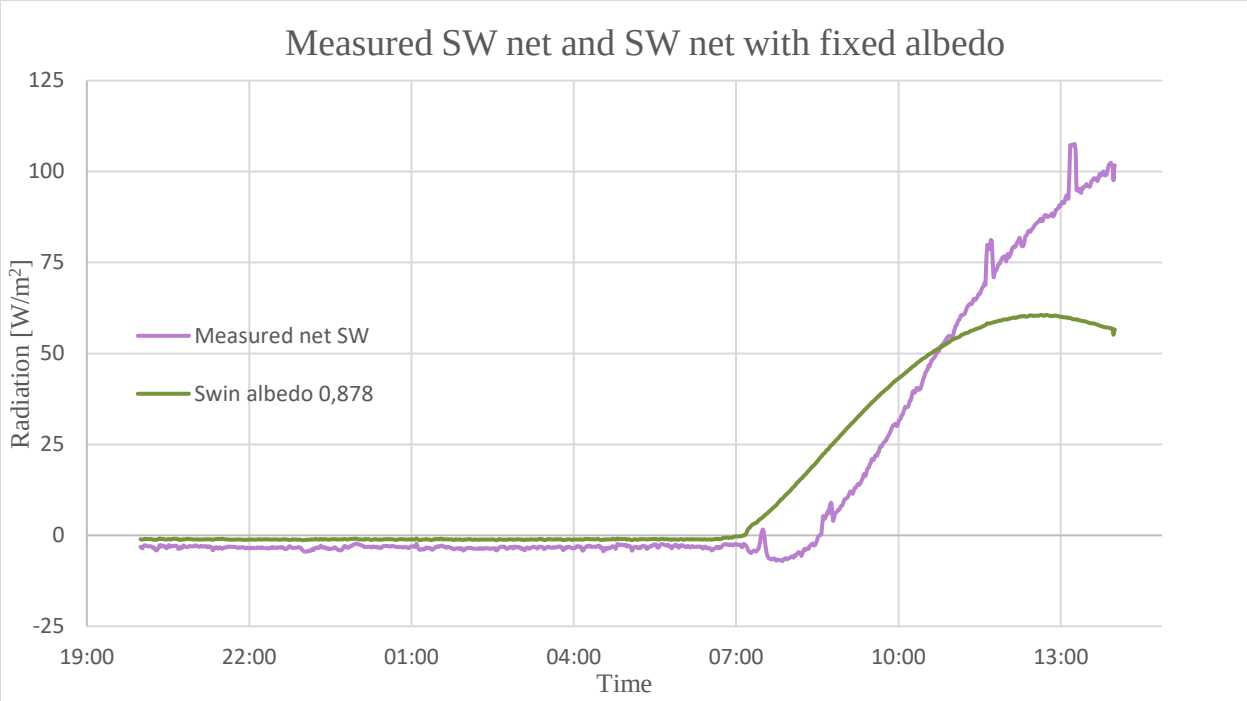

Figure 29 Different values for net shortwave radiation, the purple graph is the measured net shortwave radiation, and the green graph is calculated from incoming shortwave with a fixed albedo 0,878. Both graphs have the same integrated area.

The measured SW_{net} (purple) input provides less heat to the surface between 07:00 and 10:40 than SW_{in} with a fixed albedo (green). From 10:40 until end of measurements, the measured SW_{net} provides more heat and peaks at 14:00 with a difference of 45 W /m^2. The graphs have the same integrated area, resulting in equal supply of heat during the period, but with different distribution. The field observation supports the use of a SW_{in} radiation curve with a fixed albedo, which are as input for all heat flux simulations presented in this thesis. Why the observed snow heating seems incompatible with the measured net shortwave radiation is unclear. Further investigation is needed.

Investigation of the sensible heat input parameter

To investigate the sensible heat parameter, the field day period was simulated three times with three different sensible heat inputs for the surface boundary condition. First with a constant sensible heat value, then with a sensible heat input calculated with a constant windspeed value, and lastly, a varying windspeed value.

Figure 30 shows the computed LW_{out} radiation based on the modeled surface temperature with a constant sensible heat input value. The yellow line is the outgoing longwave radiation measured in the field. A constant sensible heat value of 58,4 W/m^2 was used. The figure shows that the computed surface temperatures is too warm during the night and too cold during the day.

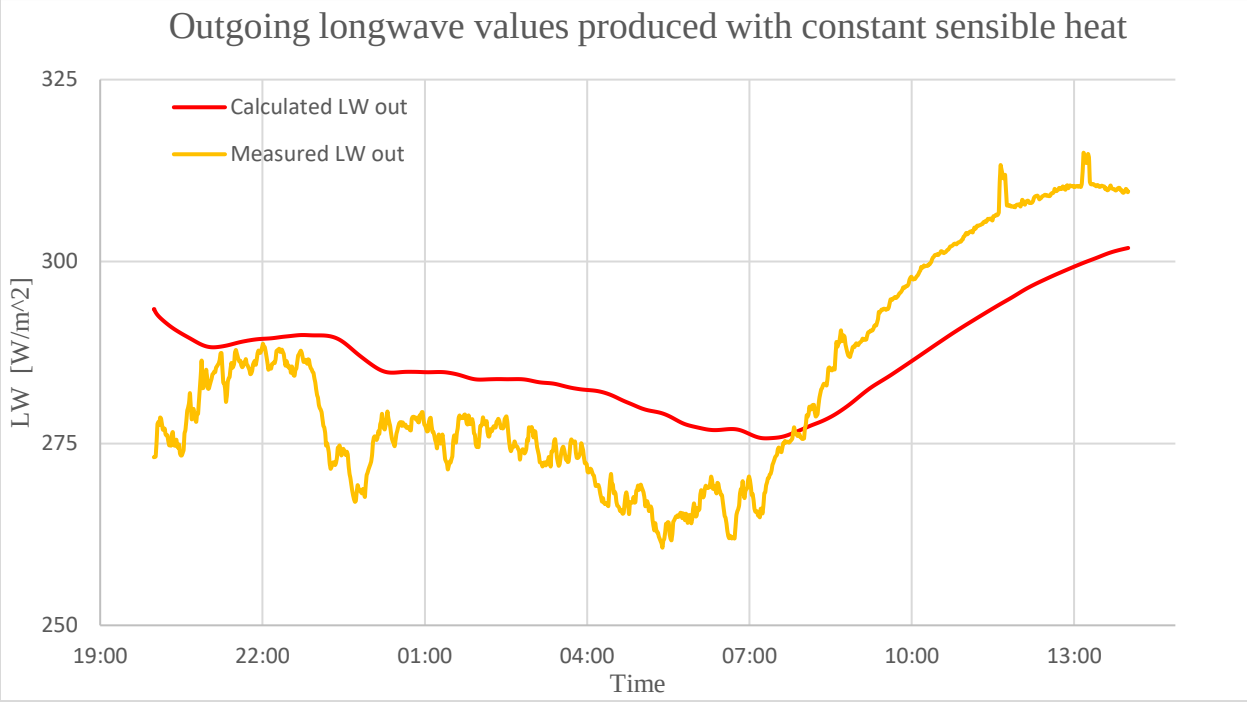

Figure 30 Measured outgoing LW radiation compared with calculated outgoing LW values with a constant sensible heat input of 58,4 W/m^2.

The constant sensible heat value of 58,4 W/m^2 was calculated from equation (2), the energy balance equation. The given value is the result of an average net zero heat flux for the measured period. The assumption of a net zero heat flux is probably wrong since the simulated period does not span the length of a full day (18 hours) and the average snow temperature could be drifting. In lack of accurate sensible heat measurement, the net zero heat flux value is considered a reasonable starting point. Argued that the snow is neither melting nor cooling at an obvious rate.

Figure 31 Figure 31Figure 31 shows calculated outgoing longwave with the sensible heat input calculated by a fixed windspeed value of 5,357 m/s. This value results in an average sensible heat flux of 58,4 W/m^2.

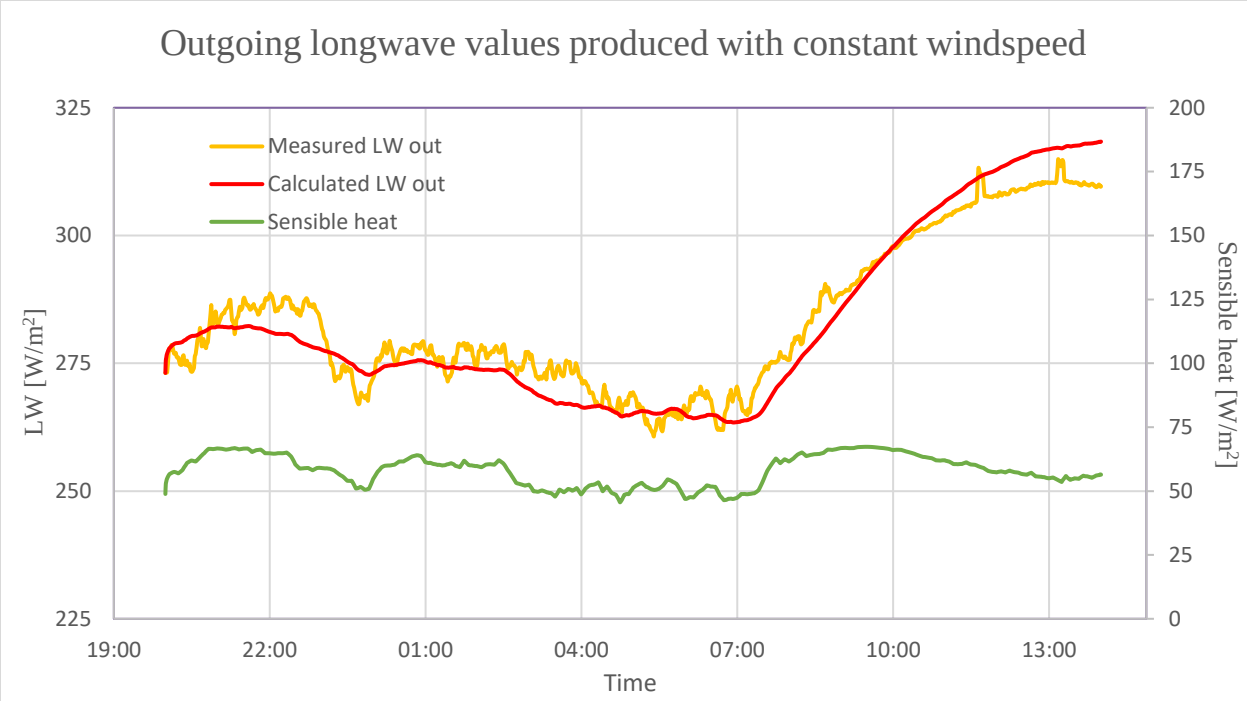

Figure 31 Measured outgoing LW radiation compared to calculated LW out based on modeled surface temperature. Sensible heat input is calculated based on a constantt windspeed of 5,357 m/s, which result in an average sensible heat flux of 58,4 W/m²

With a constant windspeed, the sensible input varies based on the temperature gradient between the snow surface and the air temperature measured at a height of 150 cm. Where a bigger gradient would increase the heat flux. The constant windspeed gives more realistic surface temperatures than the constant sensible heat input, despite the average flux is the same value within one decimal point. Still, the modeled surface temperatures run to cold during the night and too hot after 10:00.

Figure 32 shows the calculated outgoing longwave radiation with the sensible heat input calculated by a variable windspeed parameter. The average windspeed value for the whole period is 5,2 m/s and the average sensible heat flux is 58,3 W/m^2.

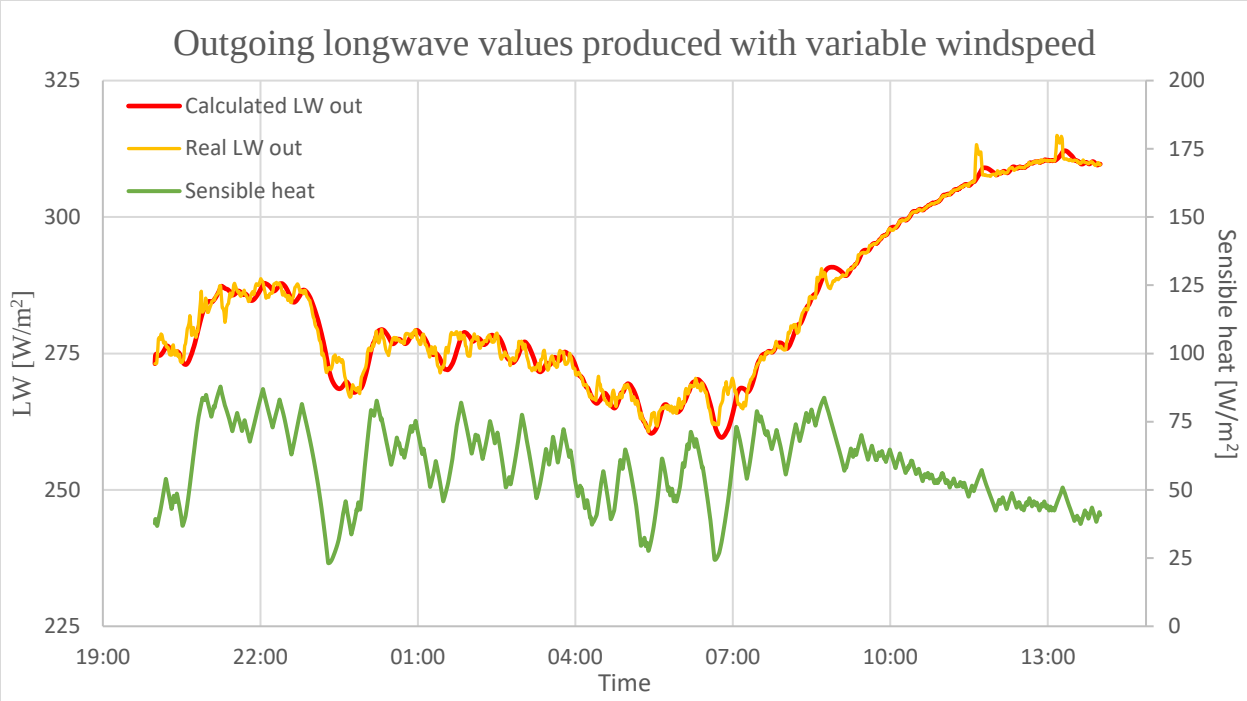

Figure 32 Measured outgoing LW radiation compared to calculated LW out based on modeled surface temperature. Sensible heat input is used to match the LW radiation based on a variable windspeed parameter. The calculated average windspeed for this period is 5,2 m/s and the average sensible heat flux is 58,3 W/m^2.

The variable windspeed parameter gives the best fitting surface temperatures for the field day period. The calculated LW_{out} values lags the real measurements, as the variable windspeed is constantly adjusting for the best fit. By running the model with a fitting sensible heat parameter adjusted by a variable windspeed, the model is essentially driven by net shortwave radiation and surface temperatures calculated from outgoing longwave radiation. By adjusting sensible heat, the model could potentially make any solar input work, which is a fundamental flaw. Laten heat fluxes is also neglected as a model input, due to lack of necessary equipment to measure the relevant metrological conditions (see 2.2.4). Further investigation is needed where the turbulent fluxes of both sensible and latent heat is properly measured in the field. A similar setup as used by Stössel et al. (2010) would improve the project.

However, calculating sensible heat with a bulk movement equation which encompasses measured temperature gradient as input, the resulting average windspeed of 5,2 m/s shows that the model is performing in a realistic manner. For high pressure weather systems, an average windspeed of 5,2 m/s is probably too high, but not completely unrealistic.

Investigation of the solar extinction coefficient

Figure 33 shows measured and simulated temperatures in the snowpack on the 12th of march at 12:00 with two different extinction coefficients, 16 and 230. With an extinction coefficient of 16, the top 20 cm is more than 2°C hotter than the measured temperature. Using the extinction coefficient of 230, the simulated near-surface temperatures are closer to the measured, but below 5 cm depth they gradually become colder than the measured temperatures.

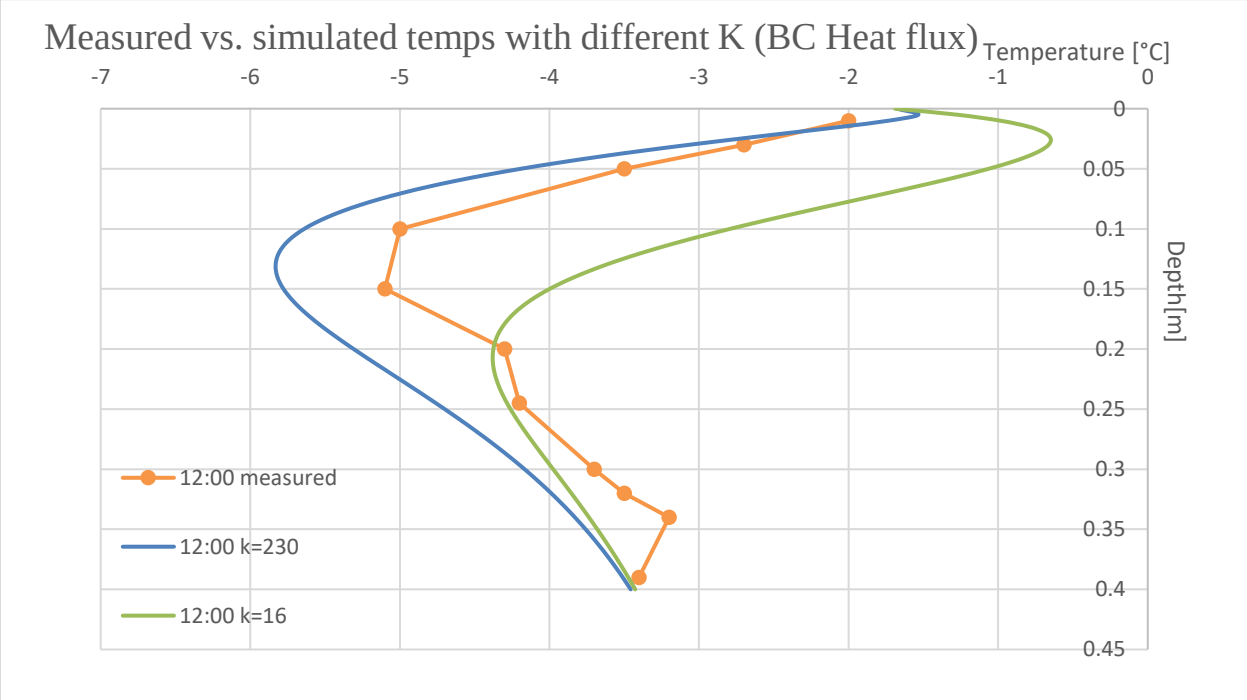

Figure 33 Measured vs simulated temperatures using a different extinction coefficient (K). 12.03. 12:00.

When K is big, solar radiation is distributed closer to the surface of the snowpack. This lets the heat conduct to the surface quicker where increased surface temperatures lead to stronger LW cooling, resulting in a colder snowpack at depth. One of the limitations of using a constant K is that you need a lower K value to get heat deep enough into the snowpack to match the manual temperature measurements. Decreasing the K causes the warmest point of the near-surface snow to be located at deeper depths. With a K value of 16, the warmest snow temperature is located three centimeters below the surface.

During the manual temperature measurements, this negative temperature gradient by the surface was not observed. The warmest point observed was at 1 cm depth when the snowpack was heating. This means that the negative temperature gradient potentially found by the surface in a snowpack heated by the sun, the "greenhouse effect" (Brandt & Warren, 1993), is found above or around the 1 cm mark. The value

used by Fierz et al. (2008) of $K = 230$ leaves the temperatures at depth slightly too cold, but pushes the negative gradient of the greenhouse effect to the top centimeter. Since the near-surface conditions are quite important to this thesis, K=230 is used. Further development of this model, beyond the scope of this thesis, should include an extinction coefficient that takes into account separate wavelengths of solar radiation.

Snow temperatures simulated with the heat flux model

Finally, the modeled temperature result of the field day period from 20:00 11th of March to 14:00 12th of March is shown in **Error! Reference source not found.**. The model uses the temperature profile measured at 20:00 as initial condition, assuming linear change between the measured point. The simulated temperature profile produced by the heat flux model shows a good data fit during the night but is off by 0,5°C at 15 cm depth 12:00. This is approximately the same as the model using BC radiometer (Figure 28), but the heat flux model generates better fitting temperatures in the top five centimeters, which is important for the investigation of near-surface temperatures.

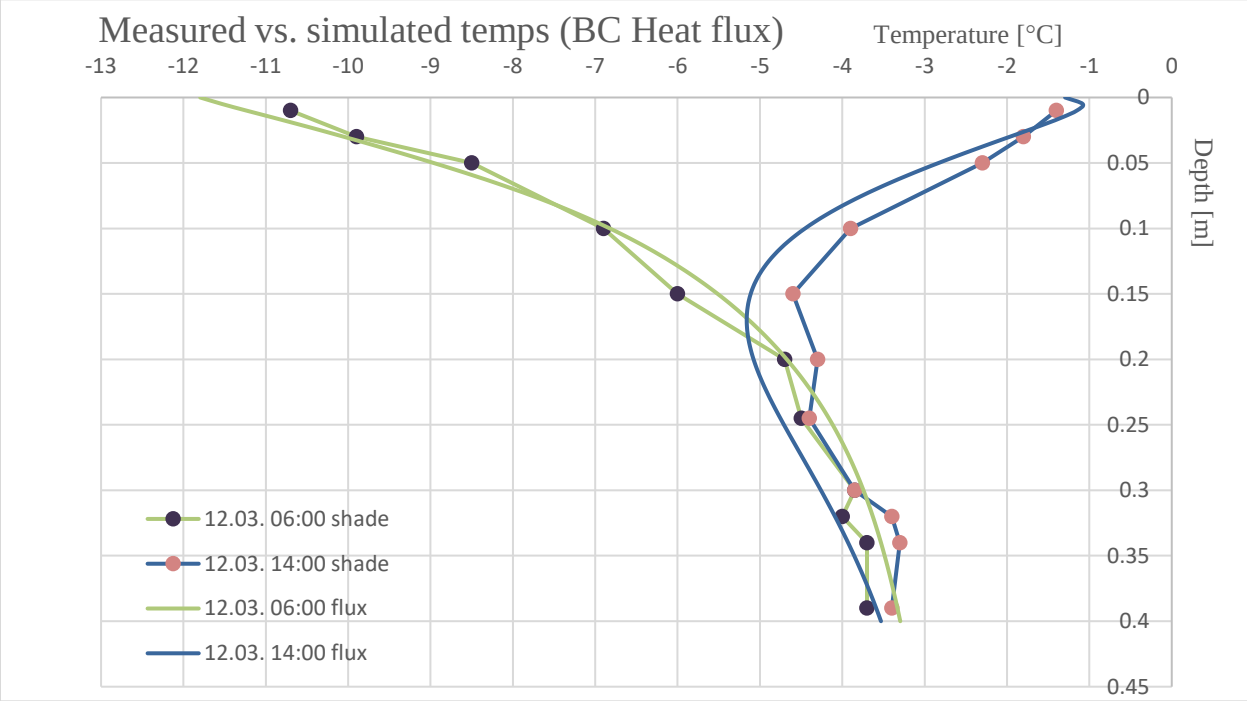

Figure Measured vs. simulated temperatures using BC heat flux.

The heat flux model is run with a spatial resolution of five millimeters. This value was chosen as a compromise between sufficient resolution and practicality. The size of the Excel solution matrix becomes very large at high resolutions, requiring a lot of computing power. To improve the model, the solution could be coded in a more suited program. However, a spatial resolution of less than a millimeter seems problematic as it becomes less than the size of a snow crystals. As discussed in 2.3.1, the smallest vapor pressure gradients of interest occur across pore space between individual grains. Since the model assumes the snow as a continuous medium, using a resolution much less than a millimeter could produce unrealistic results. Lastly, the model assumes a perfectly flat surface, considered a fair assumption if the resolution is bigger than the surface roughness.

4.3.3. Facet growth during field days

The simulation of facet growth during field days is based on the simulation with BC 1 cm shade. The parameters can be seen in Table 6.

Table 6 Parameters simulation BC 1 cm

Variables		**Units**	**Values**
Thermal diffusivity	α	$[m^2/s]$	$3{,}45*10^{-7}$
Heat capacity	c	[J/K]	2090
Density	ρ_s	$[kg/m^3]$	277
Effective thermal conductivity	k_{eff}	[W/m*K]	0,2
Delta x	Δx	[m]	0,01
Delta t	Δt	[s]	60
Total Depth	x_{max}	[m]	0,9
Duration	t_{max}	hours	38

Net growth for 24 hours is shown in Figure 34. It shows 0 mm growth under 17 cm depth, except a miniscule positive growth between 18 cm and 22 cm. Above 17 cm negative growth increases with decreasing depth until it peaks at 0,042 mm at 1 cm depth.

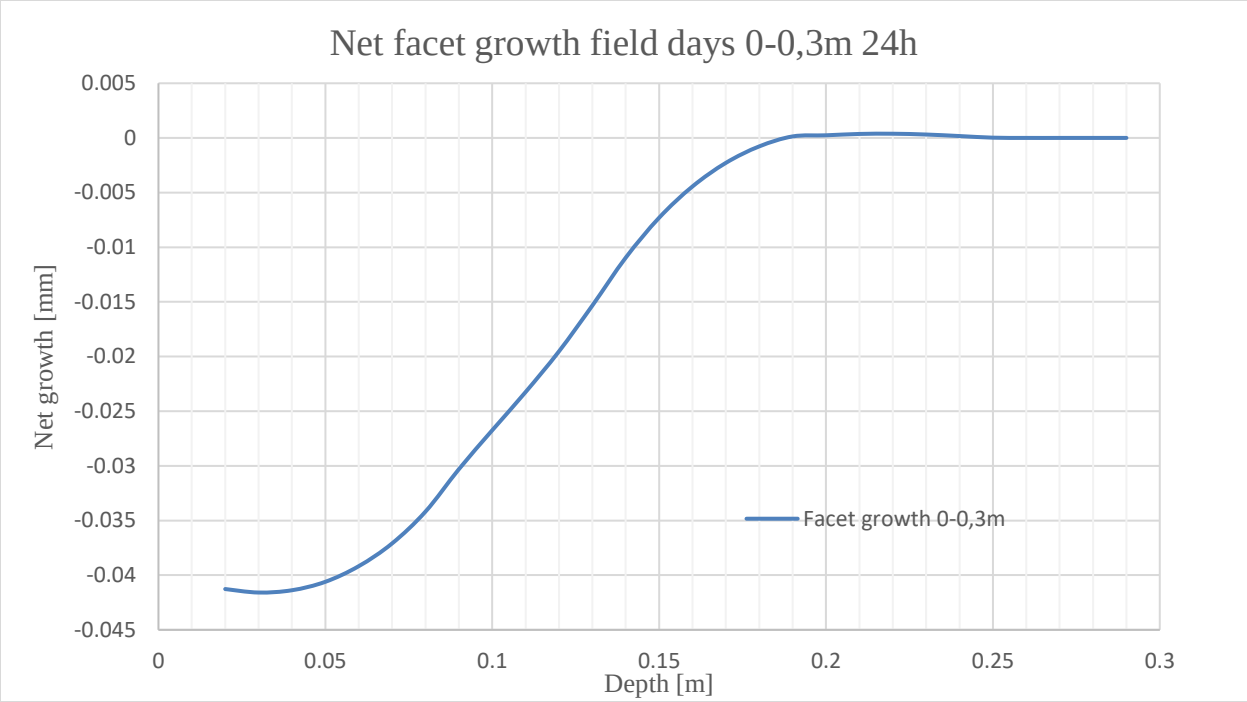

Figure 34 Net facet growth during the field days over 24 hours using simulation with BC 1 cm depth.

Figure 35 shows facet growth rate over time for three depths for the field days. The depths are chosen to be compared with the simulation based on sinusoidally oscillating surface temperatures (chapter 4.1.3).

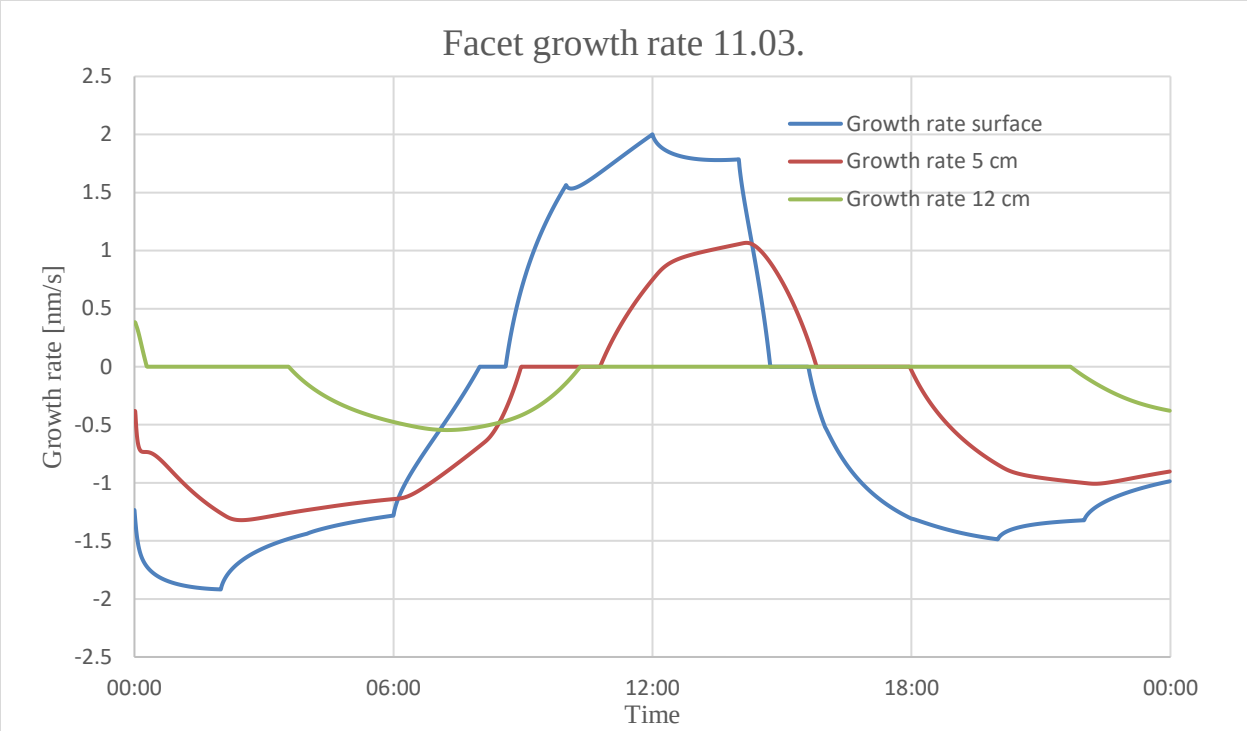

Figure 35 Facet growth rate first field day

The general shape of the curves in Figure 35 resembles those in Figure 21, where the surface temperatures were oscillated sinusoidally. In Figure 35 the spikes every two hours most easily seen in the curve for surface growth rate, are likely present because the top boundary condition is a linearly interpolated curve between measured temperatures every two hours. The steep decrease at the start of the simulation in all three curves is due to the initial conditions being linearly interpolated between thermometer measurements. The greatly increased resolution of the model compared with the measurements smoothens the temperature profile after little time has passed. Having a linearly interpolated boundary condition at two-hour resolution gives a relatively poor estimation of near-surface conditions. Higher resolution in the boundary condition is needed.

The area under 0 nm/s is bigger for all curves, which implies that all positive growth has been reversed. Although these results point to a net negative growth of facets, no facets were observed during the field days. As mentioned in chapter 2.4.1., high pressure, clear weather conditions with big diurnal temperature fluctuations are associated with formation of near-surface, diurnally recrystallized facets. The field days met these criteria. One factor that could have prevented faceting during the field days is that the incoming radiation may have been too high. Melting was observed on the roof of the cabin in Figure 7, and the

snow was moist. To form facets by diurnal recrystallization, radiation inputs just beneath that needed for melting are favorable (Stratton, 1977, as cited in Birkeland, 1998). The mean snow temperature during the field days might have been too high to form facets and caused melting instead.

4.4. Results 1st of April period

The weather during the 1st of April period consisted of three consecutive days with cold and clear nights with air temperatures down to -8°C followed by warm and sunny days with temperatures reaching 1.5°C (Figure 14). There was observed widespread near surface faceting in the region making this period very interesting with respect to investigate and modeling snow conditions producing near surface facets. The registered faceted crystals were found at 700 m.a.s.l. and above.

4.4.1. Radiometer data

Figure 36 shows the measured net radiation from the 1st of April period. The net shortwave radiation peaks around 14:00 all three days at 100 W/m^2. At the same time there is -100 W/m^2 net longwave radiation from the snow surface producing a net radiation around 0 W/m^2 at the given time. Net LW is most negative during the day and relatively stable during the night, excluding spikes around 04:30.

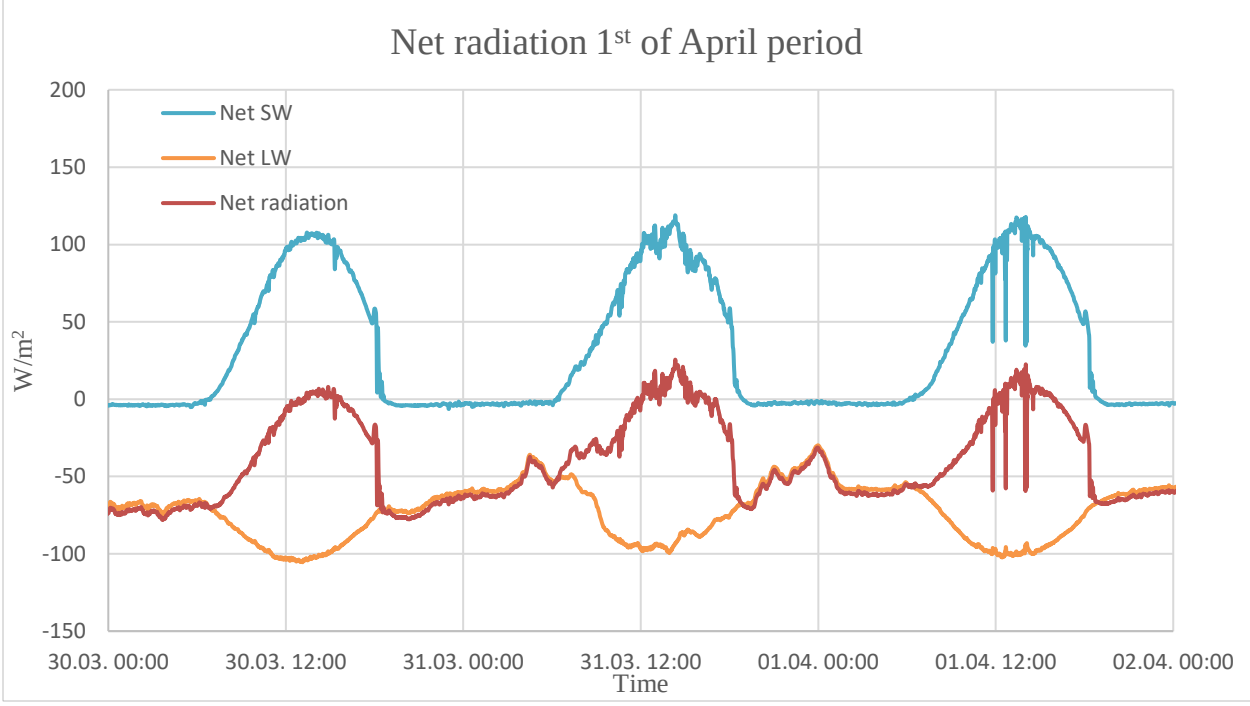

Figure 36 Net radiation from 30th of March to 1st of April.

The even arches on the net shortwave radiation curve indicate that the three days consisted of clear and sunny days with no significant cloud cover until 12:00 on the 1st of April. The cooling effect of outgoing longwave is dominant during the night, but the absolutes value of net longwave are largest during the day when snow surface temperatures are highest.

4.4.2. Tinytag settlement

Tinytag A and D changed their relative position to the snow surface during the logging period from 9th of March to 7th of April due to a combination of snowfall, melting and settling of the snowpack. The data from Tinytag A during the 1st of April period showed strong diurnal oscillations with temperatures varying approximately ± 7°C (Figure 37). The minimum temperatures were measured between 08:20 and 08:55 and varied between -8°C and -8.5°C. While the peak temperatures were recorded between 17:45 and 18:15 and varied between -0.6°C and -1.2°C.

As discussed in section 4.2.2 the temperature data from Tinytag A during the field day was not affected by the diurnal temperature fluctuations at the snow surface, indicating that A's relative distance to the snow surface have decreased from the field period to the 1st of April period. The estimation of Tinytag A's placement during the 1st of April period is 10 cm below the snow surface. Tinytag D only changed relative position to the surface, but not to the ground. During extraction Tinytag D was placed 50 cm above the ground, the same as during installation.

During the extraction of the Tinytags on the 7th of April, the total depth of the snowpack had decreased from 150 cm to 130 cm. Tinytag A was extracted approximately 20 cm below the snow surface in a layer of old and dense snow. Between the 1st of April period and the extraction day there was a snowfall of 10 cm in the region, meaning that the estimated total snow depth during the 1st of April period was 120 cm and Tinytag As placement was roughly 10 cm below the snow surface. This assumption neglects the settling of both the old and dense snow layer and the newly fallen snow. When comparing the manual temperature measurements taken in direct shade from the field days with the data from Tinytag A during the 1st of April period, Tinytag A should have measured between 5 and 10 cm below the snow surface. A wildlife camera is recommended in future studies to monitor snowfall, melting, and settling of the snowpack.

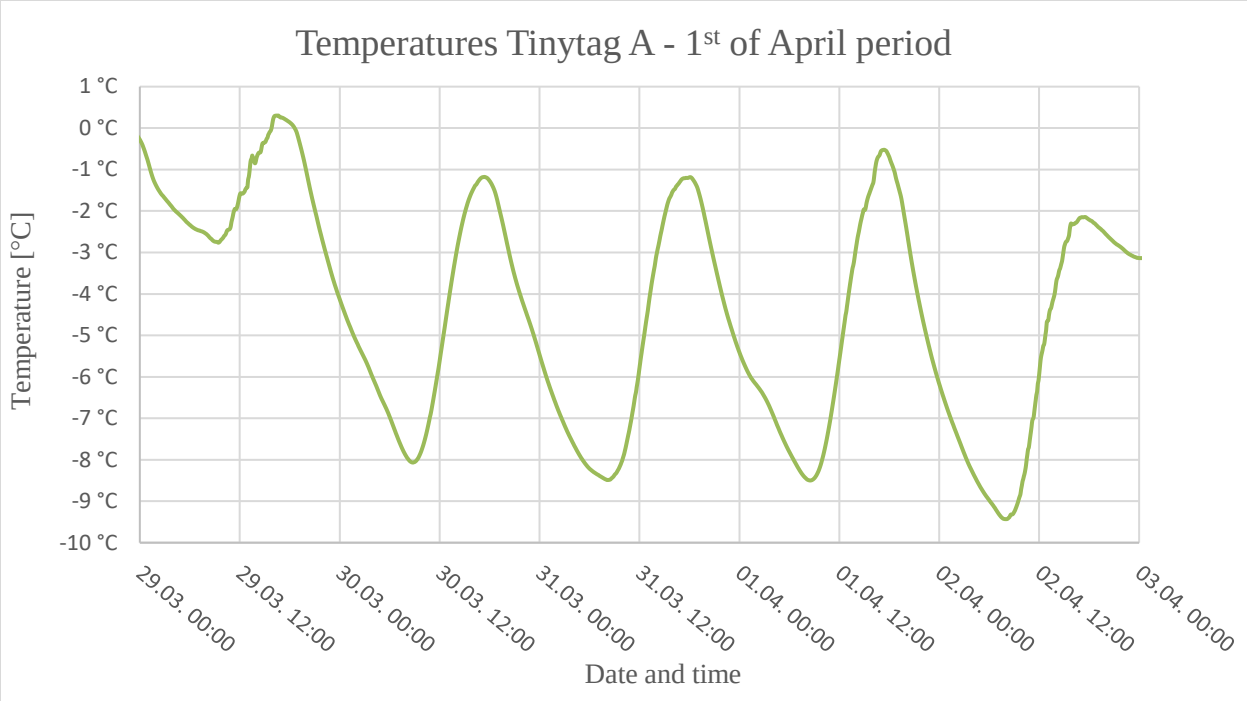

Figure 37 Temperatures from Tinytag A for the 1st of April period. The depth of logger A is estimated to be 10 cm at this time.

4.5. Simulating the 1st of April period

4.5.1. Discussion about IC and lower BC

Defining initial conditions for modeling the 1st of April period was a challenge since there were not any manual snow pit measurements to implement, as we had when simulating the field days. The IC used in the model is based on the best available data from the actual snowpack the 30th of March at 00:00. Three known points of temperature at depth were retrieved from the buried Tinytag temperature loggers. The surface temperature was calculated from the radiometer using equation (44) and the values between the known points were linearly interpolated.

In an initial attempt, the IC was used from our first manual temperature measurement 11th of March 00:00. A fixed upper BC was used based on surface temperatures calculated from the radiometer and lower BC set to 0°C at the bottom of the 120 cm deep snowpack. The simulation was run for ten cycles, a total of 30 days, of the 1st of April period (30.03. 00:00 to 01.04. 23:59) to get an equilibrated snow temperature profile. This set of temperatures was discarded after we compared them to the temperatures recorded by the three buried Tinytag temperature loggers. The simulated temperatures were much colder than the logged temperatures at their depths. At 10 cm the simulated temperature varied between -7°C and -12°C.

Tinytag A varied between -1°C and -8°C. Our simulated snowpack had gone through a 15-day cold period, while the real snowpack was relatively warm and only at the start of a cold period. This indicates that the net heat flux of the 1st of April period was not zero and that the entire snowpack cooled.

4.5.2. Simulation 1st of April using BC Heat flux with same parameters as field day

Parameters used in simulation of the 1st of April period are shown in Table 7. This is the model in its final stage, using all aspects implemented when simulating the field days. Figure 38 show the resulting temperature profiles over time.

Table 7 Parameters used when simulating the 1st of April period.

Variables		**Units**	**Values**
Thermal diffusivity	α	[m^2/s]	$3{,}45*10^{-7}$
Heat capacity	c	[J/K]	2090
Density	ρ_s	[kg/m^3]	277
Effective thermal conductivity	k_{eff}	[W/m*K]	0,2
Delta x	Δx	[m]	0,05
Delta t	Δt	[s]	30
Total Depth	x_{max}	[m]	1
Duration	t_{max}	hours	72

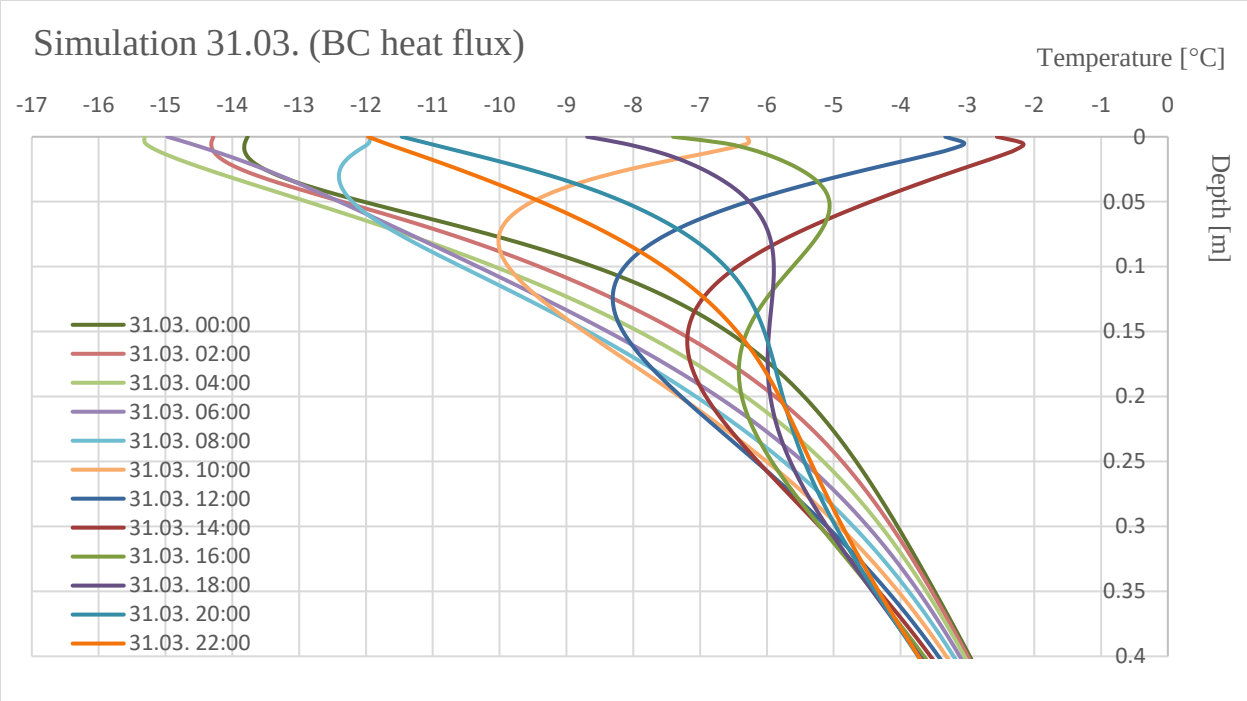

Figure 38 Simulation of 31st of March using BC heat flux.

Table 8 shows vapor pressure gradients 0 – 0,5 cm through the 1st of April period and Figure 39 show the same for 0 – 5 cm.

Table 8 Average and peak vapor pressure gradients from 0-0,5 cm through the 1st of April period

Date	**Average vpg 0-0,5 cm [mb/m]**	**Max vpg 0-0,5 cm [mb/m]**	**Min vpg 0-0,5 cm [mb/m]**
30.03.	-20,3	7,4	-59,4
31.03.	-15,9	7,0	-65,1
01.04.	-18,2	3,7	-64,9
Total	-18,1		

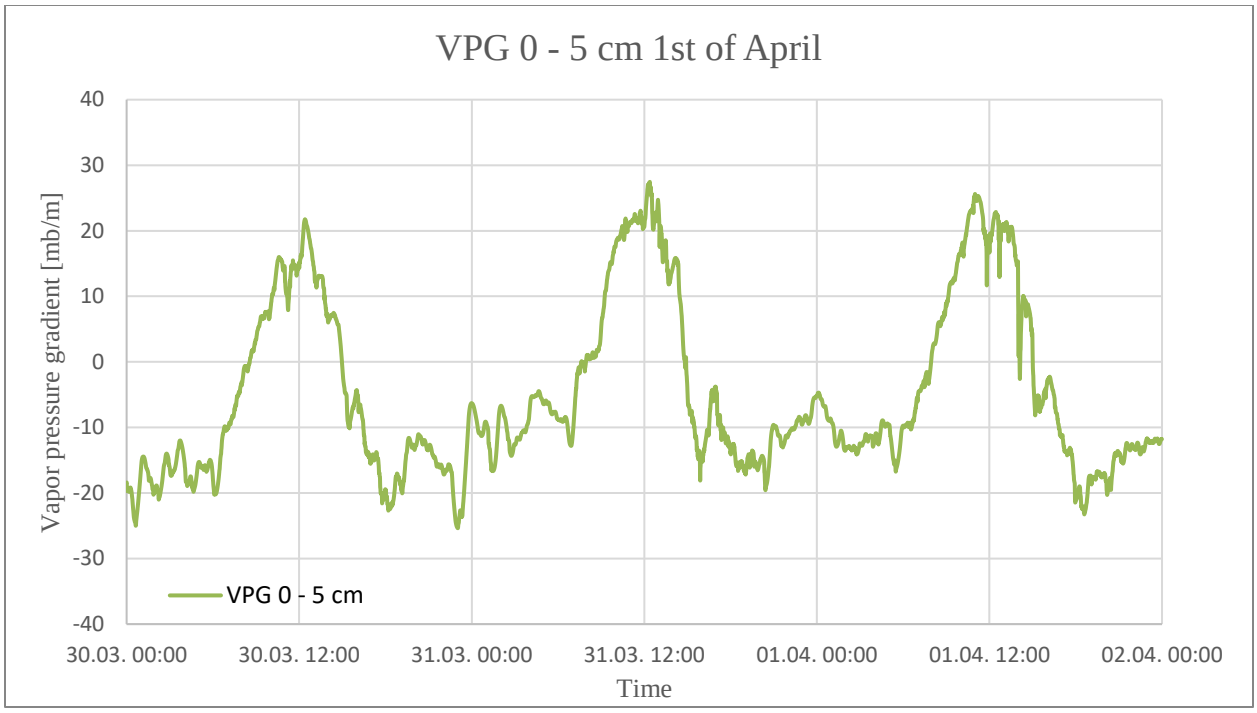

Figure 39 Vapor pressure gradient between 0 and 5 cm through the 1st of April period

Vapor pressure gradients during the 1st of April period range between around 25 mb/m to -25 mb/m. These values are very close to what Birkeland et al. (1998) measured in a similar weather period (Figure 5). Figure 39 also shows, albeit weakly, a trend during the night of having large negative vapor pressure gradients early, then lower as the night goes on and the snowpack cools. This indicates that the vapor pressure gradients calculated from the simulations are, if not perfect, at least reasonable. The resolution one chooses to use matters as well. The vapor pressure gradients for the top 5 mm of the simulated snowpack do not exceed positive values of 10 mb/m (Table 8). This suggests that the top 5 mm experience a nearly continuous negative vapor pressure gradient, only climbing above 0 mb/m when the snow surface is warming relative to the layer directly beneath, and the sun has not warmed the subsurface too much. The peak negative vapor pressure gradients are much larger when looking at the top 5 mm compared to the top 5 cm (Table 8 vs. Figure 39).

4.5.3. Facet growth during 1st of April period

The resulting net facet growth for the simulation of diurnal temperature fluctuations for the three days of the 1st of April period can be seen in**Error! Reference source not found.** Figure 40. All three days share similar characteristics, with net negative growth each day at all depths that experienced growth. Directly below the surface (first cm of depth) is where the peak negative growth has occurred. The 30.03. the peak growth was -0,12 mm at the surface. 31.03. and 01.04. have slightly lower peaks, at -0,09 mm and -0,10

mm, respectively. At about 2 cm depth the curves show a point of relatively little growth, -0,039 mm the 30.03., -0,006 mm the 31.03. and 0,013 the 01.04. Under this depth negative growth increases to a secondary maximum, before decreasing with depth to 0 mm at about 40 cm. The secondary negative peak is at 9 cm depth the 30.03., and around 12 cm depth the 31.03. and 01.04.

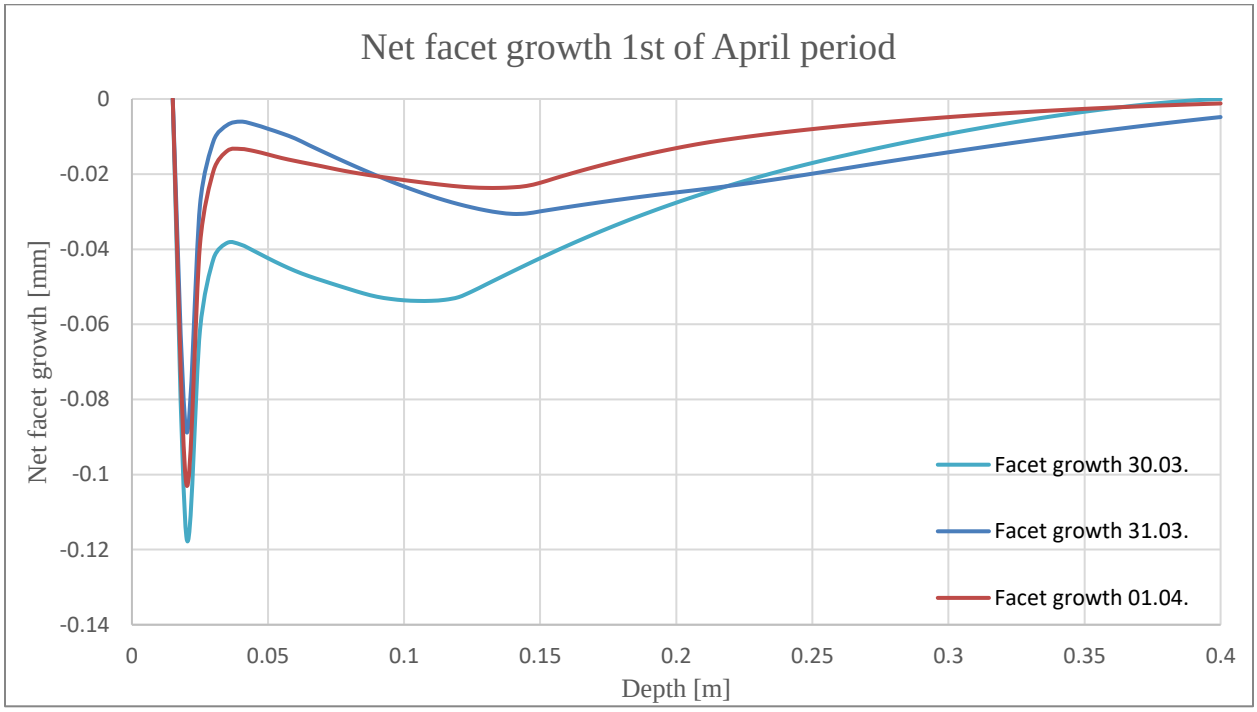

Figure 40 Net facet growth 1st of April period

The strong negative peak by the surface in Figure 40 fits quite well with what can be seen in Figure 38. The top centimeter of snow experiences negative temperature gradients both when cooling and heating. When the snowpack cools, LW radiation from the snow surface is the main mechanism, pulling the surface temperatures down and creating negative temperature gradients in the near-surface snow. When the snowpack is heating, SW radiation heats the subsurface snow, while the surface remains relatively colder due to LW cooling. This maintains the negative temperature and vapor pressure gradients in the top centimeter of the snowpack when the sun in up. The temperature of the snow is also warm during this period, so the negative temperature gradients give relatively high negative vapor pressure gradients. The strong negative temperature and vapor pressure gradients in the top centimeter during when the sun is acting on the snowpack match well with the mechanism radiation recrystallization. Separating the effects of diurnal and radiation recrystallization is, as stated in chapter 2.4.1., quite difficult, as these processes

can work in tandem. Had the radiation inputs been high enough to cause melting, the effect of melt-layer recrystallization could have played a role in the amount of faceting at this depth.

One of the clearest differences between the three simulated days is that the curve for 30.03. shows substantially more growth than either of the following days. This is thought to be because the entire snowpack was relatively warm going into the 1st of April period, resulting in higher average negative vapor pressure gradients (Table 8). The effects of faceting in a cooling snowpack, where the net energy balance is negative, may be an important factor that amplifies diurnal recrystallization and should be investigated in more detail in future studies. The initial snow type before faceting commences can be of import. This is a factor the model does not consider without manual observation of snow conditions.

Under 1,5 cm the curves in Figure 40 are similar to the curve in Figure 20, only shifted completely to the side of negative growth. The shape is discussed in detail in chapter 4.1.3. This indicates that asymmetry due to the average negative temperature gradient in the snowpack leads to preferential faceting in the negative direction.

4.5.4. Comparison of facet growth between simulations

The net growth of facets from all the simulations can be compared. The simulation of the Pinzer and Schneebeli (2009) shows a maximum net growth of 0,0036 mm and -0,0036 mm after 24 hours (Figure 17). The simulation with sinusoidally oscillating surface temperatures shows a maximum net growth of 0,022 mm after 24 hours (Figure 20). The simulation of the field days, using fixed surface temperatures based on manual temperature measurements, shows a maximum net growth of -0,042 mm after 24 hours (Figure 34). The simulation of the 1st of April period, using the model at its most complete stage, shows a maximum net growth of -0,12 mm after 24 hours (Figure 40).

The similarities between the simulation of the Pinzer and Schneebeli (2009) experiment and the simulation using sinusoidal temperature changes (chapter 4.1.3) make comparisons quite applicable. The maximum net growth of the simulation with sinusoidal surface temperatures is about six times as large. This may be due to scale or to the effect of a changing mean temperature with depth in the sinusoidal temperature simulation. The difference in maximum and minimum temperatures was much larger for the sinusoidal temperature simulation. This means that a set temperature gradient could give higher vapor pressure gradients when the snow was warm than in the Pinzer and Schneebeli (2009) simulation.

No faceting was observed during the field work, while widespread faceting was registered above 700 meters in the region after the 1st of April period. The 1st of April value (-0,12 mm) is about three times as big as the field day value (-0,042 mm), but the total size after three days of compounded faceting through the 1st of April period could have given facet growth around -0,36 mm. Since the values were obtained with quite different simulations, the 1st of April simulation being more reliable, they are not necessarily suited for comparison. If the values are assumed to be correct for their respective time periods, it seems reasonable that facet growth less than 0,1 mm would not be observed by the naked eye. 0,36 mm of growth, however, may be visible, especially with a loupe for snow observation. The simulations are run based on data from 720 m.a.s.l. This is quite near the lower limit of where facets were registered after the 1st of April period. It may be that the locality at Slakkafjellet was too close to the fjord for noticeable facets to form. The function for facet growth rate has a large impact on the resulting facet growths. If the difference in growth between field days and 1st of April was bigger, or direct observation of facets at the field area had been made, one could with more certainty say something about the validity of the function. More work is recommended to make a more realistic and accurate function for facet growth rate.

5. Conclusion

The model developed in this investigation is an approximation of the real world, so assumptions and simplifications will always leave room for improvement. The biggest issue with the final stage of the model as it stands today is that outgoing longwave radiation is used as a control, with windspeed in the implementation of sensible heat being used as a fitting parameter. The model can be forced to fit any measured values of outgoing longwave radiation, by adjusting wind speed, without regard to how accurate those values are. Changes in latent heat flux are not considered and are therefore combined with sensible heat flux and adjusted with wind speed. Having measurements of these turbulent fluxes at different heights above the snowpack would enable quantifying sensible and latent heat fluxes to a stronger degree.

A second issue is that using a constant solar radiation extinction coefficient is too simplistic. An extinction coefficient that considers the properties of different wavelengths of shortwave radiation is needed to model the near-surface conditions more accurately. Varying density and effective conductivity with depth is a natural step in further development of the model.

Despite these weaknesses, the model gives reasonable temperatures with depth over time, when compared with measured temperatures in the field. It allows for calculations of vapor pressure gradients at much higher resolution than manual field measurements. The calculated vapor pressure gradients seem plausible when compared to values presented by Birkeland et al. (1998).

Facet size is difficult to compare between studies, and further research into the function for facet growth rate by vapor pressure gradient is needed, especially for the vapor pressure gradients below 5 mb/m. The calculations of facet growth can, however, be compared between runs of the model.

Simulation of the Pinzer and Schneebeli (2009) experiment showed that even though their snow sample was exposed to large vapor pressure gradients, most of the growth was reversed when the direction of the vapor pressure gradient reversed. After one 24-hour cycle there was a maximum of 0,0036 mm of positive and negative net facet growth at, respectively, the top and bottom of the simulated snow sample. This can be attributed to the effect of temperature (hypothesis 1). Pinzer and Schneebeli (2009) took µCT scans in the middle of the snow sample, where the simulated results indicate faceting was nearly zero.

By comparing the simulated results of our purely theoretical approach and the results from simulations based on data from the field, the two hypothesized mechanisms of real-world asymmetry causing diurnal recrystallization were investigated:

Hypothesis 1: Effect of temperature. Simulation of the Pinzer and Schneebeli (2009) experiment isolated the effect of temperature, suggesting that this effect played a role in their experiment as well as in nature. The effect of temperature appears to, as expected, amplify vapor pressure gradients when the snowpack is warm. A temperature gradient in a warm snowpack does give a higher vapor pressure gradient than the same temperature gradient in a cold snowpack.

Hypothesis 2: Heating and cooling of the snowpack happens differently. In the simulation of the 1st of April period, below about 2 cm, the temperature profile showed the same characteristics as the simulation run with sinusoidally oscillating surface temperatures. This suggests that below 2 cm, the average negative temperature gradient of the snowpack makes it easier for the threshold vapor pressure gradient required for faceting to be exceeded in the negative direction. Positive growth rates induced by positive vapor pressure gradients are fully reversed and a net negative growth occurs. In the top 0-2 cm of the snowpack, negative gradients of temperature and vapor pressure were maintained through the cooling and most of the warming of the simulated snowpack. This can be attributed to a combination of diurnal recrystallization and radiation recrystallization, and it is difficult to separate one process from the other.

The results of this thesis suggest that Pinzer and Schneebeli (2009) perhaps could have observed faceting in their experiment due to the effect of temperature (hypothesis 1), but a better treatment of rounding is required for further investigation. The results also indicate that diurnal recrystallization can occur in nature because facet growth rate dominates in the negative direction, undoing any faceting that has happened in the positive direction (hypothesis 2). This effect is amplified when warm snow experiences strong negative temperature gradients but dampened when warm snow experiences strong positive temperature gradients (hypothesis 1). In the top centimeter of the snowpack, both mechanisms work together to produce the highest negative facet growth. A potentially important factor that was not investigated is snowpack mean temperature drift.

6. References

Anderson, E. A. (1976). *A Point energy and mass balance model of a snow cover*. NOAA.

Armstrong, R. L., & Brun, E. (2008). *Snow and climate: Physical processes, surface energy exchange and modeling*. University Press.

Benn, D. I., & Evans, D. J. A. (2010). *Glaciers & glaciation* (2nd ed). Hodder education.

Birkeland, K. W. (1998). Terminology and Predominant Processes Associated with the Formation of Weak Layers of Near-Surface Faceted Crystals in the Mountain Snowpack. *Arctic and Alpine Research*, *30*(2), 193. https://doi.org/10.2307/1552134

Birkeland, K. W., Johnson, R. F., & Schmidt, D. S. (1998). Near-Surface Faceted Crystals Formed by Diurnal Recrystallization: A Case Study of Weak Layer Formation in the Mountain Snowpack and Its Contribution to Snow Avalanches. *Arctic and Alpine Research*, *30*(2), 200. https://doi.org/10.2307/1552135

Brandt, R. E., & Warren, S. G. (1993). Solar-heating rates and temperature profiles in Antarctic snow and ice. *Journal of Glaciology*, *39*(131), 99–110. https://doi.org/10.1017/S0022143000015756

Cooperstein, M. S., Birkeland, K. W., & Hansen, K. J. (2004). *THE EFFECTS OF SLOPE ASPECT ON THE FORMATION OF SURFACE HOAR AND DIURNALLY RECRYSTALIZED NEAR-SURFACE FACETED CRYSTALS: IMPLICATIONS FOR AVALANCHE FORECASTING*.

Dunlop, S. (2008). A Dictionary of Weather. In *A Dictionary of Weather*. Oxford University Press. Retrieved from: https://www.oxfordreference.com/view/10.1093/acref/9780199541447.001.0001/acref-9780199541447

Fierz, C., Bakermans, L., Jamieson, B., & Lehning, M. (2008). *MODELING SHORT WAVE RADIATION PENETRATION INTO THE SNOWPACK: WHAT CAN WE LEARN FROM NEAR-SURFACE SNOW TEMPERATURES?*

Fredston, J. A., & Fesler, D. (2011). *Snow sense: A guide to evaluating snow avalanche hazard* (5th ed.). Alaska Mountain Safety Center.

Fukuzawa, T., & Akitaya, E. (1993). Depth-hoar crystal growth in the surface layer under high temperature gradient. *Annals of Glaciology*, *18*, 39–45. https://doi.org/10.1017/S026030550001123X

Gray, D. M., & Male, D. H. (1982). Snowcover ablation and runoff. In D. M. Gray & D. H. Male (Eds.), *Handbook of Snow: Principles, Processes, Management & Use*. ARCTIC.

Hachikubo, A. (2001). Numerical modelling of sublimation on snow and comparison with field measurements. *Annals of Glaciology*, *32*, 27–32. https://doi.org/10.3189/172756401781819265

Hardy, D., Williams, M. W., & Escobar, C. (2001). Near-surface faceted crystals, avalanches and climate in high-elevation, tropical mountains of Bolivia. *Cold Regions Science and Technology*, *33*(2–3), 291–302. https://doi.org/10.1016/S0165-232X(01)00055-6

Jamieson, B. (2006). Formation of refrozen snowpack layers and their role in slab avalanche release. *Reviews of Geophysics - REV GEOPHYS*, *44*. https://doi.org/10.1029/2005RG000176

Kipp & Zonen. (n.d.-a). *CNR 4 Net Radiometer: Instruction Manual* (v. 2104). Retrieved from: https://www.kippzonen.com/Download/354/Manual-CNR-4-Net-Radiometer-English-V2104

Kipp & Zonen. (n.d.-b). *CNR 4 Net Radiometer: Instruction sheet* (v1706 ed.). Retrieved from: https://www.kippzonen.com/Download/892/Instruction-Sheet-Net-Radiometers-CNR4-8-wire-version

Kipp & Zonen. (2020). *Instruction Manual: Logbox SE* (2020th–06 ed.).

LaChapelle, E. R., & Armstrong, R. L. (1977). *Temperature Patterns in an Alpine Snow Cover and Their Influence on Snow Metamorphism.* COLORADO UNIV BOULDER INST OF ARCTIC AND ALPINE RESEARCH. Retrieved from: https://apps.dtic.mil/sti/citations/ADA040169

Langham, E. J. (1982). Physics and properties of snowcover. In D. M. Gray & D. H. Male (Eds.), *Handbook of Snow: Principles, Processes, Management & Use*. ARCTIC.

Lundberg, J. C., Storebakken, B., & Zieritz, N. (2019). *Modelling the effect of surface hoar formation on the temperatture gradient and vapor pressure gradient in a snowpack*. HVL.

Marbouty, D. (1980). An Experimental Study of Temperature-Gradient Metamorphism. *Journal of Glaciology*, *26*(94), 303–312. https://doi.org/10.3189/S0022143000010844

McCabe, D., Munter, H., Catherine, D., Henninger, I., Cooperstein, M., Leonard, T., Adams, E. E., Slaughter, A. E., & Staron, P. J. (2008). *NEAR-SURFACE FACETING ON SOUTH ASPECTS IN SOUTHWEST MONTANA*. 8.

McClung, D., & Schaerer, P. (2006). *The avalanche handbook* (3rd ed.). Mountaineers Books.

Miller, D. A., & Adams, E. E. (2009). A microstructural dry-snow metamorphism model for kinetic crystal growth. *Journal of Glaciology*, *55*(194), 1003–1011. https://doi.org/10.3189/002214309790794832

Miller, D. A., Adams, E. E., & Brown, R. L. (2003). A microstructural approach to predict dry snow metamorphism in generalized thermal conditions. *Cold Regions Science and Technology*, *37*(3), 213–226. https://doi.org/10.1016/j.coldregions.2003.07.001

Nes, C. L. (2018). *Skikompis: Snøskred og trygg ferdsel* (2. utg.). Fri flyt. https://www.nb.no/search?q=oaiid:"oai:nb.bibsys.no:999919961088902202"&mediatype=bøker

Pinzer, B. R., & Schneebeli, M. (2009). Snow metamorphism under alternating temperature gradients: Morphology and recrystallization in surface snow. *Geophysical Research Letters*, *36*(23). https://doi.org/10.1029/2009GL039618

Pinzer, B. R., Schneebeli, M., & Kaempfer, T. U. (2012). Vapor flux and recrystallization during dry snow metamorphism under a steady temperature gradient as observed by time-lapse micro-tomography. *The Cryosphere*, *6*(5), 1141–1155. https://doi.org/10.5194/tc-6-1141-2012

Stössel, F., Guala, M., Fierz, C., Manes, C., & Lehning, M. (2010). Micrometeorological and morphological observations of surface hoar dynamics on a mountain snow cover: SURFACE HOAR ON MOUNTAIN SNOW COVERS. *Water Resources Research*, *46*(4). https://doi.org/10.1029/2009WR008198

Sturm, M., Holmgren, J., König, M., & Morris, K. (1997). The thermal conductivity of seasonal snow. *Journal of Glaciology*, *43*(143), 26–41. https://doi.org/10.3189/S0022143000002781

Sturm, M., & Johnson, J. B. (1992). Thermal conductivity measurements of depth hoar. *Journal of Geophysical Research: Solid Earth, 97*(B2), 2129–2139. https://doi.org/10.1029/91JB02685

Varsom. (2022). *Snøskredulykker- og hendelser* [Statistics]. Retrieved 30.05.22 from: https://www.varsom.no/snoskred/snoskredulykker/

Warren, S. G., & Wiscombe, W. J. (1980). A Model for the Spectral Albedo of Snow. I: Pure Snow. *Journal of Atmospheric Sciences, 37*.

7. Appendices

7.1. Wiring of CNR 4 Net Radiometer to Logbox SE

Figure 41 shows how we wired the radiometer to the Logbox. The cable marked as “sensor connection” in Figure 41 is the wiring from the pyranometers and pyrgeometers. We connected the nine wires from this cable to the inputs A9 to A12 (plus the thickest black wire to ground) based on figure 1.2 in the CNR 4 instruction manual v2104 (Kipp & Zonen, n.d.-a).

The CNR 4 Net Radiometer has two options for measuring the instrument body temperature: using a thermistor or a Pt-100. Both options are equally accurate. The Logbox SE we used does not support the use of the CNR 4 Net Radiometer and a Pt-100 simultaneously. Therefore, we folded the grey, green, yellow, and brown wires for the Pt-100 back and taped them to the yellow cable labelled “temperature connection” in Figure 41. To wire the thermistor we connected the black wire to VREF, the white to AIN4, the thick black wire to GND, and a 10 kΩ resistor between AIN4 and GND based on figure 8.6 in the Logbox SE instruction manual v2020-06 (Kipp & Zonen, 2020). The black and white wires can be switched.

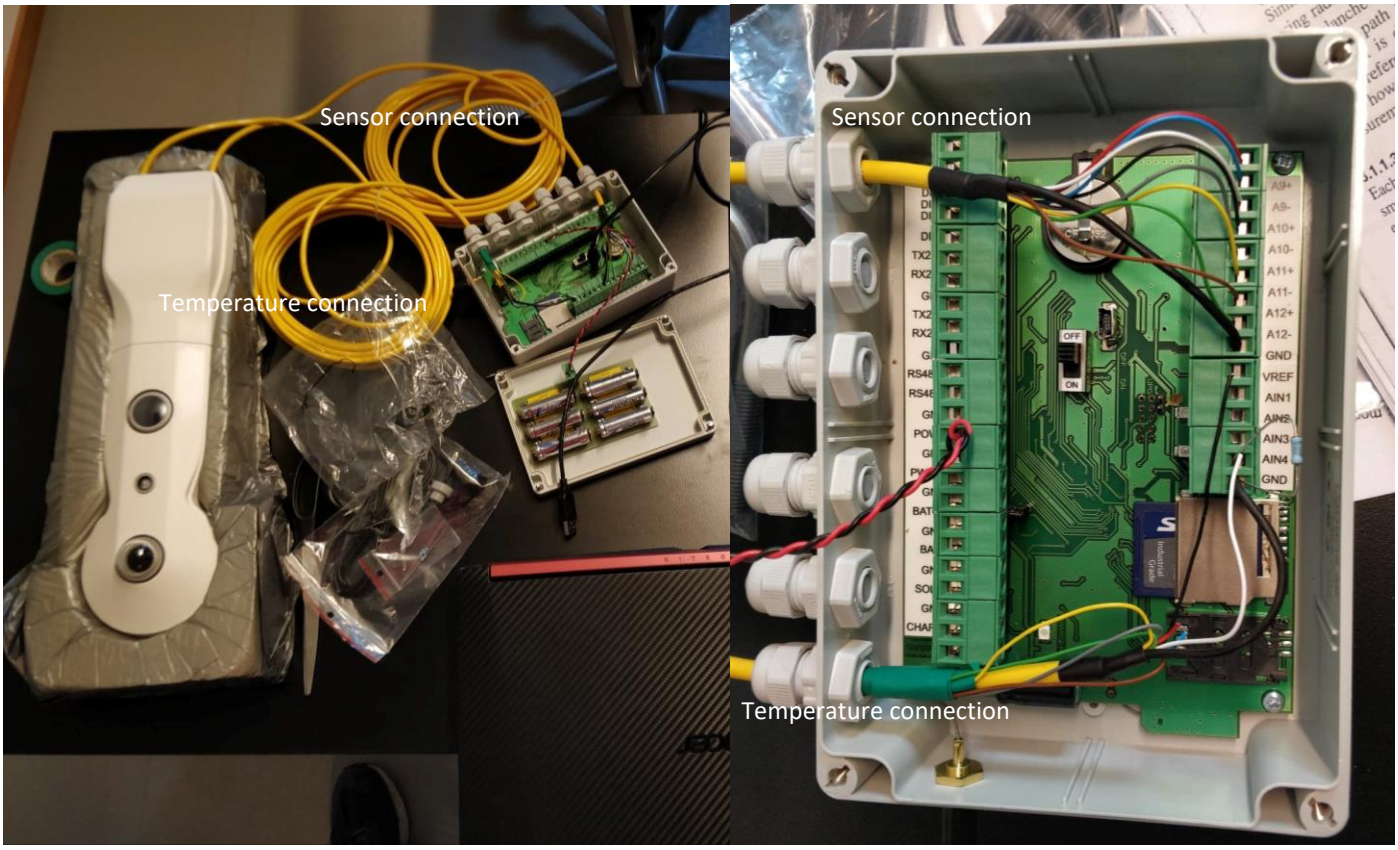

Figure 41 Photo of the inside of the Logbox SE after wiring with the CNR 4 Net Radiometer

7.2. IR thermometer

Figure 42 Photo of IR thermometer.

7.3. Pyranometer and pyrgeometer sensitivities

Table 9 Pyranometer and pyrgeometer sensitivities

Upper pyranometer sensitivity (μV/W/m^2)	15.36
Lower pyranometer sensitivity (μV/W/m^2)	14.00
Upper pyrgeometer sensitivity (μV/W/m^2)	11.03
Lower pyrgeometer sensitivity (μV/W/m^2)	11.67